Studies on perovskite oxyhydrides: catalysis and hydride anion diffusion

Ya Tang

2018

Contents

General Introduction

Background of This work

Heterogeneous metal catalysts are vital to the chemical industry, especially in the conversion from fossil resources into fuels and a broad range of chemicals such as ammonia, methane, and methanol.[1, 2] Typically, heterogeneous metal catalysts are consisting of several phases including metal particles and support materials. Normally, the metal particles are catalytically active phase in heterogeneous catalysts;[3] for example, Fe or Ru in ammonia synthesis or Ni in catalytic hydrogenation reactions. In addition, however, support materials are extremely important and play a definitive role in determination of catalytic performance. Figure 1 illustrates a schematic model of the heterogeneous catalysis research.[4] The importance of support effect is much in evidence in the heterogeneous catalysts; that is, the support materials help to stabilize the high dispersion of the metal particles,[5, 6] or involves the catalytic reactions (i.e. Mars–van Krevelen mechanism[4, 7-9]). Thus, the support material is a big concern for the searching of effective heterogeneous metal catalysts.

In metal-based heterogeneous catalysts, most commonly used support materials are oxides such as MgO,[10] Al_2O_3,[11] TiO_2,[12] as well as perovskites $CaTiO_3$[13] and $BaTiO_3$[14]. In most cases, their function is determined by the metal cation, in terms of acidity, basicity, or other factors. In the recent past few years, a rising number of studies centered on searching for new types of catalytic supports with distinct electronic properties or surface/bulk anionic defects, such as inorganic electrides[15, 16] and metal hydrides.[17-19] A prime example is with ammonia synthesis/decomposition, where inorganic electrides like $12CaO{\cdot}7Al_2O_3{:}e^-$ (C12A7:e$^-$),[15, 20] $[Ca_2N]{:}e^-$,[21, 22] CaH_2,[19] Ca_2NH,[23] Y_5Si_3,[24] $LaCu_{0.67}Si_{1.33}$,[25] and LaScSi[26] exhibit excellent electron donation ability to the adsorbed gas molecular on metals, and results in significant weakening of the N_2 triple bond[15, 20] or Ru–N bond.[27] Recently, with a range of transition metals (V, Cr, Mn, Fe, Co, and Ni), LiH[17] and BaH_2[18] were examined as catalytic supports for ammonia synthesis. In transition metals/LiH (or BaH_2), hydride (H^-) helps to remove the activated nitrogen atoms from metal surface, leading to break the scaling relationship between metal-nitrogen strengths and activity.[9, 17]

We have recently reported a new perovskite-type oxyhydride $BaTiO_{3-x}H_x$ (x = 0.1–0.6), where the oxygen anions (O^{2-}) are partly replaced by hydride ions (H^-).[28] At elevated temperatures, hydride in $BaTiO_{3-x}H_x$ can be exchanged with the surrounding

atmosphere (such as D_2, at approx. 400 ˚C).[28, 29] Furthermore, with $BaTiO_{3-x}H_x$, treatment with N_2/NH_3 gas at the same temperature results in conversion to the oxynitride.[30, 31] These hydride exchange involves N_2 (or NH_3, H_2) bond cleavage, and hints that the oxyhydride maybe is a useful material for activation of N_2 (or NH_3, H_2). Hence, the perovskite oxyhydrides show a high potential in the applications of numerous catalytic reactions. On the other hand, unlike some hydride-containing compounds such as alkali hydrides, $Ba_{21}Ge_2O_5H_{24}$,[32] or $12CaO{\cdot}7Al_2O_3{:}H^-$,[33] these transition metal oxyhydrides benefit from being members of the large perovskite family. This makes systematic comparisons for probing mechanisms possible, and provides a broad materials platform with a wide potential to further optimize catalytic activity by choice of the *A*-site or *B*-site.

Perovskite oxyhdyrides: new opportunities for catalytic supports

Hydrogen in oxides is a rather young scientific field since some perovskite oxides have been known to contain several atomic percent of hydrogen and then exhibit proton conductivity at elevated temperatures.[34-36] In oxide lattice, hydrogen may take in a variety of positions and charge states. When an oxide is equilibrated in gas mixtures with hydrogen-containing gases, e.g., water vapour, hydrogen will dissolve in the oxides.[37] Hydrogen may in principle dissolve in the forms of different species: as neutral atoms (H^0, is not a stable charge state in oxides and easily ionized to proton[38, 39]), hydride ions (H^-, the hydride species can be form in oxides under reducing condition[37]), and protons (H^+). Hydride ion (H^-), unlike a proton, is highly polarizable because two electrons are bound by just one proton.[40, 41] The H^- has some similarity with oxygen ion (O^{2-}, and also F^-) in both radius and charge, while the radius and charge of the proton and oxygen ion are both widely different.[37, 41] Moreover, the H^- is lighter in mass, smaller in charge (cf. the oxide anion) and has a high standard potential of –2.2 V for H^-/H_2, which makes this ligand mobile and labile.[42] However, in oxides the commonly observed dissolved hydrogen species are the protons, often termed interstitial protons,[43, 44] but in reality always associated with oxygen ions as hydroxide groups, OH.[37, 45-47] In contrast to proton, the existence of H^- in oxides, actually, a very rare case.[37] Stable compounds containing both hydride and oxygen anions were confirmed in few examples such as Ba_3AlO_4H,[48] $Ba_{21}Ge_2O_5H_{24}$,[49] $LaSrCoO_3O_{0.7}$,[40] and $BaTiO_{3-x}H_x$[28, 50].

Titanium oxyhydride $BaTiO_{3-x}H_x$ were synthesized by reduction with CaH_2.[28] A symmetry change from the tetragonal *P4mm* space group to the cubic $Pm\bar{3}m$ space group is observed during conversion of the oxide to oxyhydride, which is due to the electron doping.[28, 29] These perovskite-type oxyhydrides can also be easily modified in terms of *A*-site or *B*-site choice.[29] Furthermore, using H/D exchange experiments, the oxyhydride was found to be almost fully deuterated (based on neutron diffraction data), indicating that the lattice H^- in $BaTiO_{3-x}H_x$ can be exchanged with surrounding D_2 gas at 400 ˚C.[28]

This exchange involves D_2 (H_2) bond dissociation and hints that various hydrogenation reactions may be possible. On the other hand, since the chemical reactivity of the lattice hydride is quite active at elvated temperatures (i.e. thermolability), $BaTiO_{3-x}H_x$ is exploited for various synthetic uses.[30, 31, 51] For example, $BaTiO_{3-x}H_x$ has been shown to be a useful precursor for topotactic conversion to oxynitrides via H/N exchange under moderate conditions with N_2 or NH_3 atomsphere, as shown in Figure 2.[31] Other mixed anion phases impossible to access otherwise, such as $BaTi(O, H, F)_3$ and $BaTi(O, H, OH)_3$, have also been reported using the anion exchange reactions starting from titanium oxyhydrides (Figure 2).[30] Hence, these hydride exchange results suggesting that the oxyhydride is a useful material for activation of H_2, NH_3, and even the robust N_2. It is well known that N_2 cleavage is the key aspect in the ammonia synthesis. Hence, the perovskite oxyhydride offers a new opportunity for N_2 activation and maybe NH_3 synthesis. Other than N_2 activation, the perovskite oxyhydride provides a spillover pathway for adsorbed hydrogen since the hydride exchange with atmosphere hydrogen (H/D exchange) at elevated temperatures. This suggests that the oxyhydride maybe useful for Ru metals, where the hydrogen is easily poisioned.

In addition to thermal lability described above, another suspected interesting feature of oxyhydride is the electron back donation from lattice H^-, leading the Lewis basicity (i.e. the solid basicity) of oxyhydride maybe higher than the corresponding oxides. The importance of solid basicity for catalytic performance of supported metal catalysts has been described elsewhere, such as NH_3 synthesis[15] and CO_2 methanation reaction[52, 53]. However, the basicity of $BaTiO_{3-x}H_x$ has not yet been established due to the typical methods such as CO_2–TPD (temperature-programmed desorption) requires high thermal stability materials but the oxyhydride sample decomposes when the temperatures higher than 400 ˚C. Hence, the direct determination of solid basicty for oxyhydrides is impossible. However, some other methods such as kinetic analysis may be provide kinetic insights into the hydride role during the catalytic reactions. All in all, the perovskite oxyhydrides have a large potential in the applications of heterogeneous catalysis.

Hydride diffusion in oxyhydrides: experimental analysis

In addition to the interest of catalysis, the mobility of H^- in an oxyhydride framework is another concern of the perovskite oxyhydrides. The existence of hydride ion in oxides have been identified or suggested only in a limited class of oxides.[40, 48, 49, 54] The reason is because of the formation of hydride ions generally requires strong reducing conditions, which often result in degradation of the host material itself.[50, 54] The motivation for studying hydride diffusion in oxides is similar with the proton diffusion.[36] However, the experimental analysis of hydride diffusion in oxyhydrides is rarely reported. Orthorhombic $LaSrCoO_3H_{0.70}$, the first transition metal oxyhydride with significant

amounts of hydride ions, can obtain by CaH_2 reaction with the layered perovskite $LaSrCoO_4$.[40, 55] Quasielastic neutron scattering (QENS) were used to investigate the hydride diffusion in $LaSrCoO_3H_{0.70}$ and revealed that the hydride ions migrated along the direction of vacancies in the one-dimensional (1D) hydride anion sublattice above 675 K.[36] The Chudley-Elliot model and Gaussian model were used to fit the Lorentzian FWHM versus Q lines, which results indicated the two models have a very little difference in the quality of fits. It was found that the H^- hopping distance is equal to the length of a lattice parameter (ca. 3.85 Å), suggesting that the hydride is jump between vacant sites along the *a*-axis within the perovskite layer (as shown in Figure 3). Very recently, Kanno and co-workers[56] demonstrated pure H^- conduction in $La_{2-x-y}Sr_{x+y}LiH_{1-x+y}O_{3-y}$ using impedance measurements, revealing that two-dimensional (2D) H^- conduction in the layered lithium perovskite is facilitated by introducing H^- vacancies (y), though the activation energy of 68.4 kJ mol^{-1} for $La_{0.6}Sr_{1.4}LiH_{1.6}O_2$ (x = 0.40 and y = 1.0) is somewhat larger than that in $LaSrCoO_3H_{0.70}$ (nearly 20 kJ mol^{-1}).

Turing to $ATiO_{3-x}H_x$ (A = Ba, Sr, Ca or Ca-Sr, Sr-Ba solid solutions, or Eu), using TG-MS, the titanate oxyhydride perovskites have been shown to release H_2 at approx. 400 ˚C when heated under an inert atmosphere (such as Ar).[28, 29, 51, 57] The same with H_2 release, heating oxyhydrides under D_2 at the same temperature resulted in H/D anion exchange, yielding the oxydeuteride, as shown in Figure 4[28, 57]. Such an H/D exchange implies the diffusion of hydride in the oxyhydride lattice. However, the high electronic conductivity (mixed electron and anion conductivity) of $ATiO_{3-x}H_x$ does not permit the direct measurement of H^- conductivity by an impedance measurement. Alternatively, DFT calculations were used to investigate the hydride diffusion in oxyhydride lattice.[58-62] On the basis of calculation results, Iwazaki *et al.* proposed that, in $BaTiO_3$ lattice, the hydride first transfer two electrons to the titanium atoms, and then jump as a proton to an interstitial site, after which it converts back to a hydride ion on another anionic site.[58] Moreover, using DFT calculations, Zhang *et al.*[59] found that the hydrogen diffusion in $BaTiO_{3-\delta}H_x$ is dominated by migration of the interstitial H with low energy barrier. Recent calculations by Liu *et al*. have examined the activation energy of hydride diffusion in the $BaTiO_3$ lattice.[61] They showed that the hydride jumping between the nearest neighbor sites is an energy-minimizing process.

Since the quite mobile hydride anions (or thermolability), oxyhydrides exhibit a broad potential applications in solid state synthesis, solid state ionics, and catalysis. With the recent increase in reported oxyhydrides from solid state chemistry, a universal experimental method to investigate the hydride diffusion mechanism would help explain many curiosities and serve as a convenient tool to investigate the suitability of oxyhydrides for various applications. In summary, the potential applications of perovskite oxyhydrides are essentially related to the thermal

behaviour of hydride anions. Hence, the dynamics research of hydride will enhance the potential use of perovskite oxyhydrides in applications for solid state synthesis, catalysis, or ionics.

Outline of This Work

On the basis of gas molecule activation on these water-stable oxyhydrides, together with the suspected strong electron donating powder of hydride, we try to perform oxyhydride as a new type of catalytic supports for Fe, Co, Ni, and Ru-based catalysts for ammonia synthesis and CO_2 methanation reaction. Accordingly, this thesis focuses on investigations of the catalytic applications of $A\mathrm{TiO}_{3-x}\mathrm{H}_x$, with the aim of developing a new kind of support materials for metal based heterogeneous catalysts. Furthermore, the thermal behaviors of hydride ions in oxyhydride lattice (i.e. diffusion mechanism) were investigated by the H/D exchange.

In *Chapter 1*, the solid-state hydride-containing Ti compounds (TiH_2 and $BaTiO_{2.5}H_{0.5}$) exhibit continuously (~7 days) form NH_3 under H_2/N_2 flow conditions, with activity (up to 2.8 mmol g^{-1} h^{-1}) almost comparable to conventional supported Ru catalysts such as Cs-Ru/MgO or $Ru/BaTiO_3$ that we have tested. As with the homogeneous analogues, the initial presence of hydride within the catalyst is critical. Moreover, a rare hydrogen-based Mars–van Krevelen (MvK) mechanism may be at play here. Conventional scaling rules of pure metals predicts essentially no activity for Ti, making this a previously overlooked element, but the results show that by introducing hydride, the repertoire of heterogeneous catalysts can be expanded to include formerly unexamined compositions without resorting to precious metals.

In *Chapter 2*, the ammonia synthesis activities of Ru, Fe, $\mathrm{Co}/A\mathrm{TiO}_{3-x}\mathrm{H}_x$ (A = Ca, Sr, Ba) were examined to determine the role of hydride ions in these oxyhydride-supported metal catalysts. For Ru, H/D isotope studies show participation of lattice hydride in the catalytic cycle, while kinetic analysis shows reduced H_2 poisoning probably due to spillover, implying that the hydrogen-based MvK effect is still present. For Fe (and Co), the presence of hydride resulted in significantly lower activation energy and N_2 reaction order, likely due to strong electron donation from the oxyhydride support. This metal-dependent oxyhydride support effect was further verified by N_2 isotopic exchange experiments. In terms of activity, the $BaTiO_{2.5}H_{0.5}$ supports enhance the activity of $BaTiO_3$ by orders of magnitude; for Fe and Co the activity increases by a factor of 70~400, making them more active than conventional Ru catalysts of similar loading amount. These

perovskite-type oxyhydrides can also be easily modified in terms of *A*-site and *B*-site choice; the high potential for compositional variation as well as morphologies will expand the search for efficient catalysts for ammonia synthesis.

In *Chapter 3*, the oxyhydride were examined as a support material for Ni, Ru-based catalysts for CO_2 methantion reaction. The results shown that the $BaTiO_{2.4}H_{0.6}$ enhances the activity of $BaTiO_3$ by 2–7 times. Furthermore, Ni/$BaTiO_{3-x}H_x$ is also durable with its catalytic performance being kept for at least 10 hours under a water-rich environment. Kinetic analysis revealed that the lattice hydride improves hydrogen adsorption on the metal surface. We anticipate these perovskite oxyhydrides will shed new light on the design of high-efficiency metal-based catalysts for water-involved catalytic reactions.

In *Chapter 4*, gaseous hydrogen exchange and release experiments were analyzed using the Kissinger method to estimate the activation energy (E_a) for H/D exchange and H_2 release in $BaTiO_{3-x}H_x$ (x = 0.35–0.60) and $LaSrCoO_3H_{0.70}$. It is revealed that for each $BaTiO_{3-x}H_x$ at a given hydride concentration (x), both H/D exchange and H_2 release experiments provide similar E_a values. While for $BaTiO_{3-x}H_x$ with different x, the obtained E_a values significantly decrease with increasing x until around 0.4; beyond 0.4 it becomes nearly constant (200–220 kJ mol^{-1}). This observation suggests that the diffusion process in the low hydride concentration (x< 0.4) includes oxide as well as hydride diffusion, whereas for 0.4 <x (< 0.75) only hydride migrates, with second nearest-neighbour (2NN) jumps as a rate-determining process, which is supported by DFT calculations. The Kissinger analysis of $LaSrCoO_3H_{0.70}$ yielded a similar E_a of 170–190 kJ mol^{-1}, consistent with the 2NN hopping scenario. The presented method provides a facile tool for designing and improving hydride conductivity in oxyhydrides regardless of the presence of electronic conductivity.

References

1. Deutschmann, O.; Knözinger, H.; Kochloefl, K.; Turek, T., Heterogeneous Catalysis and Solid Catalysts. In *Ullmann's Encyclopedia of Industrial Chemistry*, Wiley-VCH Verlag GmbH & Co. KGaA: **2000**.

2. Norskov, J. K.; Bligaard, T.; Rossmeisl, J.; Christensen, C. H., *Nat. Chem.* **2009**, *1*, (1), 37–46.

3. Ertl, G., *J. Mol. Catal. A: Chem.* **2002**, *182–183*, 5–16.

4. Libuda, J.; Freund, H. J., *Surf. Sci. Rep.* **2005**, *57*, (7–8), 157–298.

5. Zhu, J.; Li, H.; Zhong, L.; Xiao, P.; Xu, X.; Yang, X.; Zhao, Z.; Li, J., *ACS Catal.* **2014**, *4*, (9), 2917–2940.

6. Peña, M. A.; Fierro, J. L. G., *Chem. Rev.* **2001**, *101*, (7), 1981–2018.

7. Zhu, H.; Zhang, P.; Dai, S., *ACS Catal.* **2015**, *5*, (11), 6370–6385.

8. Zhu, Y.; Zhang, S.; Ye, Y.; Zhang, X.; Wang, L.; Zhu, W.; Cheng, F.; Tao, F., *ACS Catal.* **2012**, *2*, (11), 2403–2408.

9. Vojvodic, A.; Medford, A. J.; Studt, F.; Abild-Pedersen, F.; Khan, T. S.; Bligaard, T.; Nørskov, J. K., *Chem. Phys. Lett.* **2014**, *598*, 108–112.

10. Aika, K.; Kumasaka, M.; Oma, T.; Kato, O.; Matsuda, H.; Watanabe, N.; Yamazaki, K.; Ozaki, A.; Onishi, T., *Appl. Catal.* **1986**, *28*, 57–68.

11. Behrens, M.; Studt, F.; Kasatkin, I.; Kühl, S.; Hävecker, M.; Abild-Pedersen, F.; Zander, S.; Girgsdies, F.; Kurr, P.; Kniep, B.-L.; Tovar, M.; Fischer, R. W.; Nørskov, J. K.; Schlögl, R., *Science* **2012**, *336*, (6083), 893–897.

12. Liu, J.; Li, C.; Wang, F.; He, S.; Chen, H.; Zhao, Y.; Wei, M.; Evans, D. G.; Duan, X., *Catal. Sci. Technol.* **2013**, *3*, (10), 2627.

13. Jia, C.; Gao, J.; Li, J.; Gu, F.; Xu, G.; Zhong, Z.; Su, F., *Catal. Sci. Technol.* **2013**, *3*, (2), 490–499.

14. Wang, Z.; Lin, J.; Wang, R.; Wei, K., *Catal. Commun.* **2013**, *32*, 11–14.

15. Kitano, M.; Inoue, Y.; Yamazaki, Y.; Hayashi, F.; Kanbara, S.; Matsuishi, S.; Yokoyama, T.; Kim, S. W.; Hara, M.; Hosono, H., *Nat. Chem.* **2012**, *4*, (11), 934–40.

16. Hara, M.; Kitano, M.; Hosono, H., *ACS Catal.* **2017**, 7, 2313–2324.

17. Wang, P.; Chang, F.; Gao, W.; Guo, J.; Wu, G.; He, T.; Chen, P., *Nat. Chem.* **2016**, *9*, 64–70.

18. Gao, W.; Wang, P.; Guo, J.; Chang, F.; He, T.; Wang, Q.; Wu, G.; Chen, P., *ACS Catal.* **2017**, *7*, (5), 3654–3661.

19. Kitano, M.; Inoue, Y.; Ishikawa, H.; Yamagata, K.; Nakao, T.; Tada, T.; Matsuishi, S.; Yokoyama, T.; Hara, M.; Hosono, H., *Chem. Sci.* **2016**, 7, 4036.

20. Kitano, M.; Kanbara, S.; Inoue, Y.; Kuganathan, N.; Sushko, P. V.; Yokoyama, T.; Hara, M.; Hosono, H., *Nat. Commun.* **2015**, *6*, 6731.

21. Kim, Y. J.; Kim, S. M.; Cho, E. J.; Hosono, H.; Yang, J. W.; Kim, S. W., *Chem. Sci.* **2015**, *6*, (6), 3577–3581.

22. Kim, Y. J.; Kim, S. M.; Hosono, H.; Yang, J. W.; Kim, S. W., *Chem. Commun.***2014**, *50*, (37), 4791–4794.
23. Abe, H.; Niwa, Y.; Kitano, M.; Inoue, Y.; Sasase, M.; Nakao, T.; Tada, T.; Yokoyama, T.; Hara, M.; Hosono, H., *J. Phys. Chem. C* **2017**, *121*, (38), 20900–20904.
24. Lu, Y.; Li, J.; Tada, T.; Toda, Y.; Ueda, S.; Yokoyama, T.; Kitano, M.; Hosono, H., *J. Am. Chem. Soc.* **2016**, *138*, (12), 3970–3973.
25. Ye, T.-N.; Lu, Y.; Li, J.; Nakao, T.; Yang, H.; Tada, T.; Kitano, M.; Hosono, H., *J. Am. Chem. Soc.* **2017**, *139*, (47), 17089–17097.
26. Wu, J.; Gong, Y.; Inoshita, T.; Fredrickson, D. C.; Wang, J.; Lu, Y.; Kitano, M.; Hosono, H., *Adv. Mater.* **2017**, *29*, 1700924.
27. Hayashi, F.; Toda, Y.; Kanie, Y.; Kitano, M.; Inoue, Y.; Yokoyama, T.; Hara, M.; Hosono, H., *Chem. Sci.* **2013**, *4*, (8), 3124.
28. Kobayashi, Y.; Hernandez, O. J.; Sakaguchi, T.; Yajima, T.; Roisnel, T.; Tsujimoto, Y.; Morita, M.; Noda, Y.; Mogami, Y.; Kitada, A.; Ohkura, M.; Hosokawa, S.; Li, Z.; Hayashi, K.; Kusano, Y.; Kim, J.; Tsuji, N.; Fujiwara, A.; Matsushita, Y.; Yoshimura, K.; Takegoshi, K.; Inoue, M.; Takano, M.; Kageyama, H., *Nat. Mater.* **2012**, *11*, (6), 507–11.
29. Sakaguchi, T.; Kobayashi, Y.; Yajima, T.; Ohkura, M.; Tassel, C.; Takeiri, F.; Mitsuoka, S.; Ohkubo, H.; Yamamoto, T.; Kim, J.; Tsuji, N.; Fujihara, A.; Matsushita, Y.; Hester, J.; Avdeev, M.; Ohoyama, K.; Kageyama, H., *Inorg. Chem.* **2012**, *51*, (21), 11371–11376.
30. Masuda, N.; Kobayashi, Y.; Hernandez, O.; Bataille, T.; Paofai, S.; Suzuki, H.; Ritter, C.; Ichijo, N.; Noda, Y.; Takegoshi, K.; Tassel, C.; Yamamoto, T.; Kageyama, H., *J. Am. Chem. Soc.* **2015**, *137*, (48), 15315–15321.
31. Yajima, T.; Takeiri, F.; Aidzu, K.; Akamatsu, H.; Fujita, K.; Yoshimune, W.; Ohkura, M.; Lei, S.; Gopalan, V.; Tanaka, K.; Brown, C. M.; Green, M. A.; Yamamoto, T.; Kobayashi, Y.; Kageyama, H., *Nat. Chem.* **2015**, 7, (12), 1017–1023.
32. Huang, B.; Corbett, J. D., *Inorg. Chem.* **1998**, *37*, (8), 1892–1899.
33. Hayashi, K.; Matsuishi, S.; Kamiya, T.; Hirano, M.; Hosono, H., *Nature* **2002**, *419*, (6906), 462–465.
34. Iwahara, H.; Uchida, H.; Ono, K.; Ogaki, K., *J. Electrochem. Soc.* **1988**, *135*, (2), 529–533.
35. Baikov, Y. M.; Shalkova, E. K., *J. Solid State Chem.* **1992**, *97*, (1), 224–227.
36. Bridges, C. A.; Fernandez-Alonso, F.; Goff, J. P.; Rosseinsky, M. J., *Adv. Mater.* **2006**, *18*, (24), 3304–3308.
37. Norby, T., Wideroe, Marius, Glockner, Ronny, Larring, Yngve, *Dalton Trans.* **2004**, (19), 3012–3018.
38. Rashkeev, S. N.; Fleetwood, D. M.; Schrimpf, R. D.; Pantelides, S. T., *Phys. Rev. Lett.* **2001**, *87*, (16), 165506.
39. Rashkeev, S. N.; Fleetwood, D. M.; Schrimpf, R. D.; Pantelides, S. T., *Appl. Phys. Lett.* **2002**, *81*, (10), 1839–1841.

40. Hayward, M. A.; Cussen, E. J.; Claridge, J. B.; Bieringer, M.; Rosseinsky, M. J.; Kiely, C. J.; Blundell, S. J.; Marshall, I. M.; Pratt, F. L., *Science* **2002**, *295*, (5561), 1882–1884.
41. Poulsen, F. W., *Solid State Ionics* **2001**, *145*, (1–4), 387–397.
42. T. Yamamoto, K. Shitara, S. Kitagawa, A. Kuwabara, M. Kuroe, K. Ishida, M. Ochi, K. Kuroki, K. Fujii, M. Yashima, C. M. Brown, H. Takatsu, C. Tassel and H. Kageyama, *Chem. Mater.* **2018**, DOI: 10.1021/acs.chemmater.7b04571.
43. Hempelmann, R.; Soetratmo, M.; Hartmann, O.; Wäppling, R., *Solid State Ionics* **1998**, *107*, (3–4), 269–280.
44. Bjørheim, T. S.; Kuwabara, A.; Ahmed, I.; Haugsrud, R.; Stølen, S.; Norby, T., *Solid State Ionics* **2010**, *181*, (3–4), 130–137.
45. Merinov, B.; Goddard, W., *J. Chem. Phys.* **2009**, *130*, (19), 194707.
46. Malikova, N.; Loong, C. K.; Zanotti, J. M.; Fernandez-Alonso, F., *J. Phys. Chem. C* **2007**, *111*, (17), 6574–6580.
47. Chen, Q.; Banyte, J.; Zhang, X.; Embs, J. P.; Braun, A., *Solid State Ionics* **2013**, 252, 2–6.
48. Huang, B.; Corbett, J. D., *J. Solid State Chem.* **1998**, *141*, (2), 570–575.
49. Huang, B.; Corbett, J. D., *Inorg. Chem.* **1998**, *37*, (8), 1892–1899.
50. Yamamoto, T.; Kageyama, H., *Chem. Lett.* **2013**, *42*, (9), 946–953.
51. Mikita, R.; Aharen, T.; Yamamoto, T.; Takeiri, F.; Ya, T.; Yoshimune, W.; Fujita, K.; Yoshida, S.; Tanaka, K.; Batuk, D.; Abakumov, A. M.; Brown, C. M.; Kobayashi, Y.; Kageyama, H., *J. Am. Chem. Soc.* **2016**, *138*, (9), 3211–3217.
52. Tomishige, K.; Chen, Y.-g.; Fujimoto, K., *J. Catal.* **1999**, *181*, (1), 91–103.
53. Seok, S.-H.; Choi, S. H.; Park, E. D.; Han, S. H.; Lee, J. S., *J. Catal.* **2002**, *209*, (1), 6–15.
54. Hayashi, K.; Sushko, P. V.; Shluger, A. L.; Hirano, M.; Hosono, H., *J. Phys. Chem. B* **2005**, *109*, (50), 23836–23842.
55. Bridges, C. A.; Darling, G. R.; Hayward, M. A.; Rosseinsky, M. J., *J. Am. Chem. Soc.* **2005**, *127*, (16), 5996–6011.
56. Kobayashi, G.; Hinuma, Y.; Matsuoka, S.; Watanabe, A.; Iqbal, M.; Hirayama, M.; Yonemura, M.; Kamiyama, T.; Tanaka, I.; Kanno, R., *Science* **2016**, *351*, (6279), 1314–1317.
57. Yajima, T.; Kitada, A.; Kobayashi, Y.; Sakaguchi, T.; Bouilly, G.; Kasahara, S.; Terashima, T.; Takano, M.; Kageyama, H., *J. Am. Chem. Soc.* **2012**, *134*, (21), 8782–8785.
58. Iwazaki, Y.; Suzuki, T.; Tsuneyuki, S., *J. Appl. Phys.* **2010**, *108*, (8), 083705.
59. Zhang, J.; Gou, G.; Pan, B., *J. Phys. Chem. C* **2014**, *118*, (31), 17254–17259.
60. Liu, X.; Bjorheim, T. S.; Haugsrud, R., *J. Mater. Chem. A* **2018**, *6*, 1454-1461.
61. Liu, X.; Bjorheim, T. S.; Haugsrud, R., *J. Mater. Chem. A* **2017**, *5*, (3), 1050–1056.
62. Fjellvåg, Ø. S.; Armstrong, J.; Vajeeston, P.; Sjåstad, A. O., *J. Phys. Chem. Lett.* **2018**, 353-358.

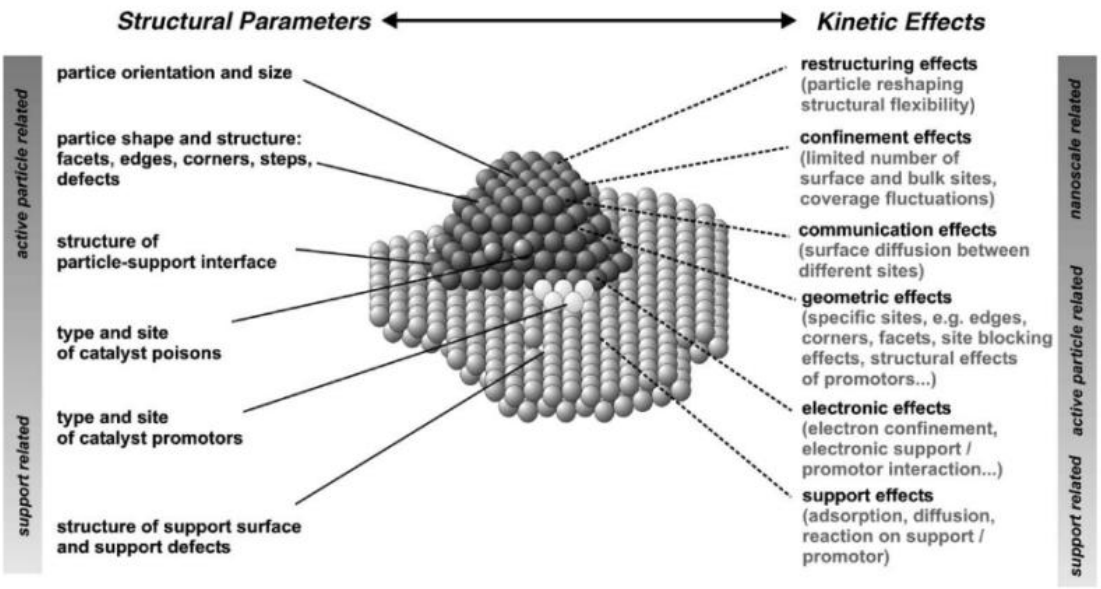

Figure 1. Structural parameters and kinetic effects on supported metal catalysts.[4]

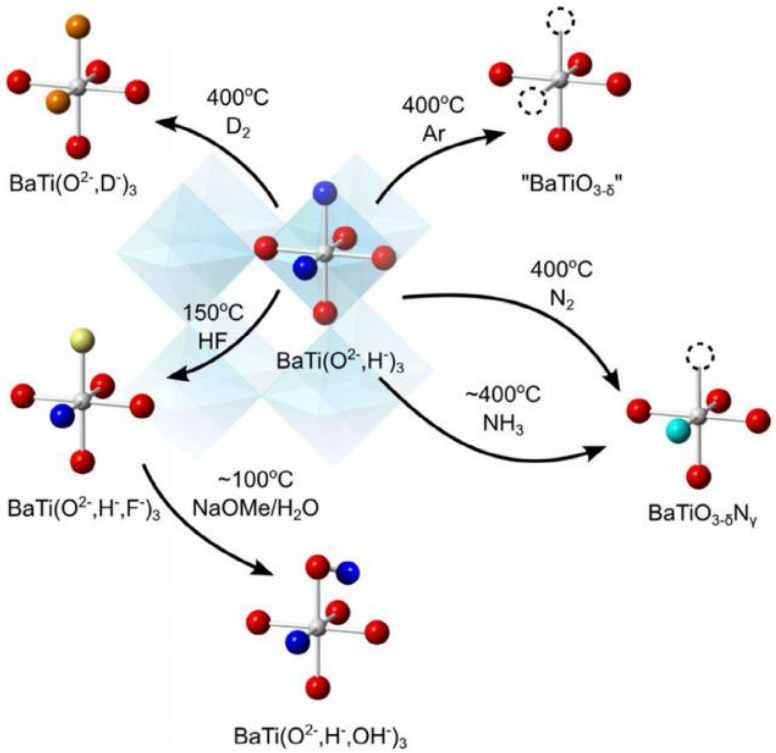

Figure 2. Different anion exchange routes starting from an oxyhydride.

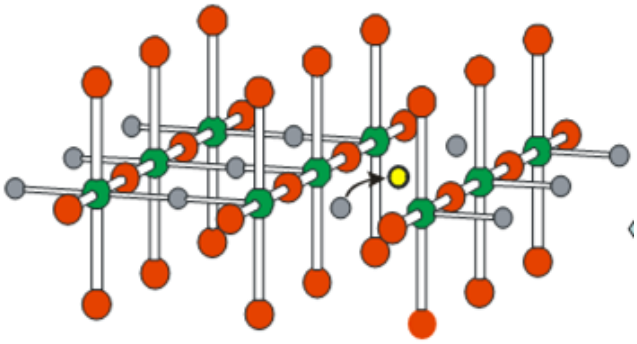

Figure 3. QENS study of hydride diffusion in $LaSrCoO_3H_{0.7}$.

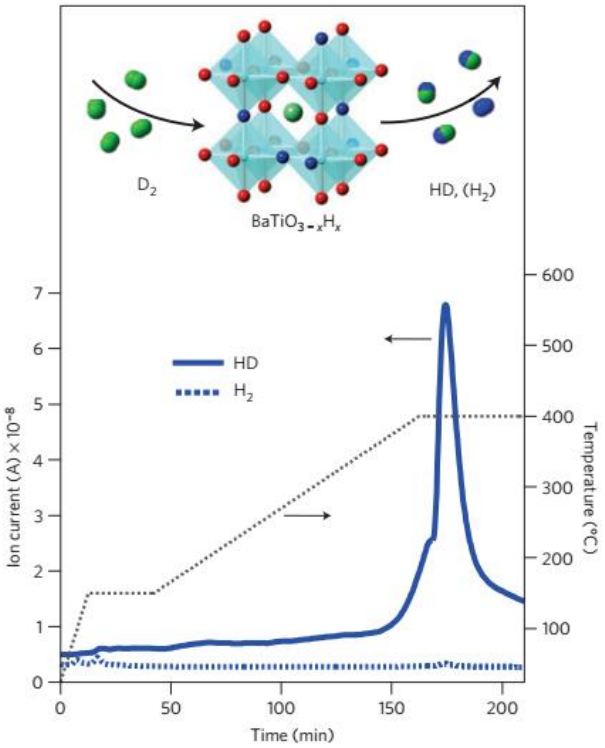

Figure 4. Mass spectrometry of gaseous species during deuteride exchange in $BaTiO_{3-x}H_x$.

Chapter 1. Titanium-based hydrides as heterogeneous catalysts for ammonia synthesis

1.1. Introduction

N_2 activation and conversion to NH_3 has been studied intensively. In terms of basic science, much research has been done to understand the biological process of N_2 fixation, while industrially, NH_3 synthesis is the starting step for various nitrogen-containing chemicals, including synthetic fertilizers. More recently, NH_3 has gathered attention as a convenient hydrogen carrier[1,2] or fuel,[3,4] necessary for implementing the hydrogen economy.

In terms of nitrogen activation by metal complexes, hydride complexes form a distinct class where strong reducing agents such as KC_8 or Na/Hg are not necessary to activate N_2. This has been reviewed extensively by Ballmann *et al.*[5] and Jia *et al*.[6] Hydride complexes of Co, Fe, Ru, Rh, Ir, Mn, Mo, Ni, Ti, Ta, and Nb have all been reported to form nitrogen complexes upon exposure to N_2 gas.[5,7] Preparing these transition metal hydride complexes sometimes requires highly reducing reagents such $NaBH_4$, but numerous Ti complexes require only H_2 gas at ambient conditions to form hydrides. One example demonstrating this reactivity is shown in Figure 1.1a, where a titanocene derivative forms a hydride complex in-situ, and then transforms to $((Me_4Cp)_2Ti)_2(\mu\text{-}N_2)$ under N_2.[8] One common aspect of catalysis for NH_3 synthesis in both homogeneous and heterogeneous states is the importance of multiple metal centers; as for titanium, Shima *et al.* recently demonstrated a polynuclear Ti complex with reactivity for H_2 and N_2 (shown in Figure 1.1b).[9] The initial $(CpMe_4SiMe_3)Ti(CH_2SiMe_3)_3$ complex reacts with H_2 gas to form a capped trinuclear titanium cluster, and further reaction with N_2 gas yields a nitride/imido/hydrido complex. Exposure to a mixture of N_2/H_2 also yields an imido-hydride complex cluster (see lower route of Figure 1.1b). While this is an extraordinary example of imido group formation from N_2 and H_2 gas, no NH_3 is formed.

Turning to solids, titanium metal is one of the few elements relatively prone to oxidative addition of H_2 to yield TiH_2,[10,11] whose fluorite-type structure shown in Figure 1.1c. As a related compound, we have recently reported the synthesis of a titanium-based perovskite oxyhydride, $BaTiO_{2.5}H_{0.5}$.[12] Using H/D exchange experiments, we have shown that the lattice H^- is thermolabile and can be exchanged with surrounding D_2 gas at 400 ˚C (Figure 1.1d). This exchange involves D_2 (H_2) bond dissociation, and hints that various hydrogenation reactions may be possible. In a more recent study, we have found that treatment with N_2 gas at the same temperature results in conversion to the oxynitride $BaTiO_{2.5}N_{0.2}$.[13] Combined, these results suggest that the oxyhydride is a useful material for the activation of diatomic H_2 and N_2.

However, despite these observations from complexes and the solid state, hydride-containing titanium compounds have not been investigated previously as heterogeneous catalysts. Here, we examine TiH_2 and $BaTiO_{2.5}H_{0.5}$ as ammonia synthesis catalysts under Haber-Bosch conditions, and find that they exhibit surprisingly robust catalytic activity.

1.2. Experimental section

1.2.1. $BaTiO_3$ and $BaTiO_{2.5}H_{0.5}$ catalysts A commercial sample of $BaTiO_3$ (Sakai Chemical Industry, particle size ~100 nm) was used as a reference catalyst. The catalyst $BaTiO_{2.5}H_{0.5}$ was synthesized by the CaH_2 reduction of this $BaTiO_3$ as reported previously.[12,13] $BaTiO_3$ and CaH_2 were mixed in a N_2-filled glovebox (1:3 molar ratio), pelletized (1.5 g, ϕ12 mm), and sealed in an evacuated (~10^{-2} Pa) pyrex tube (O.D. 20 mm, I.D. 14 mm, length ca. 12 cm) for 1 week at 560 ˚C. After reaction, the blue-black $BaTiO_{2.5}H_{0.5}$ (about 1 g) was split in two batches, and each was washed with NH_4Cl/methanol (0.1 M, 300 mL), and dried at 100 ˚C under vacuum. The amount of hydride in the sample can be verified directly or indirectly by a number of ways, such as TGA (oxidative atmosphere), Rietveld refinement of X-ray data, thermal desorption spectroscopy (TDS), and if available, neutron diffraction. Previous studies[12,13] show that all techniques give a consistent formula, and that the amount of anion vacancies was negligible. Commercial samples of TiH_2, CaH_2, TiO_2, and Ti_2O_3 were ball milled for 12 hours in a N_2-filled ZrO_2 pot. The milled powders were subsequently stored and handled under N_2.

1.2.2. NH_3 synthesis A 0.1 g sample of catalyst was suspended in a 3/8" stainless steel tube on a bed of quartz wool. Blank tests using the reactor tube and quartz wool did not give any measurable activity. Catalyst samples were initially treated with flowing H_2 (90 mL min^{-1}) at 400 ˚C (6 ˚C min^{-1} heating/cooling). Catalytic runs were then conducted at 5 MPa (gauge pressure), with a flow rate of 110 sccm. The synthesis gas composition was N_2:H_2:Ar = 22.5:67.5:10, unless otherwise noted (the Ar was initially intended to serve as an internal standard for calibrating a mass spectrometer). Commercially supplied gases (O_2 < 2 ppm, H_2O < 5 ppm) were purified with an in-line H_2O/O_2 filter to achieve *ppt*-level purity. Ammonia formation was quantified by an aqueous trap (1.87×10^{-5} M NH_4Cl, 333 mL) and an NH_3-selective electrode (Horiba X 5002A).

1.2.3. Kinetic studies Apparent activation energies were measured at 5 MPa, over 325–400 ˚C. For N_2 and H_2 reaction order measurements, gas compositions of N_2:H_2:Ar were 10:50:40, 16.7:50:33.3, 25:50:25, and 33.3:50:16.7 for determining the N_2 order, and 16.7:33.3:50, 16.7:50:33.3, 16.7:66.7:16.7 and 16.7:83.3:0 for determining the H_2 order. All measurements were conducted at 5 MPa, 400 ˚C at a flow rate of 110 sccm. Reaction

orders of NH_3 were determined by varying the conversion rate, achieved by changing the flow rate of the gas (22.5:67.5:10) between 50 mL min^{-1}, 110 mL min^{-1}, 150 mL min^{-1}, and 200 mL min^{-1}. This data was then analyzed by the method of Aika *et al*.[14] At the experimental conditions, the typical ammonia concentration is farless than 1%, thus being far from the equilibrium value (approx. 15% at 5 MPa, 400 ˚C).

1.2.4. Catalyst characterization XRD patterns were recorded on a Bruker Advance D8 diffractometer. Combustion elemental analysis for nitrogen was conducted at the School of Pharmacy, Kyoto University. XPS data were collected on an Ulvac-Phi MT-5500 instrument using Mg Kα radiation. The charge correction was conducted by shifting the O 1*s* peak to 529.5 eV. Surface areas were obtained by a Microtrac Bel BELSORP mini-II instrument using N_2 adsorption and the BET method.

1.2.5. Computational studies Calculations were performed using the CASTEP program[15] as provided within the Materials Studio package using the PBE-GGA exchange correlation functional. Initial *k*-mesh convergence and cut off energy tests were conducted on bulk structures, after which bulk lattice parameters were then optimized. Convergence criteria were 10^{-5} eV for energy, 0.03 eV/Å for force, 0.05 GPa for stress, and 0.001 Å for displacement. Slab structures with inversion symmetry (*P*-3*m*1) were then created, with slab and vacuum thicknesses roughly checked for energy convergence. Slab internal coordinates were thenrelaxed with the same criteria as above; this typically resulted in the outer two layer atoms slightly shifting their *z*-coordinates. The slabs were once again checked for *k*-mesh convergence (~0.026 $Å^{-1}$) and cut off energy (760 eV), implying that adsorption energies are converged to within at most 5 kJ mol^{-1}. The total electronic energy of gaseous N_2 was determined by placement in an 8Å × 8Å × 8Å box. Optimization of the N–N bond length resulted in 1.104 Å (experimental 1.11 Å). Dissociative heats of adsorption were defined as $(E_{slab}+E_{N2})-E_{slab+2N}$, and molecular heats of adsorption were defined as $(E_{slab}+E_{N2})-E_{slab+N2}$. Work functions were calculated by examining the electrostatic potential within the slab and at the vacuum separating the slabs. Slab models and adsorption sites are shown in the Supporting Information.

1.3. Results

1.3.1. Activity Figure 1.2a compares the activities of various catalysts for NH_3 synthesis at 400 ˚C under 5 MPa of flowing N_2/H_2 gas. As examples of typical Ru-based catalysts, the activities of $Ru/BaTiO_3$[16] and Cs-Ru/MgO catalysts[17,18] have been included; in our own experiments these catalysts produce 4.10 mmol g^{-1} h^{-1} and 2.7 mmol g^{-1} h^{-1} of NH_3, respectively (the Ru loading amount, ~0.9 wt %, is relatively low for our samples). In comparison, TiH_2 and $BaTiO_{2.5}H_{0.5}$ exhibit catalytic activities of 2.8 and 1.4 mmol g^{-1} h^{-1}, which is surprisingly on par with the aforementioned Ru catalysts. The surface area of the

TiH_2 and $BaTiO_{2.5}H_{0.5}$ powders were 10.5 $m^2\ g^{-1}$ and 15.6 $m^2\ g^{-1}$, so there is still room for improved activity by increasing the surface area. CaH_2, another hydride compound, is not active; we also note that $BaTiO_3$, TiO_2 and Ti_2O_3 powders are not catalytically active under our probed conditions. Hence, having the titanium center and hydride anion together seem to be critical for activity.

This result is rather different from recent reports with CaH_2 or LiH-based catalysts. For example, Kitano *et al* report the activity of Ru/CaH_2, but not for CaH_2 itself. For Ru/CaH_2, the high activity is due to Ru enabling the partial conversion of hydride to electride, i.e. $Ru/CaH_{2-x}(e^-)_x$, thus functioning as an electride catalyst.[19] In a separate report, Wang *et al* illustrate their use V, Cr, Mn, Fe, Co, Ni, and Ru metal mixed with LiH, with surprisingly high activities for all catalysts.[20] However, there have been no reports of catalytic activity from a single hydride compound. Reports on titanium-based materials are extremely scarce, being limited to a report on activity at atmospheric pressure exhibited by TiN nanoparticles.[21]

Figures 1.2b and 1.2c show the cumulative amounts of synthesized NH_3 as a function of time. The linear increase shows that the catalytic activity is stable over many hours. The horizontal dotted line indicates the amount of ammonia expected based on the simple decomposition of the catalyst, taking into account the amount of hydride. Since the activity is sustained at a constant rate over TON = 1, the generation of NH_3 is indeed catalytic, and the stability for TiH_2 has been confirmed up to 7 days (Figure 1.2e).

During NH_3 synthesis, it is quite possible that the hydrides partially convert to nitrides. We combined a variety of techniques to estimate the bulk and surface composition of the catalysts after the NH_3 synthesis reactions. The XRD patterns in Figure 1.3a show no change for $BaTiO_{2.5}H_{0.5}$ before and after NH_3 synthesis; however, a close examination revealed small changes in lattice parameters (Table 1.1) and relative peak intensities. We note in our previous publications that $BaTiO_{2.5}H_{0.5}$ is found to convert to an oxynitride(hydride) in pure N_2 (or NH_3) atmosphere at similar temperatures, depending on the temperature.[13, 22] Here, since the gaseous environment consists of both N_2 and H_2, an oxyhydride-nitride composition somewhat reflecting this mixed N_2/H_2 environment can be expected. A Rietveld refinement of the X-ray data (Table 1.1) gives results consistent with hydrogen being partially replaced by nitrogen, and combustion analysis of nitrogen concludes that the composition after catalysis to be approximately $BaTiO_{2.5}N_{0.2}H_{0.3}$. A separate control experiment using $BaTiO_{2.5}N_{0.3}$ as a catalyst found no activity; hence, the initial presence of hydride in the catalyst phase is critical.

We have also used X-ray photoelectron spectroscopy (XPS) to probe the surface. Results are shown in Figures 1.3d~f. The blue traces (*i*~*iii*) indicate spectra for $BaTiO_3$, $BaTiO_{2.5}H_{0.5}$, and post-reaction $BaTiO_{2.5}H_{0.5}$. The Ti 2*p* spectra (Figure 1.3d) appear similar, but a slight shoulder to the right of the peak at 458 eV indicates a slightly reduced surface

for $BaTiO_{2.5}H_{0.5}$ and post-reaction $BaTiO_{2.5}H_{0.5}$ (*ii*, *iii*) compared to $BaTiO_3$ (*i*). As expected, there is no appreciable change in the O 1*s* spectra. A small N 1*s* peak is observed, however, after NH_3 synthesis (Figure 1.3f, *iii*). Integrating the O 1*s* and N 1*s* peaks yields an atomic O/N ratio of 10:1, which is close to the bulk $BaTiO_{2.5}N_{0.2}H_{0.3}$ formula obtained previously.

The TiH_2 catalyst before and after NH_3 synthesis was also characterized in a similar manner. The XRD shown in Figure 1.3b shows no appreciable change; the peaks remain characteristic of a TiH_2 fluorite phase. Close examination of the region shown in Figure 1.3c shows a minute peak possibly from TiN, signifying potential nitridation of the surface. This is confirmed by the XPS spectra (Figure 1.3f, *v*~*vi*); the N 1*s* signal has increased slightly in intensity as a result of conducting NH_3 synthesis. The large N 1*s* signal observed even before NH_3 synthesis (Figure 1.3f, *v*) is due the ball milling step; the powder was sealed in a ball mill pot within a N_2-filled glove box. Ball milling the TiH_2 powder (commercially obtained) was necessary in order to reduce the particle size and expose a non-oxidized TiH_2 surface. This surface oxide of the initial TiH_2 particles is quite evident in the O 1*s* spectra (Figure 1.3e *iv*), but decreases substantially after ball milling (Figure 1.3e, *v*). Despite the large N 1*s* peak after ball milling, the catalyst overall is still characterized as TiH_2, as demonstrated by the XRD pattern (Figure 1.3b,c), combustion elemental analysis showing only trace nitrogen content (0.66 wt% N), and the further increase of N 1*s* intensity during NH_3 synthesis. Furthermore, we have determined in a separate control experiment that TiN of the same particle size (i.e. ball milled) is not catalytically active for NH_3 synthesis. Previously, Kumagai *et al.* reported a TiN-carbon nanocomposite (399 $m^2\ g^{-1}$) with a modest activity (31 μmol $g^{-1}\ h^{-1}$ at atmospheric pressure).[21] However, despite the difference in reaction pressure, our own results comparing ball milled TiN and TiH_2 show a clear difference in terms of activity under equivalent conditions.

These results show that for both catalysts, during the reaction the catalyst surface is an oxyhydride-nitride composition, where the presence of hydride is a key to catalytic activity (despite the change in bulk/surface compositions, for this paper we refer to the catalysts by their initial composition for convenience). Although there is some partial nitridation, a significant amount of hydride remains, due to the equilibrium brought by surrounding H_2 gas and the consequent hydrogenation of the nitride species. Aside from the equilibrium due to the H_2 gas, excessive nitridation may also be kinetically sluggish. Gradual surface nitride accumulation may be an issue for catalyst longevity, but as shown in Figures 1.2b-d, we do not see any deactivation within the time frame of our experiments.

1.3.2. Kinetics Heterogeneous catalysts for ammonia synthesis have been often compared by their activation energies and reaction orders. In order to compare the nature of the catalyst with other examples, the activation energy and reaction orders with

respect to N_2, H_2, and NH_3 are plotted in Figures 1.4a~d. The activation energy, obtained over a range of 325~400 ˚C at 5 MPa for both hydride catalysts is 70~80 kJ mol^{-1}. Comparison with other titanate systems is not possible as there are very few reports, but most standard Ru catalysts have activation energies in the region of 80~130 kJ mol^{-1}. Hence, the activation energy for our catalyst is reasonably low. For example, Cs-Ru/MgO has been reported to have an activation energy of 109 kJ mol^{-1},[23] and for Ru/$BaTiO_3$, 130~90 kJ mol^{-1} has been reported,[24,25] while more recently, exceptionally low values (such as 40~60 kJ mol^{-1}) for Ru/C12A7:e^- have been suggested to imply alternate rate-limiting steps.[25,26] The reaction orders on N_2, H_2, and NH_3 (α, β, and γ, respectively) give insights into the catalytic behavior. For most conventional catalysts, α is close to 1, being related to the fact that the rate-limiting step is the unimolecular cleavage reaction of an adsorbed N_2 species. As seen in Figure 1.4b, while there is some scatter in the data, the N_2 reaction order for TiH_2 is quite low, 0.5±0.2. For $BaTiO_{2.5}H_{0.5}$ a higher value is obtained, 0.84±0.07. Such low reaction orders (~0.5) have only been reported recently by Kitano and Hosono *et al*, with Ru/C12A7:e^- (α = 0.46),[19] Ru/Ca_2N:e^- (α = 0.53),[19] and Ru/CaH_2 (α = 0.55).[19] These catalysts are all supported Ru catalysts, making direct comparisons precarious, but no other titanium-based catalysts have been reported before. The role of hydride in this aforementioned catalysts is not entirely clear either, as Ru/C12A7:H^- has a reaction order of 1.00, unlike that of Ru/C12A7:e^-, Ru/CaH_2 or TiH_2. In these electride catalysts with $\alpha \approx 0.5$, alternate rate-limiting steps (such as N-H bond formation) have been proposed.[26] It is notable that in our presented results, an equally low α has been obtained in the absence of Ru or any electride support. The elementary steps on TiH_2 could be quite different from conventional Ru (or Fe) catalysts, so the rather low N_2 reaction order requires further consideration to be explained properly.

The reaction order on H_2, β (Figure 1.4c), is often important from a practical perspective since for noble metal catalysts it represents the degree of hydrogen poisoning. At the high pressures encountered under Haber-Bosch conditions, Ru catalysts suffer from excessive adsorption of H_2 on the surface, decreasing the overall reaction rate, leading to negative values of β. For example, for Cs-Ru/MgO, β = -0.9.[23] Naturally, changing the catalytic element from Ru to Ti in our system eliminates this hydrogen poisoning; for TiH_2, β = 1.1±0.1, and for $BaTiO_{2.5}H_{0.5}$, β = 0.53±0.08. Both TiH_2 and the barium titanate oxyhydride-nitride system can adopt variable H stoichiometry.[12,27–29] This may also be a contributing factor, by providing adequate spillover capacity/pathways for the active sites to avoid hydrogen poisoning. Such an effect has been reported in cage-structured catalysts Ru/C12A7:e^- previously.[25] The reaction order on NH_3 (γ), with data plotted in Figure 1.4d, has been obtained by varying the flow rate of the N_2/H_2 feed gas. The values for $BaTiO_{2.5}H_{0.5}$ and TiH_2, –1.2±0.2 and –1.9±0.1, are strongly negative and are closer to Fe catalysts rather than Ru catalysts. While the literature concerning NH_3 orders is not

extensive, Fe/C and KM1 have reported values of –1.0, –1.5, respectively;[30] while some Ru catalysts have reported values of 0.0 (for Cs-Ru/MgO),[23] or –0.25, (for Ru/C12A7:O^{2-}).[25,26] Some of the more recent electride/hydride-supported Ru catalysts appear to have slightly more negative orders, such as Ru/C12A7:e^- (–1.00),[25] or Ru/Ca_2N:e^- (–1.03),[19] but it is quite evident that with the strongly negative orders, the titanium hydride-based systems have surfaces which interact quite strongly with the product ammonia.

1.3. Discussion

The results in Figure 1.2 tell us that the choice of both titanium and hydride seem to give rise to the catalytic activity, and while there are analogous cases in the literature, there are not any other Ti-based catalysis to make direct comparisons. As mentioned before, a titanium hydride cluster was shown to react with gaseous N_2 to form an imido-nitride complex, but with no NH_3 production.[9] In terms of the solid state, the closest analogy may be that reported by Vettraino *et al.*[31] Here, mesoporous TiO_2 was impregnated by a zero-valent bis(toluene) titanium complex, after which the ligand was removed by thermal treatment. This led to the formation of a titanium nitride species due to reaction with ambient N_2. Reaction of the nitride with residual H_2O in the framework led to the non-catalytic formation of NH_3, observed by IR and NMR. In a further development, a catalytic cycle based on an *in-situ* reduced Ta_2O_5 catalyst surface has been reported by Yue *et al*[32,33] with an activity of ~1 μmol g^{-1} h^{-1} at 350 ˚C, atmospheric pressure. Here, Ru or Pd was supported on Ta_2O_5; the supported metal is thought to dissociate H_2, which then spills over and partially reduces the Ta_2O_5 surface. N_2 activation on this reduced Ta_2O_5 surface is used to explain the unusual activity demonstrated with Pd/Ta_2O_5 and the very low activation energy (9 kJ mol^{-1}).

Recently, Wang *et al.* reported on catalysis using various transition metals combined with LiH,[20] and this system offers interesting insight into our own catalysts. The various transition metal-LiH catalysts have reaction orders quite similar to TiH_2 (or $BaTiO_{2.5}H_{0.5}$); that is, a low N_2 order ($\alpha \approx 0.5$), positive H_2 order ($\beta \approx 1$), and strongly negative NH_3 order ($\gamma < -1$). LiH alone cannot dissociate N_2, hence, N_2 is dissociated on the transition metal surface, and then transferred to LiH; here it is hydrogenated to the final NH_3. The N_2 dissociation step is reasonably fast such that the transfer and hydrogenation on the LiH phase becomes the rate-determining step, and the activation energy (46~64 kJ mol^{-1}) is reflective of this. It is quite possible that TiH_2 and $BaTiO_{2.5}H_{0.5}$ function in a similar way.

Titanium, being an early transition metal, has a high Ti–N bond strength, making the dissociative adsorption of N_2 facile. Conventional knowledge regarding ammonia synthesis shows a trend (i.e. the scaling relationship) between metal-nitrogen bond strengths and activity,[20,34,35] and the Ti–N bond is regarded as too strong for a catalytic

ammonia synthesis as an inactive surface nitride is formed. These metal-nitrogen bond strengths usually concern Ti in the *metallic* state, and at a first glance, it seems possible that for titanium hydride, the Ti–N bond has been weakened. It is not trivial to gain a complete picture of the mechanism, but some simple DFT calculations offer us answers to focused questions. In other words, does the incorporationof hydride in Ti weaken the otherwise excessively strong Ti–N bond?

To answer this, we have performed calculations concerning N_2 adsorption, on bare surfaces of Ti (hcp) 001, TiN (fcc) 111, and TiH_2, (fcc) 111; Ti-terminated surfaces were examined (see Supporting Information for structural discussions). All three of these surfaces are close-packed Ti surfaces, with the major difference being the presence (or absence) of sub-surface hydride or nitride. Comparing the adsorption heats on these hypothetical surfacesallows us to focus on electronic effects of hydride on Ti–N bond strength and N_2 activation, while more realisitic, complex surfaces would illuminate how surface hydride may directly take part in atom transfer reactions.

Table 1.2 shows our results. 3-fold adsorption sites were chosen, and due to variations in stacking, two sites are possible, site A and B (see Figures 1.5 and 1.6 for details). The dissociative heat of adsorption reflects the Ti–N bond strength. The calculated dissociative heat of adsorption on Ti is 443~460 kJ mol^{-1}, which agrees reasonably with previously reported 481 kJ mol^{-1}.[34] Unpromoted Ru metal has a negative calculated heat of adsorption, also reported and explained previously.[34] For the TiH_2 species, we see that two sites on the 111 surface have adsorption energies of 534 kJ mol^{-1} and 374 kJ mol^{-1}. The dissociative adsorption energy of N_2 on Fe has been placed at 205~293 kJ mol^{-1} so even with lattice hydride,[34] the Ti–N bond remains quite strong, contrary to our initial hypothesis.

We have also calculated work functions of the bare surfaces and N–N bond lengths for end-on molecular adsorption of N_2. These two parameters may be taken as an indication of how much back donation from the Ti surface to the N_2 molecule there is.

The N–N bond length of N_2 adsorbed on TiH_2 is elongated (1.173 Å) when compared to on Ti (1.165Å) or unpromoted Ru (1.138Å), but this value is still somewhat small when compared to the most activated adsorption sites on more complex surfaces of Co_3Mo_3N[36,37] and Ru/C12A7:e^-.[38] The work function for the TiH_2 111 surface is 3.96 eV, fairly high compared to C12A7:e^- (~2.4)[39] and simply closer to Ti (3.99 eV) or Ru (4.67 eV).

These calculations show that indirect electronic effects from lattice hydride do not affect surface adsorption enough to warrant the results we see. In turn, we must now examine other hypotheses with more realistic models. In a recent paper, Li *et al* find that sub-surface incorporation of nitrogen into Ti (i.e. surface nitride formation) is energetically favored;[40] such an approach needs to be considered for our case also. We

have also not yet examined more complex (i.e. lower index) surfaces, in the presence of surface hydride/nitride. The key to understanding the reaction orders and activity of TiH_2 probably lies here, with the complex interplay of lattice/bulk hydride and nitride. Another possibility that could be investigated isdirect hydrogenation of N_2, as found in the associative N_2 fixation mechanism of nitrogenase.

1.4. Conclusions

In conclusion, when viewed from a wider perspective, the catalytic activity of TiH_2 and $BaTiO_{2.5}H_{0.5}$ is interesting from two directions. On one hand, extensive research on N_2-activating complexes has resulted in a number of conclusions, such the choice of early transition metals, which have strong metal-nitrogen bonds to assist in N≡N cleavage, and the use of hydride groups to eliminate strongly reducing agents.[5,6,41] Additionally, studies have shown that multi-nuclear clusters tend to be effective, as they are well-suited for supplying the multiple electrons required in the stepwise reduction of N_2.[41–43] The solid state nature of our own catalysts provides a locked multi-atom environment on the surface, and thus can be seen as an extension of these cluster systems.

On the other hand, the conclusion that a hydride compound is effective for NH_3 synthesis is also interesting from the field of heterogeneous catalysis. The direct exchange with lattice species in catalysis (the Mars–van Krevelen mechanism[44]) is quite common in oxides, where oxides are inherently good catalysts for oxidation reactions, given their ability to easily adsorb oxygen on surface vacancies, or even exchange their bulk lattice oxygen. Apart from oxides for oxidation, halides and sulfides, and a nitride have also been sporadically examined for halogenation,[45,46] hydrodesulfurization,[47,48] and ammonia synthesis[49,50] reactions. It is then natural to ask the question whether could a hydride compound function as a hydrogenation catalyst, and our results show that this is indeed possible for N_2 hydrogenation to ammonia. From the perspective of ammonia synthesis, finding new catalysts to break the scale limitation have garnered much attention recently.[20,35] While the activity we observe here is modest,when compared to industrial catalysts (KM1 or Ba-Ru/C), our Ti–H solid system is one example of a new composition that may be a starting point for breaking scaling rules, and ultimately lead to cheaper catalysts working at lower temperatures and pressures.

References

1. Klerke, A.; Christensen, C. H.; Nørskov, J. K.; Vegge, T., *J. Mater. Chem.* **2008**, *18*, 2304.
2. Yin, S. F.; Xu, B. Q.; Zhou, X. P.; Au, C. T., *Appl. Catal. A Gen.* **2004**, *277*, 1–9.
3. Rees, N. V.; Compton, R. G., *Energy Environ. Sci.* **2011**, *4*, 1255.
4. Afif, A.; Radenahmad, N.; Cheok, Q.; Shams, S.; Kim, J. H.; Azad, A. K., Ammonia-fed fuel cells: A comprehensive review. *Renewable and Sustainable Energy Reviews*, **2016**, *60*, 822–835.
5. Ballmann, J.; Munhá, R. F.; Fryzuk, M. D., *Chem. Commun.* **2010**, *46*, 1013–1025.
6. Jia, H.-P.; Quadrelli, E. A., *Chem. Soc. Rev.* **2014**, *43*, 547–564.
7. Avenier, P.; Taoufik, M.; Lesage, A.; Solans-Monfort, X.; Baudouin, A.; de Mallmann, A.; Veyre, L.; Basset, J.-M.; Eisenstein, O.; Emsley, L.; Quadrelli, E. A., *Science* **2007**, *317*, 1056–1060.
8. de Wolf, J. M.; Blaauw, R.; Meetsma, A.; Teuben, J. H.; Gyepes, R.; Varga, V.; Mach, K.; Veldman, N.; Spek, A. L., *Organometallics* **1996**, *15*, 4977–4983.
9. Shima, T.; Hu, S.; Luo, G.; Kang, X.; Luo, Y.; Hou, Z., *Science* **2013**, *340*, 1549–1552.
10. Yakel, H. L. J., *Acta Crystallogr.* **1958**, *11*, 46–51.
11. Setoyama, D.; Matsunaga, J.; Muta, H.; Uno, M.; Yamanaka, S., *J. Alloys Compd.* **2004**, *381*, 215–220.
12. Kobayashi, Y.; Hernandez, O. J.; Sakaguchi, T.; Yajima, T.; Roisnel, T.; Tsujimoto, Y.; Morita, M.; Noda, Y.; Mogami, Y.; Kitada, A.; Ohkura, M.; Hosokawa, S.; Li, Z.; Hayashi, K.; Kusano, Y.; Kim, J. eun; Tsuji, N.; Fujiwara, A.; Matsushita, Y.; Yoshimura, K.; Takegoshi, K.; Inoue, M.; Takano, M.; Kageyama, H., *Nat. Mater.* **2012**, *11*, 507–511.
13. Masuda, N.; Kobayashi, Y.; Hernandez, O.; Bataille, T.; Paofai, S.; Suzuki, H.; Ritter, C.; Ichijo, N.; Noda, Y.; Takegoshi, K.; Tassel, C.; Yamamoto, T.; Kageyama, H., *J. Am. Chem. Soc.* **2015**, *137*, 15315–15321.
14. Aika, K.; Kumasaka, M.; Oma, T.; Kato, O.; Matsuda, H.; Watanabe, N.; Yamazaki, K.; Ozaki, A.; Onishi, T., *Appl. Catal.* **1986**, *28*, 57–68.
15. Clark Stewart, J.; Segall Matthew, D.; Pickard Chris, J.; Hasnip Phil, J.; Probert Matt, I. J.; Refson, K.; Payne Mike, C., *Zeitschrift für Krist.* **2005**, *220*, 567–570.
16. Wang, Z.; Lin, J.; Wang, R.; Wei, K., *Catal. Commun.* **2013**, *32*, 11–14.
17. O Hinrichsen, F. Rosowski, A. Hornung, M. Muhler, G. E. *J. Catal.* **1997**, *165*, 33–44.
18. Bielawa, H.; Hinrichsen, O.; Birkner, A.; Muhler, M., *Angew. Chem. Int. Ed.* **2001**, *40*, 1061–1063.
19. Kitano, M.; Inoue, Y.; Ishikawa, H.; Yamagata, K.; Nakao, T.; Tada, T.; Matsuishi, S.; Yokoyama, T.; Hara, M.; Hosono, H., *Chem. Sci.* **2016**, *7*, 4036–4043.
20. Wang, P.; Chang, F.; Gao, W.; Guo, J.; Wu, G.; He, T.; Chen, P. *Nat. Chem.* **2017**, *9*, 64–70.
21. Kumagai, H.; Takanabe, K.; Kubota, J.; Domen, K., *Bull. Chem. Soc. Jpn.* **2015**, *88*, 584–590.

22. Yajima, T.; Takeiri, F.; Aidzu, K.; Akamatsu, H.; Fujita, K.; Yoshimune, W.; Ohkura, M.; Lei, S.; Gopalan, V.; Tanaka, K.; Brown, C. M.; Green, M. A.; Yamamoto, T.; Kobayashi, Y.; Kageyama, H., *Nat. Chem.* **2015**, *7*, 1017–1023.
23. Rosowski, F.; Hornung, A.; Hinrichsen, O.; Herein, D.; Muhler, M.; Ertl, G., *Appl. Catal. A Gen.* **1997**, *151*, 443–460.
24. Horiuchi, Y.; Kamei, G.; Saito, M.; Matsuoka, M., *Chem. Lett.* **2013**, *42*, 1282–1284.
25. Kitano, M.; Inoue, Y.; Yamazaki, Y.; Hayashi, F.; Kanbara, S.; Matsuishi, S.; Yokoyama, T.; Kim, S.-W.; Hara, M.; Hosono, H., *Nat. Chem.* **2012**, *4*, 934–940.
26. Kitano, M.; Kanbara, S.; Inoue, Y.; Kuganathan, N.; Sushko, P. V; Yokoyama, T.; Hara, M.; Hosono, H., *Nat. Commun.* **2015**, *6*, 6731.
27. Numakura, H.; Koiwa, M.; Asano, H.; Izumi, F., *Acta Metall.* **1988**, *36*, 2267–2273.
28. Qadri, S. B.; Skelton, E. F.; Nagumo, M.; Webb, A. W.; Lynch, F. E.; Marmaro, R. W., *Phys. Rev. B* **1992**, *46*, 1193–1194.
29. Wang, K.; Kong, X.; Du, J.; Li, C.; Li, Z.; Wu, Z., *CALPHAD Comput. Coupling Phase Diagrams Thermochem.* **2010**, *34*, 317–323.
30. Hagen, S.; Barfod, R.; Fehrmann, R.; Jacobsen, C. J. H.; Teunissen, H. T.; Chorkendorff, I., *J. Catal.* **2003**, *214*, 327–335.
31. Vettraino, M.; Trudeau, M.; Lo, A. Y. H.; Schurko, R. W.; Antonelli, D., *J. Am. Chem. Soc.* **2002**, *124*, 9567–9573.
32. Yue, C.; Trudeau, M.; Antonelli, D., *Chem. Commun.* **2006**, 1918–1920.
33. Yue, C.; Qiu, L.; Trudeau, M.; Antonelli, D., *Inorg. Chem.* **2007**, *46*, 5084–5092.
34. *Ammonia Catalysis and Manufacture*; Nielsen, A., Ed.; Springer-Verlag: Berlin, 1995.
35. Vojvodic, A.; Medfored, A. J.; Studt, F.; Abild-Pedersen, F.; Khan, T. S.; Bligaard, T.; Nørskov, J. K., *Chem. Phys. Lett.* **2014**, *598*, 108–112.
36. Zeinalipour-Yazdi, C. D.; Hargreaves, J. S. J.; Catlow, C. R. A., *J. Phys. Chem. C* **2015**, *119*, 28368–28376.
37. Zeinalipour-Yazdi, C. D.; Hargreaves, J. S. J.; Catlow, C. R. A., *J. Phys. Chem. C* **2016**, *120*, 21390–21398.
38. Kuganathan, N.; Hosono, H.; Shluger, A. L.; Sushko, P. V., *J. Am. Chem. Soc.* **2014**, *136*, 2216–2219.
39. Toda, Y.; Yanagi, H.; Ikenaga, E., *Adv. Mater.* **2007**, *19*, 3564–3569.
40. Li, L.; Meng, F.-L.; Hu, X.-Y.; Qiao, L.; Sun, C. Q.; Tian, H.-W.; Zheng, W.-T., *RSC Adv.* **2016**, *6*, 14651–14657.
41. Bazhenova, T. A.; Shilov, A. E., *Coord. Chem. Rev.* **1995**, *144*, 69–145.
42. Pool, J. a; Lobkovsky, E.; Chirik, P. J., *Nature* **2004**, *427*, 527–530.
43. Gambarotta, S.; Scott, J., *Angew Chem. Int. Ed.* **2004**, *43*, 5298–5308.
44. Doornkamp, C.; Ponec, V., *J. Mol. Catal. A Chem.* **2000**, *162*, 19–32.
45. Brezneva, N. E.; Roginsky, S. Z., *Usp. Khim.* **1938**, *7*, 1503.

46. Roginsky, S. Z., In *Geterogenny kataliz v chim-promyslennosti, Materials of the All-Union Conference on Catalysis*; The State Publishing House for the Scientific and Technical Literature: Moscow, **1955**; p. 73.
47. Topsøe, H.; Clausen, B. S.; Massoth, F. E., *Catalysis, Science and Technology, Vol. 11*; Anderson, J. R.; Boudart, M., Eds.; Springer: Berlin (New York/Heidelberg), **1996**.
48. Pecoraro, T. A.; Chianelli, R. R., *J. Catal.* **1981**, *67*, 430.
49. McKay, D.; Gregory, D. H.; Hargreaves, J. S. J.; Hunter, S. M.; Sun, X., *Chem. Commun.* **2007**, 3051–3053.
50. Hunter, S. M.; Gregory, D. H.; Hargreaves, J. S. J.; Richard, M.; Duprez, D.; Bion, N., *ACS Catal.* **2013**, *3*, 1719–1725.

Table 1.1. Crystallographic parameters of $BaTiO_{2.5}H_{0.5}$ catalyst before and after NH_3 synthesis.

Compound	Atom	Site	*x*	*y*	*z*	Occ.	$100U_{iso}$
$BaTiO_{2.44}H_{0.56}$	Ba	1*b*	0.5	0.5	0.5	1	0.847(9)
Pm–3*m*	Ti	1*a*	0	0	0	1	0.98(2)
a = 4.04092(3) Å	O/H	3*d*	0.5	0	0	0.815(5)	1.49(9)
R_{wp} = 5.06%, R_p = 3.76%, χ^2 = 2.21							
$BaTi(O,N)_{2.69}H_{0.31}$	Ba	1*b*	0	0	0	1	0.87(1)
P4mm	Ti	1*a*	0.5	0.5	0.521(2)	1	1.09(8)
a = 4.01662(6) Å	(O,N)/H	1*a*	0.5	0.5	0.02(1)	0.898(6)	–0.1(2)
c = 4.0236(1) Å	(O,N)/H	2*c*	0.5	0	0.557(4)	0.102(6)	–0.1(2)
R_{wp} = 4.62%, R_p = 3.54%, χ^2 = 1.81							
$BaTi(O,N)_{2.74}H_{0.26}$	Ba	1*b*	0	0	0	1	0.88(1)
P4mm	Ti	1*a*	0.5	0.5	0.529(2)	1	0.8(1)
a = 4. 01664(6) Å	(O,N)/H	1*a*	0.5	0.5	0.006(5)	0.912(6)	1.00
c = 4.0236(1) Å	(O,N)/H	2*c*	0.5	0	0.537(2)	0.088(6)	1.00
R_{wp} = 4.65%, R_p = 3.55%, χ^2 = 1.83							

Table 1.2. Calculated adsorption heats on close-packed surfaces, N–N distances, and work functions.

Ads. Site[a]	Heat of ads.[b] (kJ mol^{-1})		N–N dist. (Å)	W. F.[c] (eV)
	Diss.	End-on N_2		
Ru-A	-114	-136	1.138	4.67
Ru-B	-66	-165	1.144	
Ti-A	443	95	1.162	3.99
Ti-B	460	86	1.160	
TiH_2-A	534	142	1.173	3.96
TiH_2-B	374	99	1.162	
TiN-A	356	97	1.159	4.22
N_2 (gas)	–	–	1.104	–

[a] sites as defined in Figures. 1.5 and 1.6; [b] see experimental details for definition; [c] work function of bare surface.

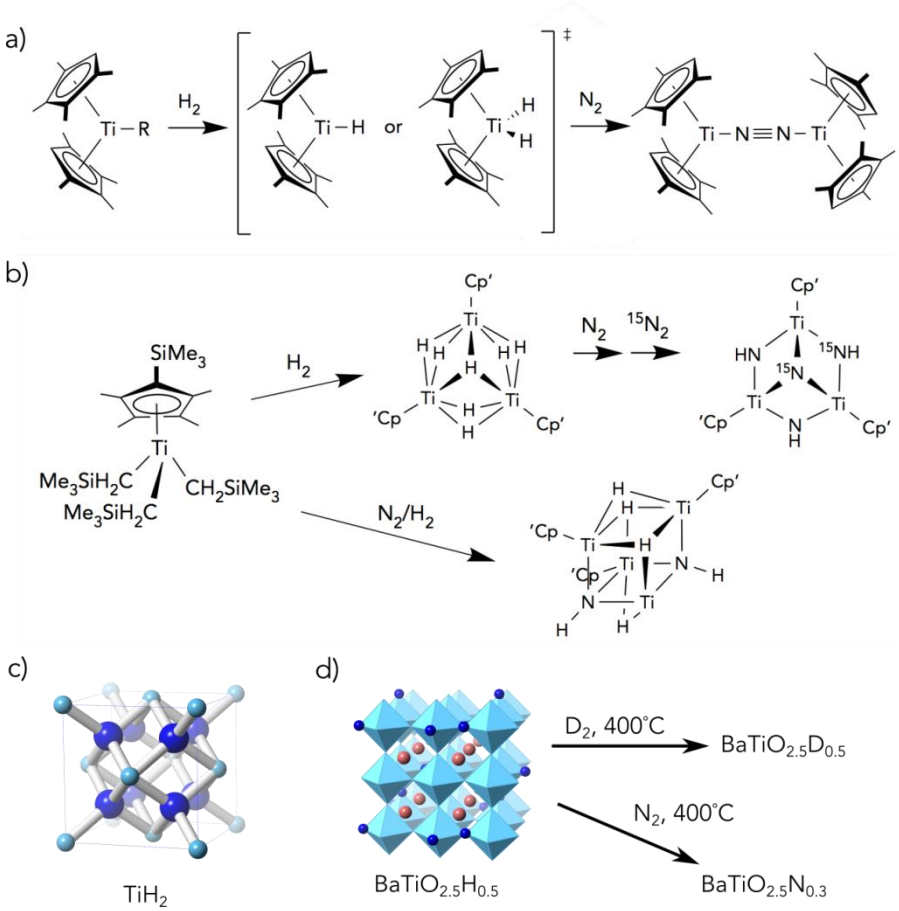

Figure 1.1. Reaction schemes and relevant structures. (a) A titanium-based hydride complex reacting with N_2 gas, (b) a polynuclear titanium hydride complex and its reaction with N_2 gas, (c) the crystal structure of TiH_2 (light blue spheres represent Ti and large blue spheres represent hydrogen) and (d) structure of $BaTiO_{2.5}H_{0.5}$ shown with products from reactions with D_2 and N_2.

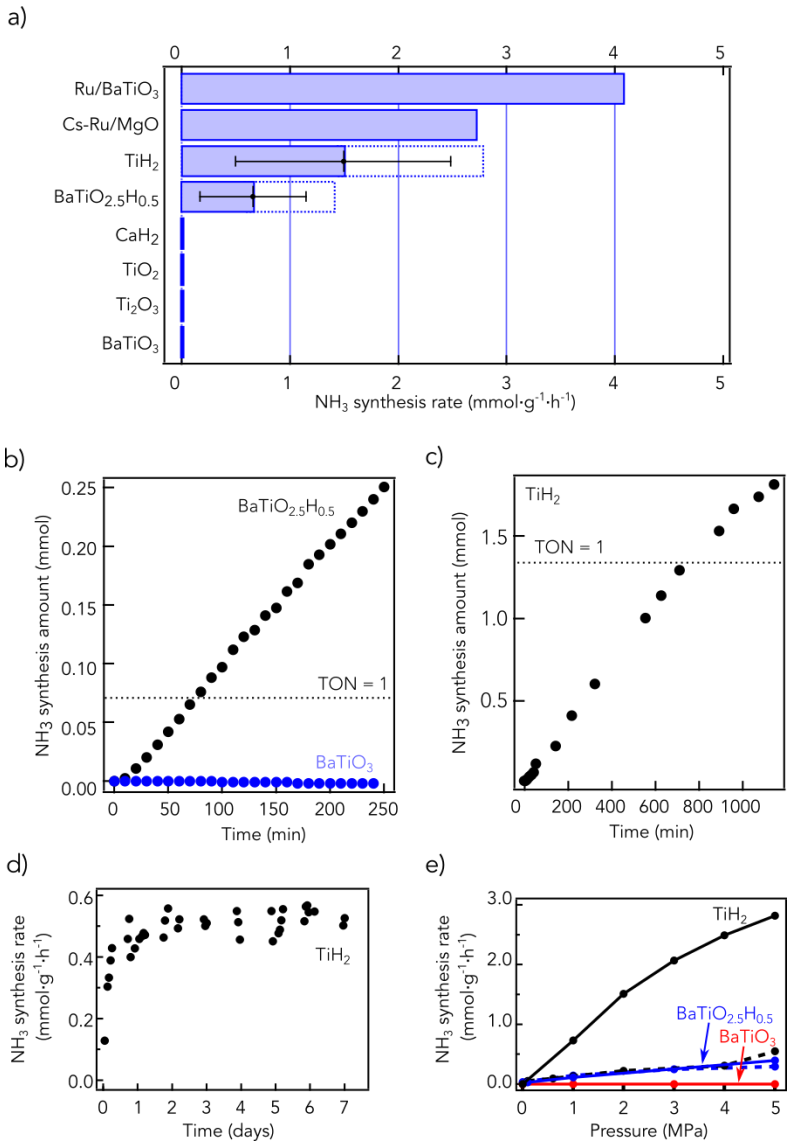

Figure 1.2. Catalytic activities. (a) Catalytic activities of select catalysts for NH_3 synthesis at 400 ˚C, 5 MPa. The full scale (5 mmol g^{-1} h^{-1}) corresponds to an NH_3 concentration of 0.17%. The activities of the $BaTiO_{2.5}H_{0.5}$ and TiH_2 catalysts range by a factor of 1~2 depending on thermal and pressure history of the sample; the error bars represent standard deviations from four separate sample/trials, and the dotted bar indicates the highest activity observed. (b, c) Plots showing time dependence of NH_3 synthesis. (d) A longer experiment showing the stability of TiH_2 activity over 1 week (final TON ~ 6). (e) Pressure dependence (gauge pressure) of activity; the dotted lines indicate a second trial.

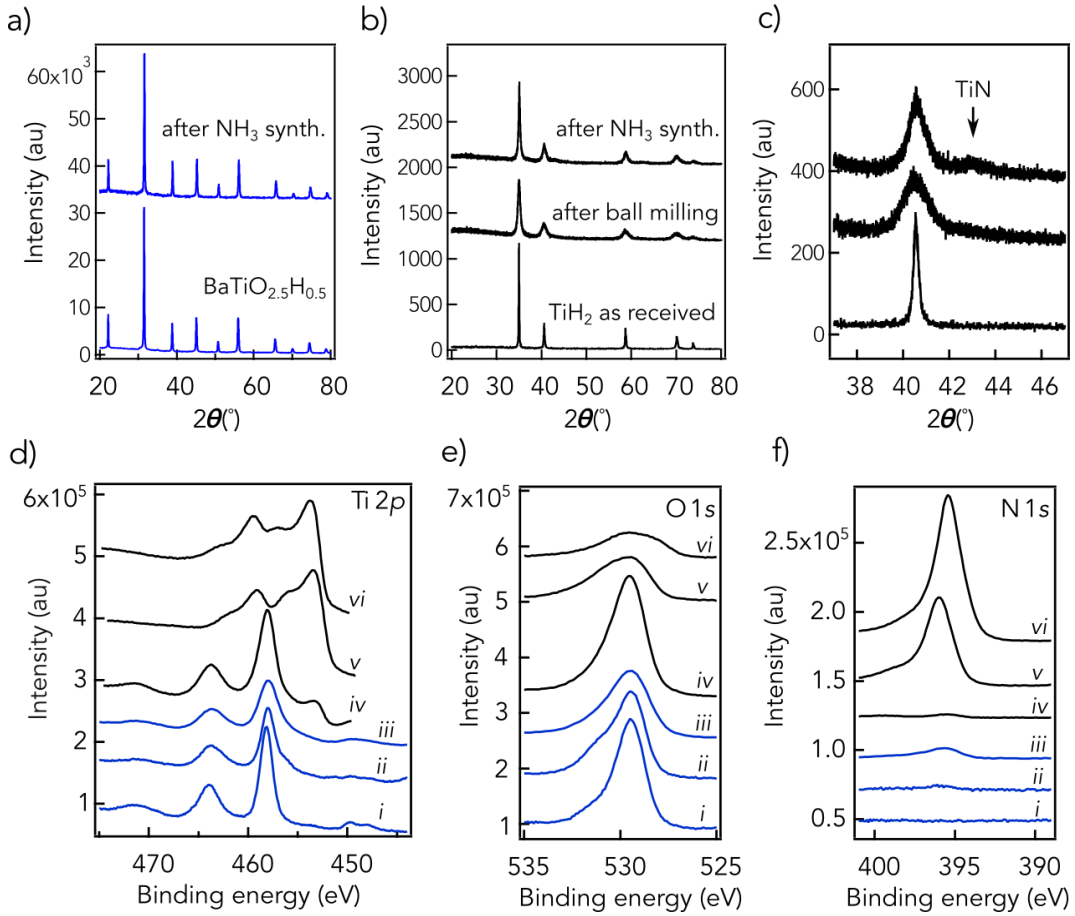

Figure 1.3. Characterization of catalysts. In panel a, XRD shows that the $BaTiO_{2.5}H_{0.5}$ catalyst keeps the same bulk structure during NH_3 synthesis. Panel b shows that the TiH_2 catalyst also shows no change after ball milling or NH_3 synthesis, whereas in panel c a close examination shows possible traces of TiN. The catalyst surface was also examined by XPS, shown in panels d~f. Blue traces denote $BaTiO_{2.5}H_{0.5}$ (or $BaTiO_3$) catalysts: *i, ii, iii* represent spectra of $BaTiO_3$, $BaTiO_{2.5}H_{0.5}$, and the $BaTiO_{2.5}H_{0.5}$ catalyst after NH_3 synthesis, respectively. The black traces, *iv, v*, and vi, are spectra of TiH_2 before ball milling, after ball milling, and after NH_3 synthesis.

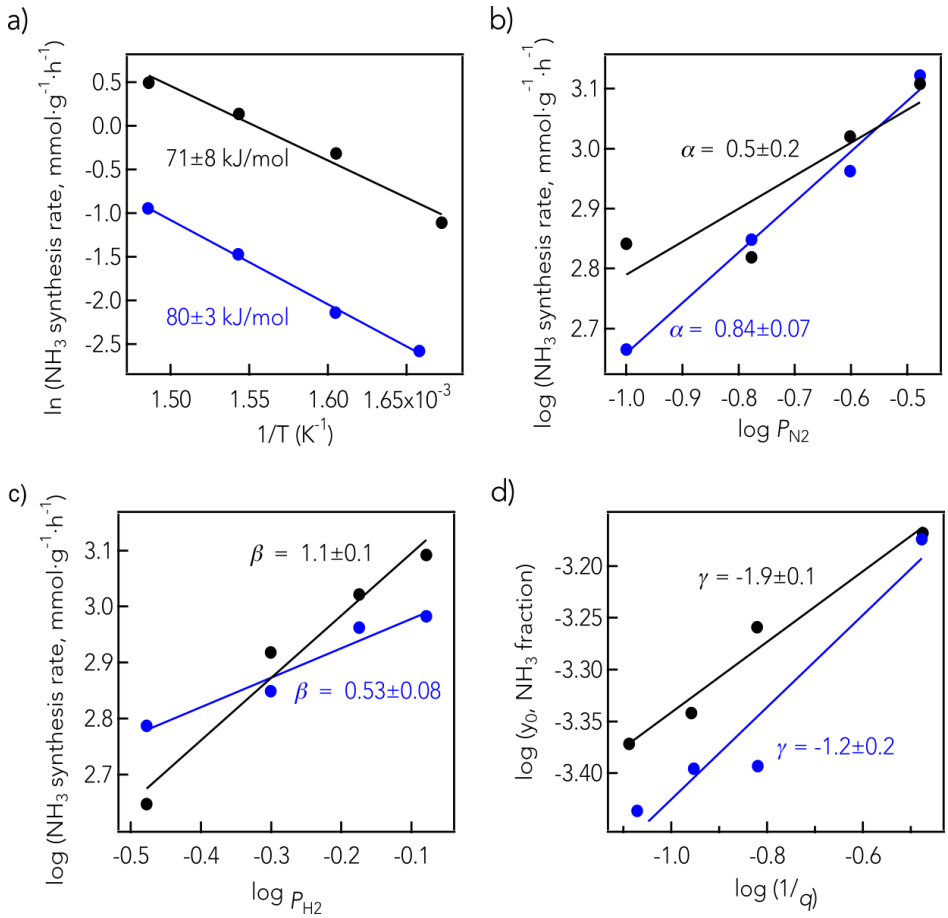

Figure 1.4. Reaction kinetics of $BaTiO_{2.5}H_{0.5}$ (blue) and TiH_2 catalysts (black). Activation energies in panel a are at 5 MPa, and reaction orders (panels b~d) of N_2, H_2, and NH_3 (α, β, and γ respectively) are at 400 ˚C, 5 MPa. For panels b (and c), the H_2 (or N_2) concentration in the feed gas was kept constant, while the N_2 concentration (or H_2) was varied, with Ar also varied as a balance gas. In panel d, q represents the flow rate; this was varied to provide different NH_3 concentrations, and hence the reaction order on NH_3.

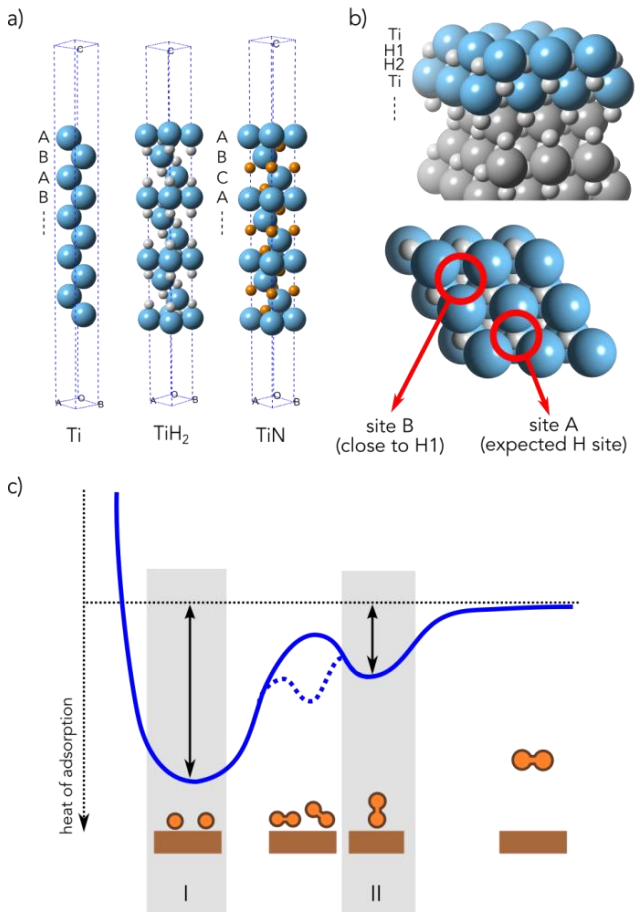

Figure 1.5. Defining model systems to find adsorption energies on close-packed Ti surfaces. (a) Unit cells of slabs used for modeling the Ti 001_{hcp}, TiH_2 111_{fcc}, and TiN 111_{fcc} surfaces. (b) Example of two 3-fold sites on a TiH_2 surface. For details on the possible 3-fold surface sites on Ti/Ru, and TiN, see Figure 1.6. (c) Energetic diagram for N_2 adsorption. 'I' represents dissociative adsorption of N_2, while II represents end-on adsorption of molecular N_2.

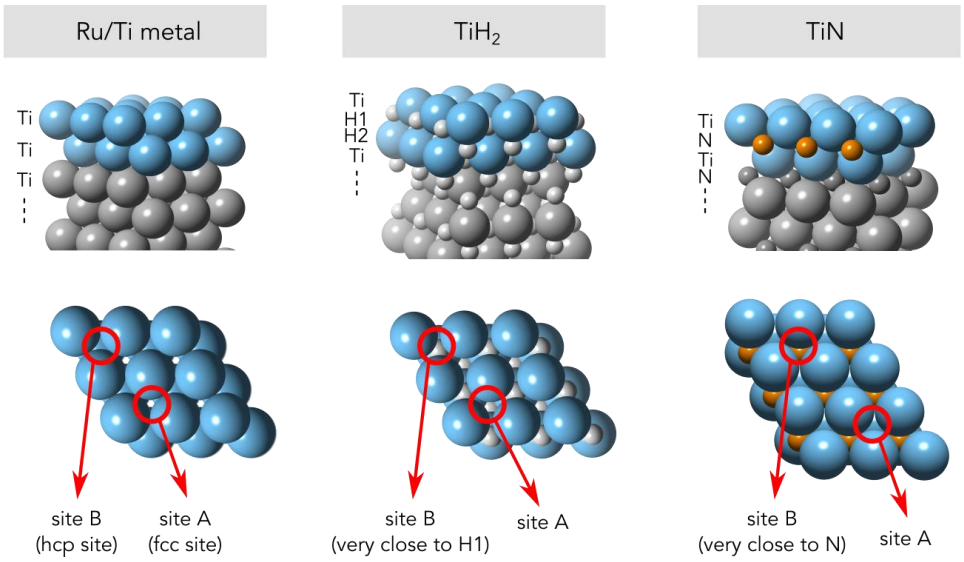

Figure 1.6. Detailed view of close-packed slabs (side and top views) and adsorption sites for calculating heats of adsorption.

Chapter 2. Metal-dependent support effects of oxyhydride-supported Ru, Fe, Co catalysts for ammonia synthesis

2.1. Introduction

Ammonia is one of the most important basic chemicals, and widely employed for the production of fertilizers, plastics, fibers,[1] and more recently, CO_x-free hydrogen.[2] It is predominantly produced by the Haber-Bosch process, typically using oxide-supported iron as the catalyst. Ru-based catalysts on carbon[3] and MgO[4] have also been extensively reported.

Over the most recent past few years, a number of new studies have focused on new catalysts incorporating metal hydride or electride in the support, such as $12CaO{\cdot}7Al_2O_3{:}e^-$ (C12A7:e$^-$),[5, 6] $[Ca_2N]{:}e^-$,[7, 8] CaH_2,[9] Ca_2NH,[10] Y_5Si_3,[11] LaScSi,[12] LiH,[13] and BaH_2,[14] where all of these catalysts show high activities and unusual mechanisms. As a related material, we have recently examined $BaTiO_{2.5}H_{0.5}$ and TiH_2[15] as a catalyst for NH_3 synthesis under Haber-Bosch conditions (400 ˚C, 5 MPa). Titanium, being an early transition metal, was traditionally viewed as an inactive metal for catalytic NH_3 synthesis,[16-19] but we observed a continuous NH_3 formation on $BaTiO_{2.5}H_{0.5}$ and TiH_2 even in the absence of the typically necessary Ru, Fe, or Co particles. Hence, this finding provides one example of a new composition (Ti–H solid system) that may be a starting point for breaking scaling rules.[13, 20]

So far, other than titanium oxyhydride, the recently reported numerous new catalysts for NH_3 synthesis have all involved supported metals such as Ru, Fe, or Co particles. Given the above electride and metal hydride examples, it is reasonable to believe that these new support materials play a key role in the superior performance. It thus naturally raises the question that whether the titanium oxyhydride is a good support material for metal-based catalysts. It is important to note that, these novel supports were either supported with Ru (C12A7:e$^-$), or Fe, Co (LiH, BaH_2), but have never been examined with both metals. The Ru-based catalysts exhibit good activities even under moderate conditions,[21] but the effect on other metals (Fe, Co, Ni, etc.) would be interesting as Wang *et al.* observed with their LiH and BaH_2 support.[13, 14] Hence, comparing the activities of Ru, Fe, and Co supported on $BaTiO_3$ and $BaTiO_{2.5}H_{0.5}$ is a perfect set where the effect of hydride (H^-) can be isolated, and compared with the other novel metal hydride and electride–supported metal catalysts. In this paper, we compare the activities of various catalysts involving $BaTiO_{2.5}H_{0.5}$ (and $BaTiO_3$) as a support, attempt to gain insight into the reaction mechanism based on isotope studies and kinetic experiments.

2.2. Experimental section

2.2.1. *A*TiO$_{3-x}$H$_x$ (*A* = Ca, Sr, Ba) A powder sample of BaTiO$_{3-x}$H$_x$ was synthesized by the CaH$_2$ reduction of BaTiO$_3$ (particle size 100 nm) as reported previously.[1] BaTiO$_3$ (1.62 g) and CaH$_2$ (0.88 g, 99.9%, Aldrich) with a molar ratio of 1:3 were mixed in an N$_2$-filled glovebox, pelletized (2.5 g), and sealed in an evacuated (~10^{-2} Pa) pyrex tube (O.D. 20 mm, I.D. 14 mm, length ca. 12cm). The compositions of BaTiO$_{2.5}$H$_{0.5}$ and BaTiO$_{2.6}$H$_{0.4}$ were obtained by heating the tubes for 1 week at 560 ˚C and 520 ˚C, respectively. After reaction, the blue-black BaTiO$_{3-x}$H$_x$ specimen (ca. 1.5 g) was washed with NH$_4$Cl/methanol (0.1 M, 300 mL), and dried at 100 ˚C under vacuum. The amount of hydride in the sample was verified directly or indirectly by a number of ways, such as TGA (oxidative atmosphere), Rietveld refinement of X-ray data, thermal desorption spectroscopy (TDS), and if available, neutron diffraction. Our previous studies show that all techniques give a consistent formula, and that the amount of anion vacancies is not substantial.[1]

We also prepared the oxyhydrides with *A* = Ca, Sr, Ba, where the starting materials *A*TiO$_3$ were prepared with citric acid method.[2] The powder specimens of citric acid (20.0 g, 98%, Wako) and *A*CO$_3$ (0.025 mol, 99.9%, Aldrich) were dissolved in ethylene glycol (300 mL, 98%, Wako) with titanium isopropoxide (7.5 mL, 97%, Wako) in an N$_2$-filled glovebox and then heated at 300 ˚C till the solution became black. The black powder was then calcinated at 500 ˚C overnight. The oxyhydrides were synthesized by the same method as above with the identical conditions (1 week at 560 ˚C).

2.2.2. BaTiO$_{3-x}$D$_x$ CaD$_2$ was used to prepare BaTiO$_{3-x}$D$_x$ in the same manner as BaTiO$_{3-x}$H$_x$. CaD$_2$ was synthesized by reaction between Ca metal (99.9%, Wako) and D$_2$ gas (99.8%, Taiyo Nippon Sanso). A 3/8" stainless steel tube with a pressure gauge was charged with Ca metal (10.0 g) under N$_2$ atmosphere, and then pressurized with D$_2$ gas (0.2 MPa). The tube was isolated from the D$_2$ source and heated to 600 ˚C (5 ˚C min^{-1}), and a pressure drop was observed within a few minutes. After the pressure decreased to a constant value, D$_2$ was re-introduced (0.2 MPa). This cycle was repeated until no pressure decrease was observed, typically requiring approximately 10 cycles. The reactor was then quenched with water, opened in a glovebox, and the sample was ground, after the above reaction process was repeated another 2 times.

2.2.3. Preparation of Ru, Fe, and Co-based catalysts A Ru$_3$(CO)$_{12}$ (63.3 mg, 99%, Aldrich)/THF solution (300 mL, 3.3×10^{-4} M) was prepared, to which the oxyhydride support (3.0 g) was added. After stirring at room temperature for 4 hours, the solvent was removed *in-vacuo*. The powder (0.3 g) was collected, sealed in a pyrex tube under vacuum (~10^{-2} Pa, O.D. 12 mm, I.D. 10 mm, length ca. 10 cm) and heated in a furnace to 390 ˚C at a rate of 1.7 ˚C min^{-1} for 3 hours. A slight Ru mirror is deposited on the pyrex tube, so elemental analysis was necessary to determine the accurate Ru content. The resulting Ru/BaTiO$_{3-x}$H$_x$ is pyrophoric, and hence is stored in an N$_2$-filled glovebox. After

impregnation and carbonyl decomposition, $BaTiO_{2.5}H_{0.5}$ yielded $Ru/BaTiO_{2.7}H_{0.3}$, while $BaTiO_{2.6}H_{0.4}$ yielded $Ru/BaTiO_{2.85}H_{0.15}$. Here, the hydride contents of the oxyhydride support after metal deposition were determined by Rietveld refinement of synchrotron XRD. For Cs-Ru/MgO, Ru/MgO was impregnated in the similar manner, with an ethanol solution of $CsCO_3$ (molar ratio of Ru:Cs = 1:1). Fe and Co catalysts were prepared by impregnation of the support (3.0 g) with a $Fe(acac)_3$ or $Co(acac)_3$ solution in methanol (189.7 mg of $Fe(acac)_3$ or 181.3 mg of $Co(acac)_3$, 5.37×10^{-4} M, 300 mL), in the same manner as Ru. After solvent removal, the catalyst was directly decomposed to metallic Fe or Co state during an extended H_2 reduction procedure (3 hours) immediately before the NH_3 synthesis experiment.

2.2.4. NH_3 synthesis A 0.1 g sample of catalyst was suspended in a 3/8" stainless steel tube on a bed of quartz wool. The catalyst samples were reduced under flowing pure H_2 (90 mL min^{-1}) at 400 ˚C (6 ˚C min^{-1} heating/cooling) for 2 hours. Catalytic runs were conducted at pressures of 0.1 MPa to 5 MPa (gauge pressure), with a flow rate of 110 mL min^{-1}. The synthesis gas composition was N_2:H_2:Ar = 22.5:67.5:10, unless otherwise noted. NH_3 formation was qualitatively monitored by a Pfeiffer OmniStar mass spectrometer (monitoring NH^{3+} or NH^{2+}), and quantified by an aqueous trap (1.87×10^{-5} M NH_4Cl, 333 mL) and NH_3-selective electrode (Horiba X 5002A).

2.2.5. Kinetic studies All kinetic studies were conducted at conditions where the conversion was at most 1.5% (400 ˚C, 5 MPa). The thermodynamic conversion limit under these conditions is approximately 15%, so our measurements conditions were far from equilibrium. Apparent activation energies were measured at 5 MPa, over temperatures range from 300 to 400 ˚C, with a flow rate of 110 mL min^{-1} in both heating and cooling processes. Initially, gases of commercial supplied purity (O_2 < 2 *ppm*, H_2O < 5 *ppm*) were used. Later, an in-line H_2O/O_2 filter was installed to provide a higher purity (< *ppt*). We found this essential to reduce the hysteresis observed for Ru-based catalysts. For N_2 and H_2 reaction order measurements, gas compositions of N_2:H_2:Ar were 10:50:40, 16.7:50:33.3, 25:50:25 and 33.3:50:16.7 for determining the N_2 order, and 16.7:33.3:50, 16.7:50:33.3, 16.7:66.7:16.7 and 16.7:83.3:0 for determining the H_2 order. All measurements were conducted at 5 MPa, 400 ˚C at a flow rate of 110 mL min^{-1}. Reaction orders of NH_3 were determined by varying the conversion rate, achieved by changing the flow rate of the gas (22.5:67.5:10) between 50 mL min^{-1}, 110 mL min^{-1}, 150 mL min^{-1}, and 200 mL min^{-1}. This data was then analyzed by the method of Aika *et al.* (ref. 33).

2.2.6. N_2 isotopic exchange N_2 isotopic exchange reactions over Cs-Ru/MgO, $Ru/BaTiO_3$, $Ru/BaTiO_{2.5}H_{0.5}$, and $Fe/BaTiO_{2.5}H_{0.5}$ were conducted using a U-shaped glass reactor connected with a closed gas circulation system as reported elsewhere.[3-5] The catalysts (0.25 g) were first loaded into the U-shaped glass reactor in an N_2-filled glovebox. Prior to the exchange reactions, the catalysts were heated in a H_2 atmosphere at 400 ˚C for

2 hours to reduce oxidised metal catalysts. The reaction mixtures ($^{15}N_2$:$^{14}N_2$ = 1:3, total pressure = 15.0 kPa) were then adsorbed on the catalysts without circulation at the conditions of 240–320 ˚C, 0.1 MPa until an adsorption equilibrium was achieved. The reactions (m/e = 28, 29 and 30) were monitored by a Pfeiffer OmniStar mass spectrometer.

2.2.7. Catalyst characterization X-ray diffraction (XRD) patterns were recorded on a Bruker Advance D8 diffractometer in-house, and at beamline BL02B2 at SPring-8 (JASRI, Japan) under beamline proposals 2014A1083, 2014B1104, and 2014B1360. Transmission electron microscope (TEM) images were recorded on Hitachi NAR-9000 (300 kV) or JEM-2010 (200 kV). Pulse CO adsorption was conducted on a BELCAT instrument (Nippon Bel. Co. Ltd.), with a pre-treatment of He (50 ˚C), H_2 (400 ˚C), He (200 ˚C). Combustion elemental analysis for nitrogen was conducted at the School of Pharmacy, Kyoto University. The hydride content was also analyzed by thermal desorption spectroscopy (ESCO. Ltd.). Ru, Fe, and Co contents were analyzed by Sumica Corp; samples were digested by a sodium peroxide fusion, followed by acid extraction and ICP-AES analysis. X-ray absorption spectra (XPS) were obtained at the Ritsumeikan University SR Center, at Beamlines BL-11 and BL-13, and at SPring-8, BL-27SU. XPS data on samples transferred under inert conditions were obtained at the Ritsumeikan University SR Center, using an Ulvac-Phi instrument.

2.3. Results

2.3.1. Ru, Fe, Co/$BaTiO_{3-x}H_x$ We examined the NH_3 synthesis activities of $BaTiO_{3-x}H_x$ after depositing Ru, Fe, and Co at 400 ˚C and 5 MPa, and the results are shown in Figure 2.1a. Ru/$BaTiO_3$, recently reported by Wang *et al.*[22] and Horiuchi *et al.*,[23] is quite a respectable catalyst, slightly surpassing the well-reported Cs-Ru/MgO,[24, 25] one of the most active NH_3 synthesis catalysts. However, Ru/$BaTiO_{2.5}H_{0.5}$ has an activity enhanced by a factor of 7 when compared to Ru/$BaTiO_3$ (28.8 mmol g^{-1} h^{-1} *vs.* 4.1 mmol g^{-1} h^{-1}). The increase in activity correlates with the hydride content, as an intermediate activity was achieved with Ru/$BaTiO_{2.65}H_{0.35}$. This indicates that the presence of hydride within the oxide support drastically enhances the catalytic activity. When the Ru amount increases from 0.86 wt% (nominally 1 wt%) to 2.5 wt% (nominally 3 wt%), the activity increases to 50 mmol g^{-1} h^{-1}. Table 2.1 summarizes the actual loading metal amounts and turn over frequency (TOF) values for these catalysts. For the nominally 1 wt% loaded Ru catalysts, when the support was changed from $BaTiO_3$ to $BaTiO_{2.5}H_{0.5}$, the TOF increased by 9 times, from 0.054 s^{-1} to 0.453 s^{-1}. This compares quite favorably to Cs-Ru/MgO, which has a TOF of 0.032 s^{-1} under the same reaction conditions. Other highly active

Ru-based catalysts involve Ba-Ru/C,[26, 27] and more recently, Ru/C12A7:e⁻,[5, 6] but we have not been able to obtain data with these catalysts.

Fe and Co are metals far less examined currently for NH_3 synthesis,[28] but the enhancement from oxyhydride support is especially prominent here. For Fe, switching the support from oxide to oxyhydride results in an activity enhancement of 70 times (0.2 mmol g^{-1} h^{-1} *vs.* 14 mmol g^{-1} h^{-1}, Figure 2.1a). It is notable that with the use of an oxyhydride support, Fe-based catalysts even surpass pre-existing Ru catalysts. For Co, the activity is increased by a factor of 400 when compared to $Co/BaTiO_3$ (0.014 mmol g^{-1} h^{-1} *vs.* 5.5 mmol g^{-1} h^{-1}). The recent reported active catalysts, transition metals/LiH,[13] show quite high activity at 350 ˚C and 1 MPa (11 mmol g^{-1} h^{-1} for Fe/LiH and 11.5 mmol g^{-1} h^{-1} for Co/LiH). The metal loading amount, however, is nearly 130–135 wt%, making it difficult to compare the support effect with our oxyhydrides. For Fe, XPS and Fe-$L_{3,2}$ edge XAS on the catalysts before/after the reactions show that the supported Fe species during the reaction are not completely an elemental metal (Figure 2.2). This has made it difficult to obtain adequate CO adsorption data (and hence TOF values), but it is curious that the Fe catalyst exhibits such a high activity, despite its seemingly disadvantaged oxidation state.

2.3.2. Ru/(Ca, Sr, Ba)$TiO_{3-x}H_x$ To understand the role of *A*-site alkali-earth cations, NH_3 syntheses of Ru/(Ca, Sr, Ba)$TiO_{3-x}H_x$ (citric acid samples) were examined at 400 ˚C and 5 MPa. The Ru metal particle size and actual deposited amounts on the various supports were also compared (see details in ESI). As shown in Table 2.1, these Ru catalysts (Ru/(Ca, Sr, Ba)TiO_3 and Ru/(Ca, Sr, Ba)$TiO_{3-x}H_x$) show very similar metal size/deposition effects. The (Ca, Sr, Ba)$TiO_{3-x}H_x$ supports exhibit much higher catalytic activity than the corresponding oxide supports (Figure 2.1b). Among these, $Ru/BaTiO_{2.67}H_{0.33}$ showed the highest catalytic performances, both in activity and TOF. In order to make a fair comparison, it is necessary to consider the slightly differing H^- contents in the oxyhydride samples (Table 2.2). However, even though the H^- content of Sr-oxyhydride (x = 0.41) is higher than Ba-oxyhydride (x = 0.33), the NH_3 synthesis activity of $Ru/SrTiO_{2.59}H_{0.41}$ (15 mmol g^{-1} h^{-1}) is much lower than $Ru/BaTiO_{2.67}H_{0.33}$ (30.5 mmol g^{-1} h^{-1}). Thus, the incorporation of hydride has enhanced the activity of all *A*-site substituted catalysts, while preserving the differences in reactivity between the Ca, Sr, and Ba-containing oxide supports. Evidently, the *A*-site still plays an important role.

2.3.3. Pressure effects As shown in Figure 2.3, we also examined the catalytic behavior of $BaTiO_{3-x}H_x$-supported Ru, Fe, and Co catalysts under a range of pressures (0.1–5 MPa). The influence of reaction pressure on the activity is more prominent in $Ru/BaTiO_{2.5}H_{0.5}$ than $Ru/BaTiO_3$; the NH_3 synthesis activities for $Ru/BaTiO_{2.5}H_{0.5}$ increased from 5 mmol g^{-1} h^{-1} at 0.1 MPa to 24.8 mmol g^{-1} h^{-1} at 400 ˚C, 5 MPa. In contrast, for $Ru/BaTiO_3$, the synthesis activities are quite similar between 0.1 MPa and 5

MPa (2.5–3 mmol g^{-1} h^{-1}). For Fe, Co/$BaTiO_{3-x}H_x$, the pressure dependences were much less pronounced than Ru/$BaTiO_{3-x}H_x$ (2.7 mmol g^{-1} h^{-1} at 0.1 MPa and 14 mmol g^{-1} h^{-1} at 5 MPa for Fe, 0.3 mmol g^{-1} h^{-1} at 0.1 MPa and 4 mmol g^{-1} h^{-1} at 5 MPa for Co). Such different catalytic behavior between Ru/$BaTiO_{3-x}H_x$ and Fe, Co/$BaTiO_{3-x}H_x$ under pressures is quite interesting, as it may reflect distinct roles of hydride anions played during the catalytic reactions. Particularly interesting is the case of Ru-based catalysts, where the incorporation of hydride significantly increases the synthesis activity under higher pressure (5 MPa). This behavior is closely related to the elimination of the so-called "hydrogen poisoning effect" on Ru surface with hydride. Hydrogen poisoning effect can be detected by the reaction order on H_2. Hence, in the following, we examine the effect of H^- incorporation in the support on kinetic parameters such as reaction order and activation energy.

2.3.4. Kinetics Comparisons of activation energies (E_a) and reaction orders offer more direct insight into what effect hydride anions and different *A*-site cations provide on the activity. The NH_3 formation rate is determined by the rate constant and the reaction order with respect to N_2 (α), H_2 (β) and NH_3 (γ).[6, 29] Activation energies from our own experiments and some values from the literature are summarized in Table 2.3. The table lists E_a values for both heating and cooling processes when a considerable difference was observed; this hysteresis appears to be dependent on gas purity, so we simply discuss the results using averages. In our experiments at 5 MPa, Fe/$BaTiO_3$ shows an E_a value of 117 kJ mol^{-1}. The inclusion of hydride (Fe/$BaTiO_{2.4}H_{0.6}$) substantially decreases the E_a value by a factor of 2 (64 kJ mol^{-1}). In comparison, the activation energy for unpromoted Fe/C has been reported to be 143 kJ mol^{-1},[28] and for the industrial Fe catalyst KM1R from Halder-Topsøe, E_a ranges from 70 kJ mol^{-1} (1 MPa) to 180 kJ mol^{-1} (100 MPa).[28, 30] For Co/$BaTiO_{2.4}H_{0.6}$, again a low activation energy (69 kJ mol^{-1}) is achieved, as Co/C is reported at 149 kJ mol^{-1} (1 MPa) and a Co spinel catalyst at 270 kJ mol^{-1} (10 MPa).[30] Obviously, the incorporation of hydride has a significant effect for Fe and Co, resulting in activation energies almost on par with Ru/C12A7:e^-,[5, 6] Ru/CaH_2,[9] and transition metals/LiH, BaH_2.[13, 14]

For Ru-based catalysts, the results are more ambiguous given dependencies on gas purity. For a Ru/$BaTiO_3$ sample (commercial $BaTiO_3$ with 100 nm particle size), with typical commercially supplied gases, we obtain E_a of 141 kJ mol^{-1}, but when cooling, a substantially lower E_a (50 kJ mol^{-1}) was observed. Purifying the gas to *ppt* level impurities gave E_a values of 89 kJ mol^{-1} and 103 kJ mol^{-1}, decreasing the hysteresis and increasing the activity. In addition to the commercial $BaTiO_3$ samples, we also examined catalyst samples where the precursor oxides were prepared by the citric acid method (see experimental section), which gave E_a values of 147/159 kJ mol^{-1} (heating/cooling) for Ru/$BaTiO_3$ after purifying the feed gas. For Ru/$BaTiO_{2.7}H_{0.3}$ (the starting $BaTiO_3$ was

prepared by citric acid method), the activation energies are 132 kJ mol^{-1} and 137 kJ mol^{-1} in heating and cooling processes, respectively. Gas purity-dependence of E_a values were also observed in other oxide- (Ru/$CaTiO_3$ and Ru/$SrTiO_3$) and oxyhydride-supported Ru catalysts (Ru/$SrTiO_{2.6}H_{0.4}$ and Ru/$CaTiO_{2.77}H_{0.23}$). It is somewhat surprising that for Ru-based catalysts there is no considerable difference in activation energy due to the presence of hydride.

We now turn to the reaction order. Fe/$BaTiO_3$ and Fe/$BaTiO_{2.5}H_{0.5}$ differ greatly in terms of N_2 reaction order. As shown in Table 2.3, the incorporation of hydride has resulted in lowering α from 1.24 to 0.56, a factor of one half. This is an exceptionally low value, considering that α is typically close to 1. Recent examples of a low α are Ru/C12A7:e^- (α = 0.46) and Fe, Co/LiH (α = 0.37–0.48) where a novel rate-determining step (RDS) has been suggested.[6, 13] We note that Kitano *et al.*[18] have also measured the reaction order for the hydride-incorporated Ru/C12A7:H^-, which is the closest analogy to our oxyhydride catalyst, but obtained a more standard value of 1.

For Ru, the N_2 reaction order remains almost unchanged with the incorporation of hydride into the $BaTiO_3$ support, while the H_2 reaction order β increases from negative to positive. Most Ru catalysts have negative β values, reflecting hydrogen poisoning of the Ru surface. Cs-Ru/MgO has a H_2 reaction order of –1.5, and for Ru/$BaTiO_3$ it is –0.89. For Ru/$BaTiO_{2.5}H_{0.5}$, however, the reaction order is slightly positive, around 0.2. This indicates that with the incorporation of hydride, the Ru catalyst is less susceptible to hydrogen poisoning. This results in a large gain of overall NH_3 yield at elevated pressures, as shown in Figure 2.3. Given the usual correlation between N_2 reaction order α and activation energy E_a, in Ru/$A$$TiO_{3-x}H_x$ (A = Ca, Sr, Ba) we focused on the H_2 reaction order, and this is where we see some differences. For Ru/$BaTiO_{2.7}H_{0.3}$, the H_2 reaction order is slightly positive, around 0.25. The H_2 order of Ru/$SrTiO_{2.6}H_{0.4}$ (–0.36) and Ru/$CaTiO_{2.77}H_{0.23}$ (0.1) are considered to significantly improve hydrogen poisoning when compared to the equivalent oxide supports.

2.3.5. N_2 isotopic exchange The activation energies of N_2 isotopic exchange reaction (IER) over oxide- and oxyhydride-supported Ru, Fe catalysts were examined at 240–320 ˚C and 0.1 MPa. As shown in Figure 2.4, there is no activation energy difference of N_2 IER between Ru/$BaTiO_3$ (72 kJ mol^{-1}) and Cs-Ru/MgO (73 kJ mol^{-1}) under our reaction conditions. This N_2 IER activation energy is determined by the N_2 desorption process (RDS in N_2 IER[31]) and hints that a similar support effect of $BaTiO_3$ and MgO for Ru. Furthermore, the activation energies between NH_3 synthesis and N_2 IER for Ru/$BaTiO_3$ are quite similar (89 kJ mol^{-1} *vs.* 73 kJ mol^{-1}) but for Ru/$BaTiO_{2.5}H_{0.5}$ they are quite different (130 kJ mol^{-1} *vs.* 80 kJ mol^{-1}), indicating a substantial effect from hydride. For Fe/$BaTiO_{2.5}H_{0.5}$, in marked contrast, we observed an approximate value between NH_3 synthesis and N_2 IER (64 kJ mol^{-1} *vs.* 68 kJ mol^{-1}). Moreover, for oxyhydride supports,

there is no significant difference of E_a values between high (5 MPa) and low pressures (0.1 MPa), both for Ru (88 kJ mol^{-1}) and Fe (68 kJ mol^{-1}) (Figure 2.4c). These activation energy values, when viewed from the point of RDS, can be realized from two steps; i.e. N_2 cleavage or NH_n formation[6, 32]. For Ru, combined with similar NH_3 synthesis activation energies between Ru/$BaTiO_3$ and Ru/$BaTiO_{2.5}H_{0.5}$ (80–90 kJ mol^{-1}), we deduced that the RDS is the conventional dissociation process of N_2 (Figures 2.5a). The much higher N_2 IER activation energy (130 kJ mol^{-1}) probably means that the adsorbed N atoms on Ru surface with oxyhydride $BaTiO_{2.5}H_{0.5}$ support is more stable than that with oxide $BaTiO_3$ support (Figure 2.5a). This parallels what Kitano *et al.* claimed for Ru/electride in ref. 6; that the Ru-N energy for electride should be at a lower energy than the conventional oxide supports. However, this cannot be a plausible explanation for high activity of Ru/$BaTiO_{2.5}H_{0.5}$. Kitano *et al.*[6] had summarized the activation energies of N_2 IER on various Ru-based catalysts, showing that the electron back donation from the electride support significantly decreases the N_2 IER activation energy, which seems absent in our Ru/oxyhydride. Since the change of N_2 IER activation energy is not decisive factor for the high activity of Ru/oxyhydride, the elimination of H_2 poisoning, which is manifested by the positive H_2 reaction order, might be more important for Ru.

For Fe, let us first assume that the RDS is the N_2 dissociation process, both for $BaTiO_3$ and $BaTiO_{2.5}H_{0.5}$ support. For Fe/$BaTiO_3$, this energy profile is quite reasonable on the basis of large NH_3 synthesis activation energy (117 kJ mol^{-1}). For Fe/$BaTiO_{2.5}H_{0.5}$, the activation energy of N_2 IER is very close to that of NH_3 synthesis (68 kJ mol^{-1} *vs.* 64 kJ mol^{-1}), meaning that the adsorption energy of nitrogen on Fe is quite small (ca. 4 kJ mol^{-1}). Without support materials, the activation energy for N adsorption on Fe was found to be nearly 260 kJ mol^{-1}.[33] For KM1R, an Fe-based catalyst that were used in the majority of the industrial ammonia synthesis, a value of 146 kJ mol^{-1} was measured for N desorption from Fe surface at 1 MPa.[34] Together with the E_a value (70 kJ mol^{-1}, at 1 MPa) of KM1R[28], we can estimate the adsorption energy of N on Fe is ca. 76 kJ mol^{-1}. Furthermore, similar to the Ru case, we expect the Fe-N energy for $BaTiO_{2.5}H_{0.5}$ should be at a lower energy than that for conventional oxide supports. Obviously, this arrangement does not permit this. Hence, as shown in Figure 2.5b, the RDS for Fe/$BaTiO_{2.5}H_{0.5}$ is altered from N_2 cleavage to the process of NH_n formation if the oxyhydride support functions as a strong electron donor for Fe. As a result, the N adsorption energy on Fe/$BaTiO_{2.5}H_{0.5}$ could be much higher than the first assumption, i.e. 4 kJ mol^{-1}.

2.3.6. H/D isotope studies We have previously shown the labile nature of hydride anion in $BaTiO_{2.5}H_{0.5}$ by its facile exchange with the gas phase.[35, 36] If such hydride exchange of the bulk also occurred during NH_3 synthesis, this would provide a convenient H_2 spillover pathway, which in turn would help explain the lack of H_2 poisoning, as observed in the reaction order of the Ru/$BaTiO_{2.5}H_{0.5}$ catalyst. To gain further insight, we

prepared a deuterated $Ru/BaTiO_{2.4}D_{0.6}$ and examined the H/D isotopic purity of the NH_3 produced when a stream of N_2/H_2 was used. The use of the deuterated support enables us to distinguish the hydrogen source in the product NH_3. Figure 2.6 plots isotope products (NH_3, ND_2H, ND_3) as the catalyst temperature is increased. NH_3 is produced, sequentially in the forms of ND_3 (m/e = 20), ND_2H (m/e = 19) and NH_3 (m/e = 17) (NDH_2 was not monitored since the m/e = 18 signal can come from H_2O and ND^{2+}). The initial deuterated NH_3 signifies that the lattice hydride of the support is involved in the catalytic cycle. After this, NH_3 is continuously produced, meaning that the process is catalytic and ultimately involves the gaseous and lattice hydrogen species. The NH_3 synthesis rate was stable for the entire 3 hours of the experiment, amounting to a turnover number of 50 with respect to the lattice hydrogen, again indicating a catalytic cycle.

We further examined the H/N/O content in the support at various stages, using a combination of combustion elemental analysis (N), synchrotron XRD Rietveld refinement (O+N) and thermal desorption spectroscopy (H). As shown in Table 2.2, for Ru/oxyhydride, depositing the Ru particles requires impregnating with $Ru_3(CO)_{12}$ and then treating under vacuum at 390 ˚C; this process results in some loss of hydride, leading to a composition $Ru/BaTiO_{2.72}H_{0.28}$, which is the catalyst loaded into the reactor. After H_2 treatment (400 ˚C, 0.1 MPa) and NH_3 synthesis, the resulting composition is $Ru/BaTiO_{2.72}N_{0.16}H_{0.12}$. The partial replacement of H^- by N^{3-} is not surprising, based on our previous results showing that $BaTiO_{2.5}H_{0.5}$ converts to an oxynitride form at moderate conditions under N_2[36] or NH_3.[35] As the activity is stable for at least 3 hours (also with 48 hours reactions, Figure 2.7), we expect that the oxyhydride-nitride is the active catalyst composition, and remains constant for the entire duration of the synthesis.

We have also probed the catalytic activity of $Ru/BaTiO_{2.5}N_{0.2}$ (explicitly prepared in the above manner with N_2), but the activity, as shown in Figure 2.1a, is quite low. These results demonstrate that during the reaction, the lattice hydride is indispensable to enhance the catalytic activity. The Fe catalysts show similar H/N compositions, with the catalyst composition changing from $BaTiO_{2.35}H_{0.65}$ to $Fe/BaTiO_{2.72}H_{0.28}$ (after H_2 reduction at 400 °C) and finally $Fe/BaTiO_{2.77}N_{0.12}H_{0.11}$ (after NH_3 synthesis, see Table 2.2). Despite the varied compositions during the actual NH_3 synthesis, unless otherwise stated we refer to all catalysts with their anion compositions prior to metal deposition/NH_3 synthesis.

2.4. Discussion

The results presented above clearly show that incorporating hydride into an oxide support induces various changes in the catalytic activity. In short, when comparing the $BaTiO_3$ and $BaTiO_{3-x}H_x$ supports, we find that: (i) with Ru, the oxyhydride support

suppresses the hydrogen poisoning on the metal surface; (ii) with Fe (or Co), the oxyhydride support significantly decreases the activation energy and N_2 reaction order (α); (iii) the choice of *A*-site in perovskite oxyhydride is another factor for the catalytic performance; (iv) the reversible exchange between lattice hydride and gas-phase H_2 is critical, especially for Ru which is otherwise easily poisoned.

Figure 2.8 summarizes our proposed mechanisms of the effects that hydride bring about. Given the lability of hydride in $BaTiO_{2.5}H_{0.5}$,[35] the oxyhydride support provides a convenient spillover pathway for H^- (and perhaps even N^{3-}) (Figure 2.8a). This is manifested by the positive H_2 reaction order (β) value that we observe with the $Ru/BaTiO_{2.5}H_{0.5}$ catalyst. For conventional oxide-supported Ru catalysts, one main factor limiting the activity is the excessive adsorption of hydrogen at high pressures, which decreases the amount of active sites for NH_3 synthesis, but this effect seems to be mitigated by the colossal H_2 spillover. The N_2 IER on Ru-based catalyst addition supports this effect. The participation of the lattice hydride within the NH_3 synthesis cycle indicates that the hydrogen-based Mars-van Krevelen (MvK) effect previously suggested in $BaTiO_{2.5}H_{0.5}$ and TiH_2[15] is still present even when Ru is added.

The second striking effect is the electron donation from the oxyhydride support (Figure 2.8b), which is observed based on kinetic analysis of Fe, Co/oxyhydride catalysts; that is, the exceptionally low values of activation energy and N_2 reaction order observed with the $BaTiO_{3-x}H_x$ supports. In general, electron donation from the support reduces the strength of the N≡N bond of an adsorbed N_2 molecule, and cleavage of this bond is thought to be the RDS.[37, 38] Hence, low activation energy is one indication of strong electron donation for the oxyhydride support. As for the reaction order of N_2 (α), $Fe/BaTiO_{2.5}H_{0.5}$ showed a roughly one half value compared to conventional heterogeneous catalysts (Table 2.3), indicating a novel RDS is indeed possible.[5, 6] Moreover, the oxyhydride-supported Fe catalysts exhibited higher catalytic activity (70 times with respect to the oxide support) for NH_3 synthesis with a lower activation energy. Taking into consideration the corresponding N_2 IER results, we conclude that adsorbed N_2 molecules dissociate more smoothly on the Fe surface by electron donation from the oxyhydride support, while the subsequent steps can be the RDS for the surface reactions of dissociated N and H atoms (Figure 2.3b).

The role of hydride has been discussed in many catalytic supports recently, but hydride appears to have somewhat different roles depending on the material supported. For the $Ru/C12A7:e^-$ and $Ru/Ca_2N:e^-$, a small amount of hydride is introduced into the support during the reaction; this is a sign of spillover which in turn leads to no H_2 poisoning on the surface.[5, 6, 9, 39] However, H_2 poisoning is observed on the pure hydride catalyst $Ru/C12A7:H^-$,[6] so there are some subtleties here. For the Ru/CaH_2 and Ru/Ca_2NH,[9] Kitano *et al.* proposed that an *in-situ* partial conversion of hydride into

electride (i.e. Ru/$CaH_{2-x}(e^-)_x$), and the electride's strong electron donation, not hydride's, is the main factor for increasing activity. We should note that these materials have only been tested with Ru so far.

Regarding the effects of LiH and BaH_2, Wang *et al.*[13] and Gao *et al.*[14] addressed different aspects. On the basis of the results of a wide range of supported metals (V, Cr, Mn, Fe, Co, Ni), the authors proposed that the transition metal-adsorbed nitrogen species is readily transferred to the LiH surface and then hydrogenated into a [LiNH] species. This leads to low α and high activity on a wide range of metals which would otherwise may have unfavorable metal-nitride bond strengths.[17] Interestingly, an alternate explanation similar to Ru/electride can be applied to this material too. This would involve partial conversion of LiH to an electride, leading to reduced activation energies, and low N_2 reaction order due to an alternate RDS. As yet, there is no cross-confirmation between the various proposed mechanisms and new support materials.

In the case of our oxyhydride supports, we see a combination (but not all) of these effects, depending on the metal supported. For Ru/oxyhydride, unlike Ru/CaH_2, we do not see any evidence of hydride conversion to electride, since we do not see any substantially reduced activation energies or N_2 reaction order. However, we find increased activity due to elimination of H_2 poisoning, as shown by the positive H_2 reaction order and isotope study. Furthermore, our oxyhydride supports are still effective for Ru at low temperatures (Figure 2.4b), this is extremely different from Ru/C12A7:e^-,[6] where the reaction mechanism was controlled by the temperatures. Combined, for Ru, oxyhydride is only to suppress the H_2 poisoning on the metal surface. Fe and Co, which typically give lower activities than Ru, benefit from the presence of hydride the most in our study; this is similar to the study by Wang *et al.*,[13] where the activity of Co increases by three orders of magnitude. The N_2 reaction orders and activation energies also decrease significantly in their study, analogous to our own results for Fe and Co. However, with N_2 IER experiments, we observed an evidence for altered RDS on Fe/oxyhydride. Hence, unlike Ru, the oxyhydride supports function as an electron donor for Fe (and possibly Co).

2.5. Conclusions

The introduction of hydride into the oxide $A$$TiO_3$ (A = Ca, Sr, Ba) support results in enhanced activities and altered kinetic parameters, with the details depending on the choice of supported metals (Ru, Fe, Co). Overall, the high activity is due to a hydrogen-based Mars–van Krevelen mechanism decreasing the hydrogen poisoning, and also as hydride functioning either as a strong electron donor. Which of these effects visibly dominates depends on the metal supported.

Comparison with other hydride-based catalysts reveals that hydride can have a variety of roles, depending on the support matrix. In terms of optimization, the titanium oxyhydrides are based on well-known oxide perovskites, and have a potential to have their composition tuned in *A*-site or *B*-site substitution to search a further active ammonia synthesis catalyst. As the number of oxyhydrides increases,[40-43] our study shows that the interesting effects of hydrogen can be investigated in a wider range of materials than previously thought.

References

1. Appl, M., *Ammonia: principles and industrial practice*; Wiley Online Library, **1999**.
2. Klerke, A.; Christensen, C. H.; Nørskov, J. K.; Vegge, T., *J. Mater. Chem.* **2008**, *18*, 2304.
3. Aika, K.-i.; Kawahara, T.; Murata, S.; Onishi, T., *Bull. Chem. Soc. Jpn.* **1990**, *63*, 1221.
4. Murata, S.; Aika, K.-I., *Appl. Catal. A: Gen.* **1992**, *82*, 1.
5. Kitano, M.; Inoue, Y.; Yamazaki, Y.; Hayashi, F.; Kanbara, S.; Matsuishi, S.; Yokoyama, T.; Kim, S. W.; Hara, M.; Hosono, H., *Nat. Chem.* **2012**, *4*, 934.
6. Kitano, M.; Kanbara, S.; Inoue, Y.; Kuganathan, N.; Sushko, P. V.; Yokoyama, T.; Hara, M.; Hosono, H., *Nat. Commun.* **2015**, *6*, 6731.
7. Kim, Y. J.; Kim, S. M.; Cho, E. J.; Hosono, H.; Yang, J. W.; Kim, S. W., *Chem. Sci.* **2015**, *6*, 3577.
8. Kim, Y. J.; Kim, S. M.; Hosono, H.; Yang, J. W.; Kim, S. W., *Chem. Comm.* **2014**, *50*, 4791.
9. Kitano, M.; Inoue, Y.; Ishikawa, H.; Yamagata, K.; Nakao, T.; Tada, T.; Matsuishi, S.; Yokoyama, T.; Hara, M.; Hosono, H., *Chem. Sci.* **2016**, *7*, 4036.
10. Abe, H.; Niwa, Y.; Kitano, M.; Inoue, Y.; Sasase, M.; Nakao, T.; Tada, T.; Yokoyama, T.; Hara, M.; Hosono, H., *J. Phys. Chem. C* **2017**, *121*, 20900.
11. Lu, Y.; Li, J.; Tada, T.; Toda, Y.; Ueda, S.; Yokoyama, T.; Kitano, M.; Hosono, H., *J. Am. Chem. Soc.* **2016**, *138*, 3970.
12. Wu, J.; Gong, Y.; Inoshita, T.; Fredrickson, D. C.; Wang, J.; Lu, Y.; Kitano, M.; Hosono, H., *Adv. Mater.* **2017**, 1700924.
13. Wang, P.; Chang, F.; Gao, W.; Guo, J.; Wu, G.; He, T.; Chen, P., *Nat. Chem.* **2017**, *9*, 64.
14. Gao, W.; Wang, P.; Guo, J.; Chang, F.; He, T.; Wang, Q.; Wu, G.; Chen, P., *ACS Catal.* **2017**, *7*, 3654.
15. Kobayashi, Y.; Tang, Y.; Kageyama, T.; Yamashita, H.; Masuda, N.; Hosokawa, S.; Kageyama, H., *J. Am. Chem. Soc.* **2017**, *139*, 18240.
16. Jens, K.; Studt, F.; Abild-Pedersen, F.; Bligaard, T., *Fundamental concepts in heterogeneous catalysis*; John Wiley & Sons, **2014**.
17. Vojvodic, A.; Medford, A. J.; Studt, F.; Abild-Pedersen, F.; Khan, T. S.; Bligaard, T.; Nørskov, J. K., *Chem. Phys. Lett.* **2014**, *598*, 108.
18. Jones, G.; Bligaard, T.; Abild-Pedersen, F.; Nørskov, J. K., *J. Phys.: Condens. Mater* **2008**, *20*, 064239.
19. Calle-Vallejo, F.; Loffreda, D.; KoperMarc, T. M.; Sautet, P., *Nat. Chem.* **2015**, *7*, 403.
20. Dahl, S.; Logadottir, A.; Jacobsen, C. J. H.; Nørskov, J. K., *Appl. Catal. A: Gen.* **2001**, *222*, 19.
21. Bielawa, H.; Hinrichsen, O.; Birkner, A.; Muhler, M., *Angew. Chem. Int. Edit.* **2001**, *40*, 1061.
22. Kobayashi Y.; Hernandez O. J.; Sakaguchi T.; Yajima T.; Roisnel T.; Tsujimoto Y.; Morita M.; Noda Y.; Mogami Y.; Kitada A.; Ohkura M.; Hosokawa S.; Li Z.; Hayashi K.; Kusano Y.;

Kim J.; Tsuji N.; Fujiwara A.; Matsushita Y.; Yoshimura K.; Takegoshi K.; Inoue M.; Takano M.; Kageyama H., *Nat. Mater.* **2012**, *11*, 507–511.
23. M. Kakihana, T. Okubo, M. Arima, Y. Nakamura, M. Yashima and M. Yoshimura, *J. Sol-Gel Sci. Techn.* **1998**, *12*, 95–109.
24. O. Hinrichsen, F. Rosowski, A. Hornung, M. Muhler and G. Ertl, *J. Catal.* **1997**, *165*, 33–44.
25. K. Urabe, K.-i. Aika and A. Ozaki, *J. Catal.* **1975**, *38*, 430–434.
26. Wang, Z.; Lin, J.; Wang, R.; Wei, K., *Catal. Commun.* **2013**, *32*, 11.
27. Horiuchi, Y.; Kamei, G.; Saito, M.; Matsuoka, M., *Chem. Lett.* **2013**, *42*, 1282.
28. Ozaki, A. *Acc. Chem. Res.* **1981**, *14*, 16.
29. Rosowski, F.; Hornung, A.; Hinrichsen, O.; Herein, D.; Muhler, M.; Ertl, G., *Appl. Catal. A: Gen.* **1997**, *151*, 443.
30. Rarogpilecka, W.; Miskiewicz, E.; Szmigiel, D.; Kowalczyk, Z., *J. Catal.* **2005**, *231*, 11.
31. Raróg, W.; Kowalczyk, Z.; Sentek, J.; Składanowski, D.; Zieliński, J., *Catal. Lett.* **2000**, *68*, 163.
32. Hagen, S.; Barfod, R.; Fehrmann, R.; Jacobsen, C. J. H.; Teunissen, H. T.; Chorkendorff, I., *J. Catal.* **2003**, *214*, 327.
33. Aika, K.; Kumasaka, M.; Oma, T.; Kato, O.; Matsuda, H.; Watanabe, N.; Yamazaki, K.; Ozaki, A.; Onishi, T., *Appl. Catal.* **1986**, *28*, 57.
34. Lendzion-Bieluń, Z.; Pelka, R.; Arabczyk, W., *Catal. Lett.* **2009**, *129*, 119.
35. Dahl, S.; Törnqvist, E.; Chorkendorff, I., *J. Catal.* **2000**, *192*, 381.
36. J. R. Jennings, *Catalytic ammonia synthesis: fundamentals and practice*, Springer Science & Business Media, **2013**.
37. M. Muhler, F. Rosowski and G. Ertl, *Catal. Lett.* **1994**, *24*, 317–331.
38. Haruyama, T.; Namise, T.; Shimoshimizu, N.; Uemura, S.; Takatsuji, Y.; Hino, M.; Yamasaki, R.; Kamachi, T.; Kohno, M., *Green Chem.* **2016**, *18*, 4536.
39. Yajima, T.; Takeiri, F.; Aidzu, K.; Akamatsu, H.; Fujita, K.; Yoshimune, W.; Ohkura, M.; Lei, S.; Gopalan, V.; Tanaka, K.; Brown, C. M.; Green, M. A.; Yamamoto, T.; Kobayashi, Y.; Kageyama, H., *Nat. Chem.* **2015**, 7, 1017.
40. Masuda, N.; Kobayashi, Y.; Hernandez, O.; Bataille, T.; Paofai, S.; Suzuki, H.; Ritter, C.; Ichijo, N.; Noda, Y.; Takegoshi, K.; Tassel, C.; Yamamoto, T.; Kageyama, H., *J. Am. Chem. Soc.* **2015**, *137*, 15315.
41. Hellman, A.; Baerends, E. J.; Biczysko, M.; Bligaard, T.; Christensen, C. H.; Clary, D. C.; Dahl, S.; van Harrevelt, R.; Honkala, K.; Jonsson, H.; Kroes, G. J.; Luppi, M.; Manthe, U.; Nørskov, J. K.; Olsen, R. A.; Rossmeisl, J.; Skúlason, E.; Tautermann, C. S.; Varandas, A. J. C.; Vincent, J. K., *J. Phys. Chem. B* **2006**, *110*, 17719.
42. Liu, H., *Chin. J. Catal.* **2014**, *35*, 1619.
43. Kanbara, S.; Kitano, M.; Inoue, Y.; Yokoyama, T.; Hara, M.; Hosono, H., *J. Am. Chem. Soc.*

2015, *137*, 14517.
44. Denis Romero,F.;Leach, A.; Möller, J. S.; Foronda, F.; Blundell, S. J.; Hayward, M. A., *Angew. Chem. Int. Edit.* **2014**, *126*, 7686.
45. Hayward, M. A.; Cussen, E. J.; Claridge, J. B.; Bieringer, M.; Rosseinsky, M. J.; Kiely, C. J.; Blundell, S. J.; Marshall, I. M.; Pratt, F. L., *Science* **2002**, *295*, 1882.
46. Bang, J.; Matsuishi, S.; Hiraka, H.; Fujisaki, F.; Otomo, T.; Maki, S.; Yamaura, J.; Kumai, R.; Murakami, Y.; Hosono, H., *J. Am. Chem. Soc.* **2014**, *136*, 7221.
47. Tassel, C.; Goto, Y.; Kuno, Y.; Hester, J.; Green, M.; Kobayashi, Y.; Kageyama, H., *Angew. Chem. Int. Edit.* **2014**, *53*, 10377.

Table 2.1. Comparison of activities, particle sizes, and turn over frequency (TOF) values. TOF values based on sites available as measured by CO-pulse adsorption. The Ru particle sizes on the oxide and oxyhydride supports are very close, all within the range of 3–5 nm. This indicates these prepared catalysts should show very similar metal size/deposition effects.

Catalysts	Ru wt%		Dispersion[b] %	Size[c] nm	Rate[d] mmol g^{-1} h^{-1}	TOF[e] s^{-1}
	Nominal	Actual[a]				
$Ru/BaTiO_3$	1	0.89	23.8	5.6	4.1	0.054
	3	2.6	20.8	6.4	9.41	0.049
	5	4.1	15.5	8.6	29.5	0.130
$Ru/BaTiO_{2.51}H_{0.49}$	1	0.86	20.8	6.4	28.8	0.453
	3	2.5	10.3	12.9	50	0.543
	5	4.3	11.6	11.5	20.7	0.116
$Fe/BaTiO_3$	1	0.39	–	~5	0.2	–
$Fe/BaTiO_{2.35}H_{0.65}$	1	0.40	15.7	7.4	14	0.345
$Co/BaTiO_3$	1	0.26	–	~5	0.014	–
$Co/BaTiO_{2.37}H_{0.63}$	1	0.31	66.3	~5	5.5	0.044
Cs-Ru/MgO	1	0.85	28.2	4.7	2.74	0.032
$Ru/BaTiO_3$	1	0.76	34.4	3.9	2.12	0.022

$Ru/BaTiO_{2.7}H_{0.3}$	1	0.81	52. 5	2.6	30.36	0.2
$Ru/SrTiO_3$	1	0.66	52.2	2.6	2.03	0.017
$Ru/SrTiO_{2.6}H_{0.4}$	1	0.75	39.8	3.4	15.74	0.148
$Ru/CaTiO_3$	1	0.73	38.9	3.5	0.77	0.008
$Ru/CaTiO_{2.77}H_{0.23}$	1	0.71	26.2	5.1	5.37	0.082

[a] as measured by ICP-AES after alkali-fusion/acid digestion; [b,c] particle size and dispersion were calculated on the basis of CO-pulse results; [d] rate denotes ammonia synthesis rates; [e] TOF was calculated by synthesis rates divided by the number of Ru atoms deposited on the catalysts.

Table 2.2. Details of anionic compositions and lattice parameters of oxyhydride supports. Chemical formulae and lattice parameters are based on Rietveld refinement of synchrotron XRD, while the nitrogen content was independently measured by combustion analysis. H contents are inferred by assuming no vacancies.

Catalyst	Support composition	After metal deposition	After H_2 reduction (before NH_3 synthesis)	After NH_3 synthesis
$Ru/BaTiO_{2.5}H_{0.5}$	$BaTiO_{2.51(1)}H_{0.49(1)}$ a = 4.02995(4) Å	$Ru/BaTiO_{2.72(1)}H_{0.28(1)}$ a = 4.01145(4) Å		$Ru/BaTi(O,N)_{2.88(1)}H_{0.12(1)}$ a = 4.0099(3) Å c = 4.0098(6) Å (N 0.90 wt%)
$Ru/BaTiO_{2.65}H_{0.35}$	$BaTiO_{2.65(1)}H_{0.35(1)}$ a = 4.0243(1) Å	$Ru/BaTiO_{2.85(1)}H_{0.15(1)}$ a = 4.00428(6) Å c = 4.0106(1) Å		$Ru/BaTi(O,N)_{2.98(1)}H_{0.02(1)}$ a =4.00446(5) Å c = 4.01218(7) Å (N 0.61 wt%)
$Fe/BaTiO_{2.4}H_{0.6}$	$BaTiO_{2.35(2)}H_{0.65(2)}$ a = 4.03370(2) Å		$Fe/BaTiO_{2.72(2)}H_{0.28(2)}$ a =4.02319(4) Å	$Fe/BaTi(O,N)_{2.89}H_{0.11}$ a =4.01348(4) Å (N 0.72 wt%)
$Co/BaTiO_{2.4}H_{0.6}$	$Co/BaTiO_{2.37(2)}H_{0.63(2)}$ a = 4.030(1) Å			$Co/BaTi(O,N)_{2.87(2)}H_{0.13(2)}$ a = 4.01288(4) Å (N 0.69 wt%)
$Ru/BaTiO_{2.7}H_{0.3}$	$BaTiO_{2.50(1)}H_{0.50(1)}$	$Ru/BaTiO_{2.67}H_{0.33}$		$Ru/BaTi(O,N)_{2.88(4)}H_{0.12(4)}$
$Ru/SrTiO_{2.6}H_{0.4}$	$SrTiO_{2.62(2)}H_{0.38(2)}$	$Ru/SrTiO_{2.59}H_{0.41}$		$Ru/SrTi(O,N)_{2.69(2)}H_{0.31(2)}$
$Ru/CaTiO_{2.77}H_{0.23}$	$CaTiO_{2.72(2)}H_{0.28(2)}$	$Ru/CaTiO_{2.77}H_{0.23}$		$Ru/CaTi(O,N)_{2.86(2)}H_{0.14(2)}$

Table 2.3. Comparison of activation energies and reaction orders.

Catalysts	E_a, kJ mol^{-1}	N_2 order, α	H_2 order, β	NH_3 order, γ
$Fe/BaTiO_3$	131/103	1.24(±0.09)	0.93(±0.05)	–0.52(±0.09)
$Fe/BaTiO_{2.4}H_{0.6}$	72/54	0.5(±0.1)	0.7(±0.1)	–1.1(±0.2)
Fe/C [a]	143	0.9	1.5	–1
KM1R [b]	70	0.9	2.2	–1.5
Co/C [c]	149	0.8	–0.4	–0.3
$Ru/BaTiO_3$	89/103	1.2(±0.2)	–0.89(±0.02)	–0.19(±0.05)
$Ru/BaTiO_{2.5}H_{0.5}$ [d]	83	0.7(±0.08)	0.2(±0.1)	–0.64(±0.04)
$Ru/BaTiO_3$	153	–	–0.56	–
$Ru/BaTiO_{2.7}H_{0.3}$ [e]	135	–	0.25	–
$Ru/SrTiO_3$	91	–	–0.98	–
$Ru/SrTiO_{2.6}H_{0.4}$ [e]	94	–	–0.36	–
$Ru/CaTiO_3$	68	–	–0.26	–
$Ru/CaTiO_{2.77}H_{0.23}$ [e]	71.6	–	0.1	–
Cs-Ru/MgO [f]	109	0.8	–0.9	0
Cs-Ru/MgO	–	1.14(±0.08)	–1.5(±0.2)	–1(±0.2)
Ru/C12A7:e^- [g]	49	0.46	0.96	–1
Ru/C12A7:O^{2-} [h]	105	1	–	–
Ru/C12A7:H^- [i]	–	1	0.63	0.6

[a, b, c] 1 MPa, 320–400 °C, from ref. 32; [f] 2 MPa, 277–357 °C, ref. 28; [g, h, i] 0.1 MPa, 320–400 °C, ref. 5, 6; [h, i] ref. 5; [g] ref. 6; [d] commercial 100 nm $BaTiO_3$; [e] starting materials $ATiO_3$ (A = Ca, Sr, Ba) were prepared by citric acid method.

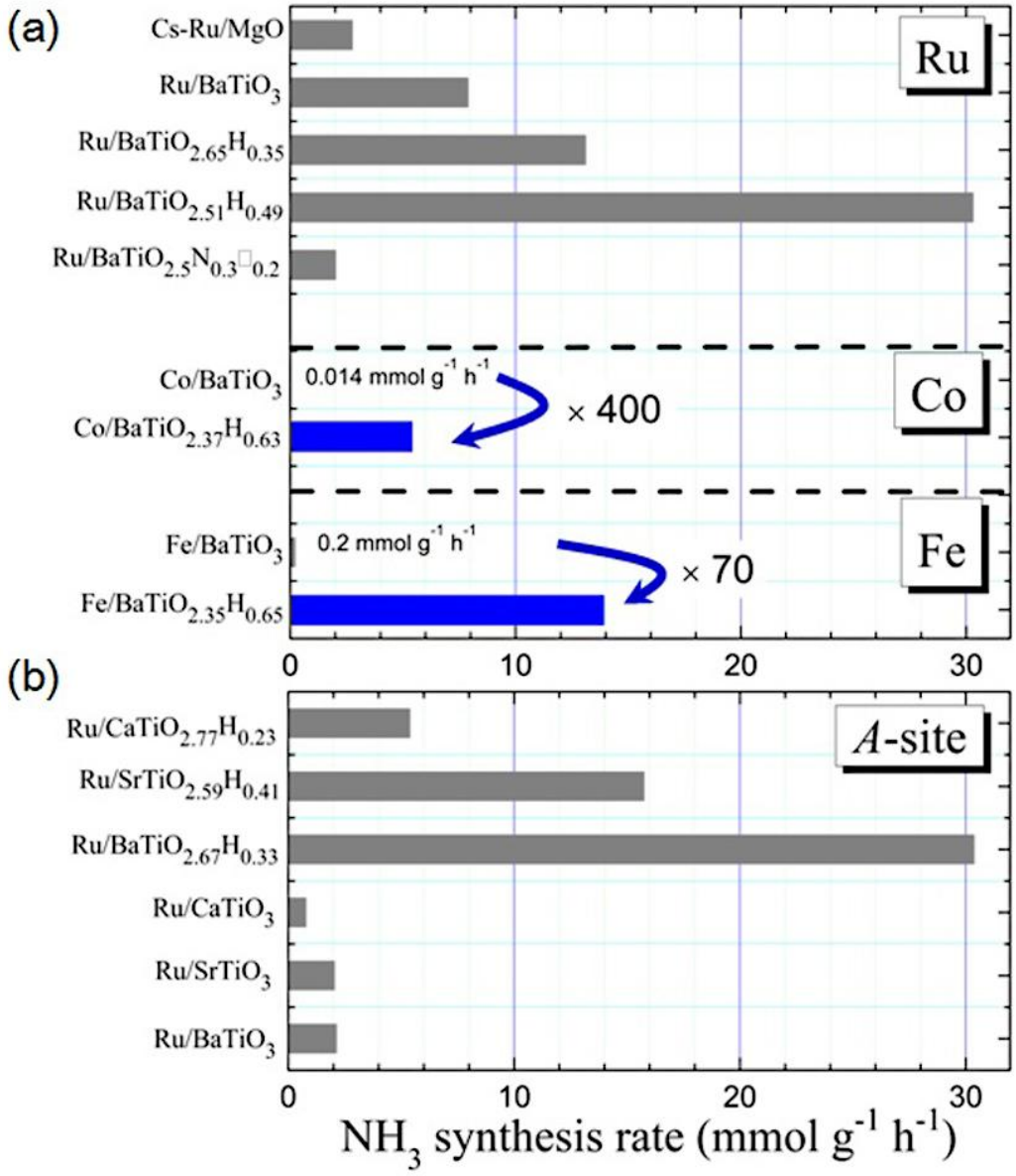

Figure 2.1. Activities of various supported-metal catalysts. Nominally 1 wt% metal loading amount, see Table 2.1 for the actual amounts. Anionic compositions during synthesis conditions are given in the Table 2.2.

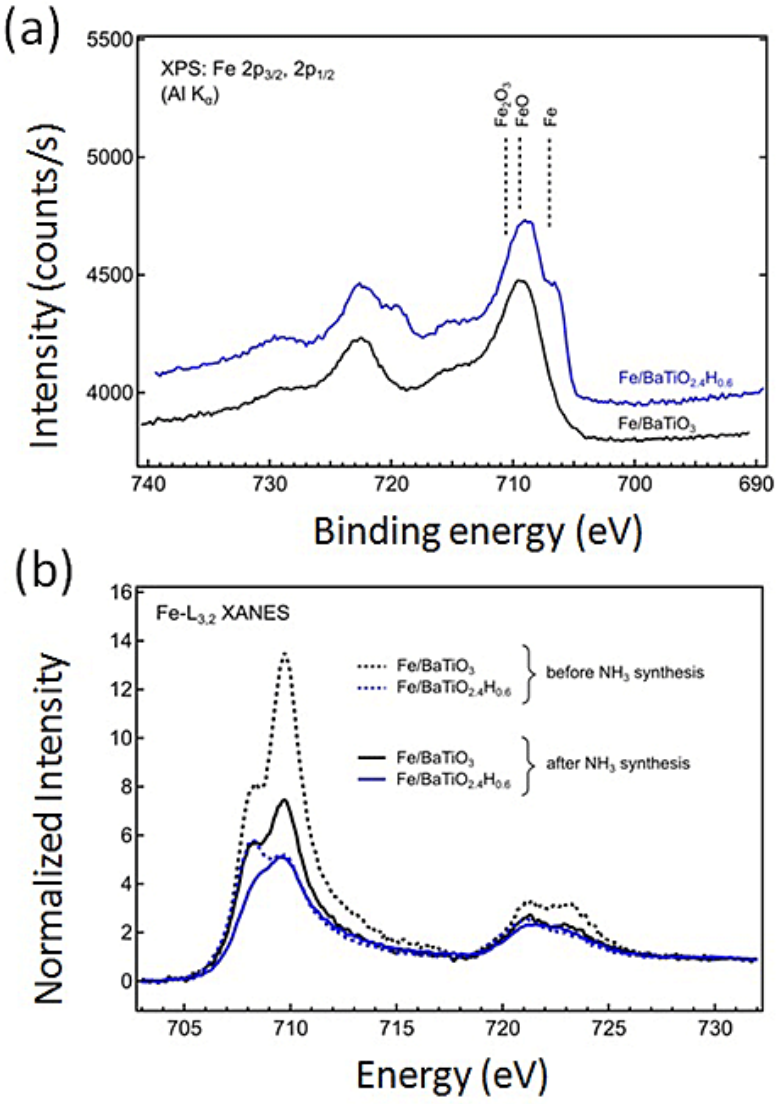

Figure 2.2. XPS and XAS spectra of Fe catalysts. Panel a compares the XPS spectra of $Fe/BaTiO_3$ and $Fe/BaTiO_{2.45}H_{0.65}$ before H_2 reduction, prior to NH_3 synthesis. The dotted lines for Fe, FeO, and Fe_2O_3 are representative positions from the NIST XPS database. Panel b shows the Fe-$L_{3,2}$ X-ray absorption spectra for the Fe catalysts before and after NH_3 synthesis. The split L_3 peak at 708–710 eV indirectly reflects the oxidation state. While the split peak intensities ideally represent the t_{2g} and e_g orbital populations, empirically they correlate with Fe^{2+} and Fe^{3+} states; Fe^{2+} compounds have a intense peak at 708 eV, while for Fe^{3+} compounds the peak component at 710 eV is stronger. The data show that during/after NH_3 synthesis, both the oxide- and oxyhydride-supported catalysts have relatively similar oxidation states.

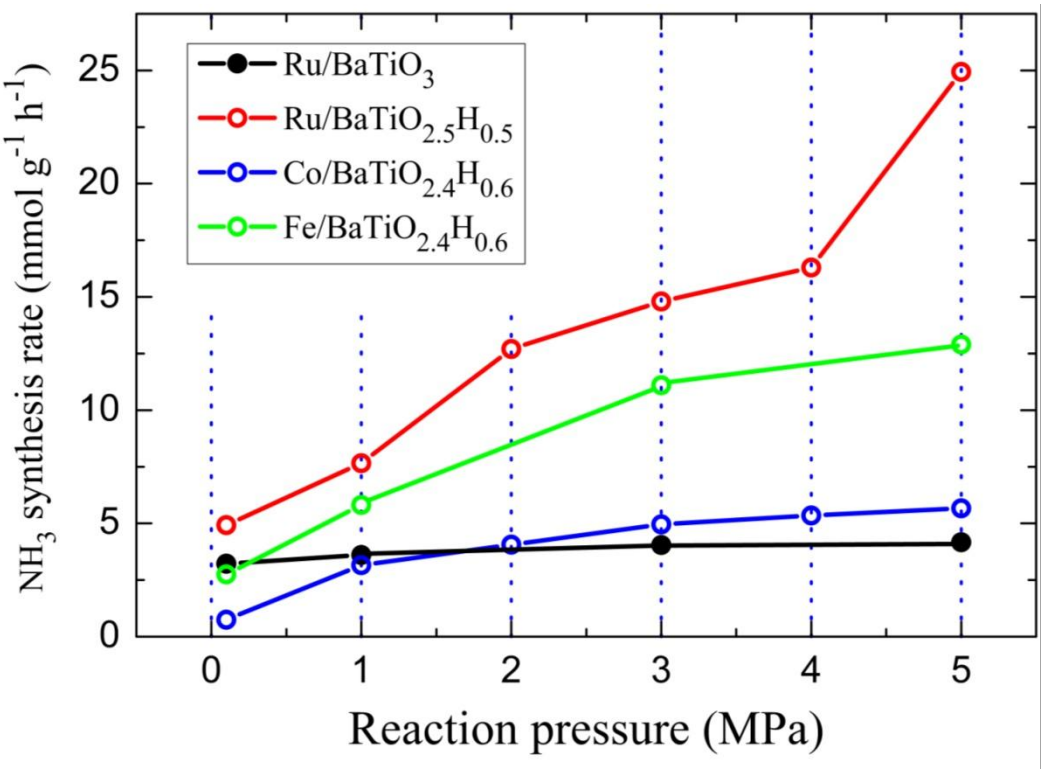

Figure 2.3. NH_3 synthesis activities of Ru, Fe, Co/$BaTiO_{3-x}H_x$ at 400 ˚C reactions over a range of pressures (0.1–5 MPa).

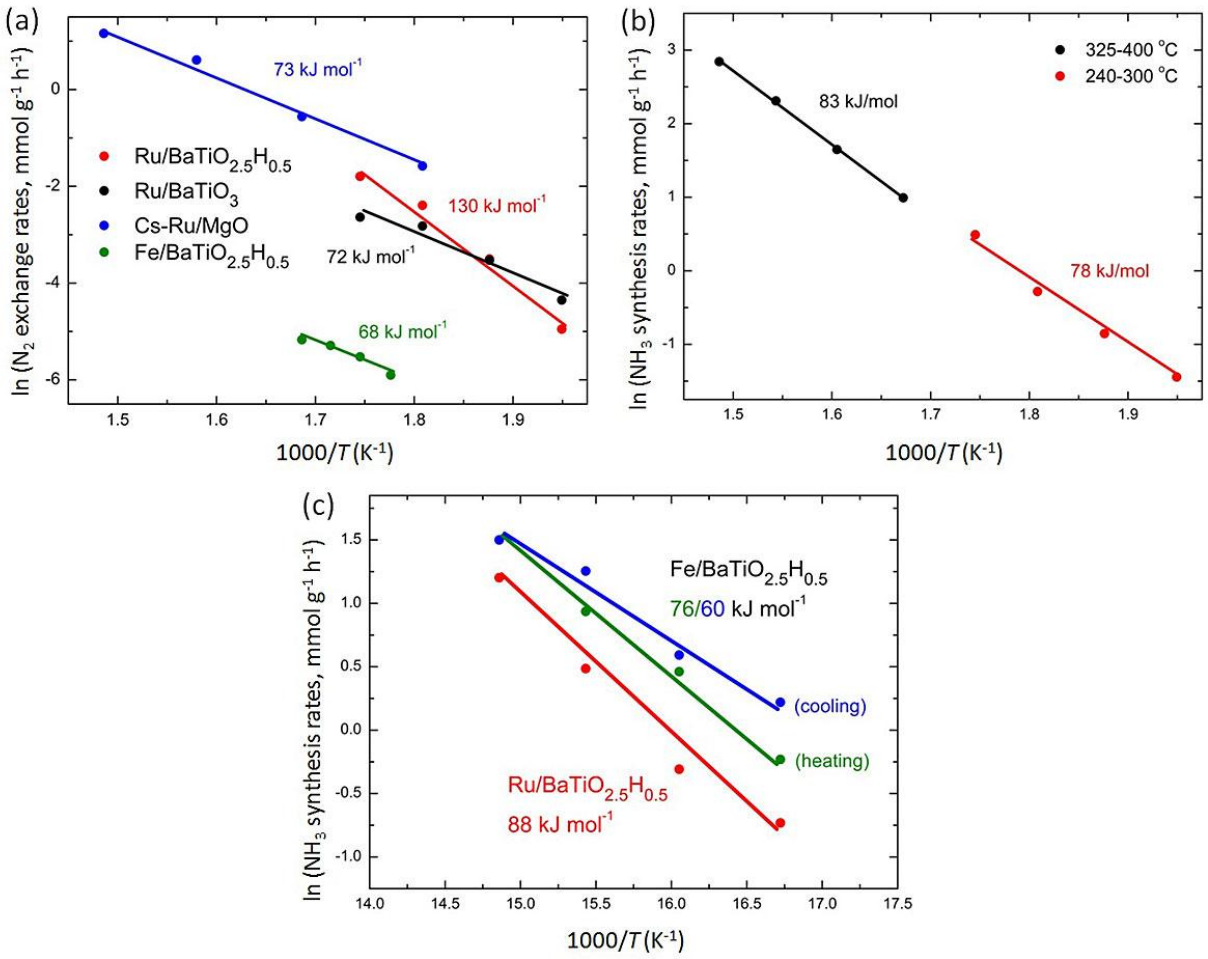

Figure 2.4. (a) Arrhenius plots for N_2 isotopic exchange. (b) Arrhenius plots for NH_3 synthesis over $Ru/BaTiO_{2.5}H_{0.5}$ at different temperature ranges. This indicates that our oxyhydride-supported Ru catalysts, unlike Ru/electride, have no temperature dependence of support effects with the reaction temperatures range from 240 to 400 ˚C. (c) Arrhenius plots for NH_3 synthesis over Ru, $Fe/BaTiO_{3-x}H_x$ at 0.1 MPa, temperature ranges from 325 to 400 ˚C.

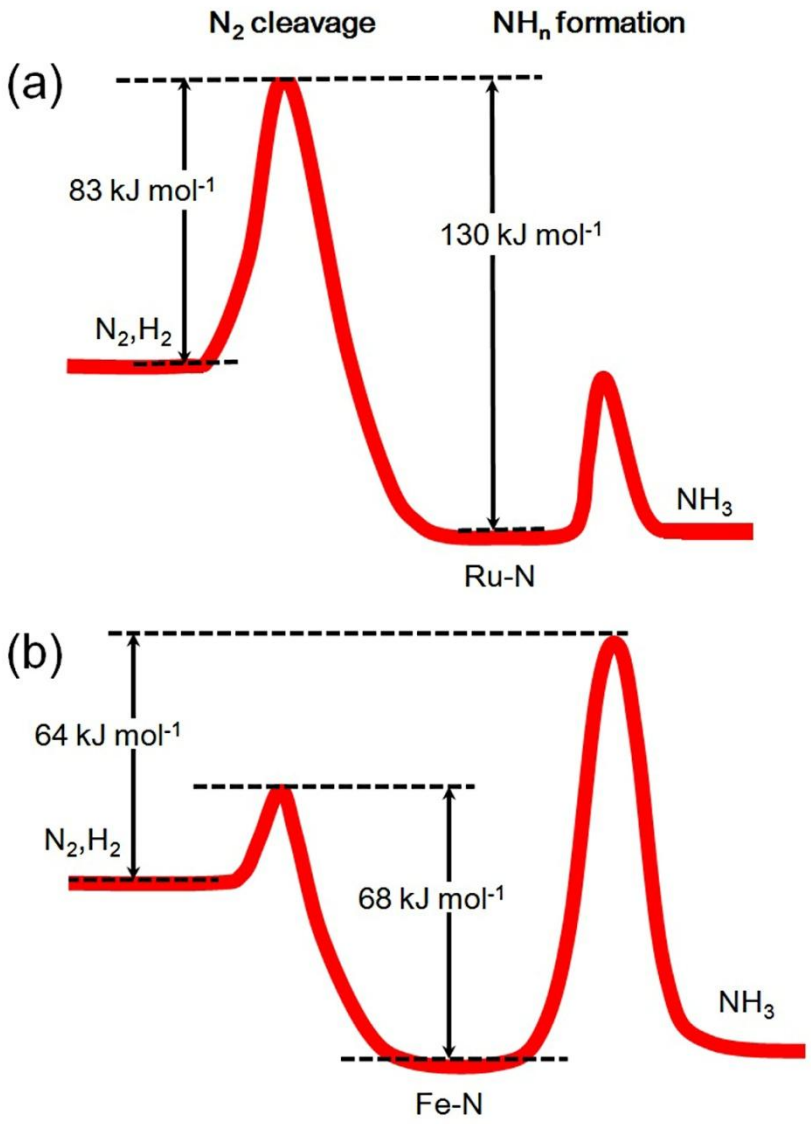

Figure 2.5. Energy profile of NH_3 synthesis and N_2 isotopic exchange over $Ru/BaTiO_{2.5}H_{0.5}$ (a) and $Fe/BaTiO_{2.5}H_{0.5}$ (b). The enthalpy change for the production of NH_3 from $N_2(g)$ and $H_2(g)$ is ca. −46 kJ mol^{-1}.[38]

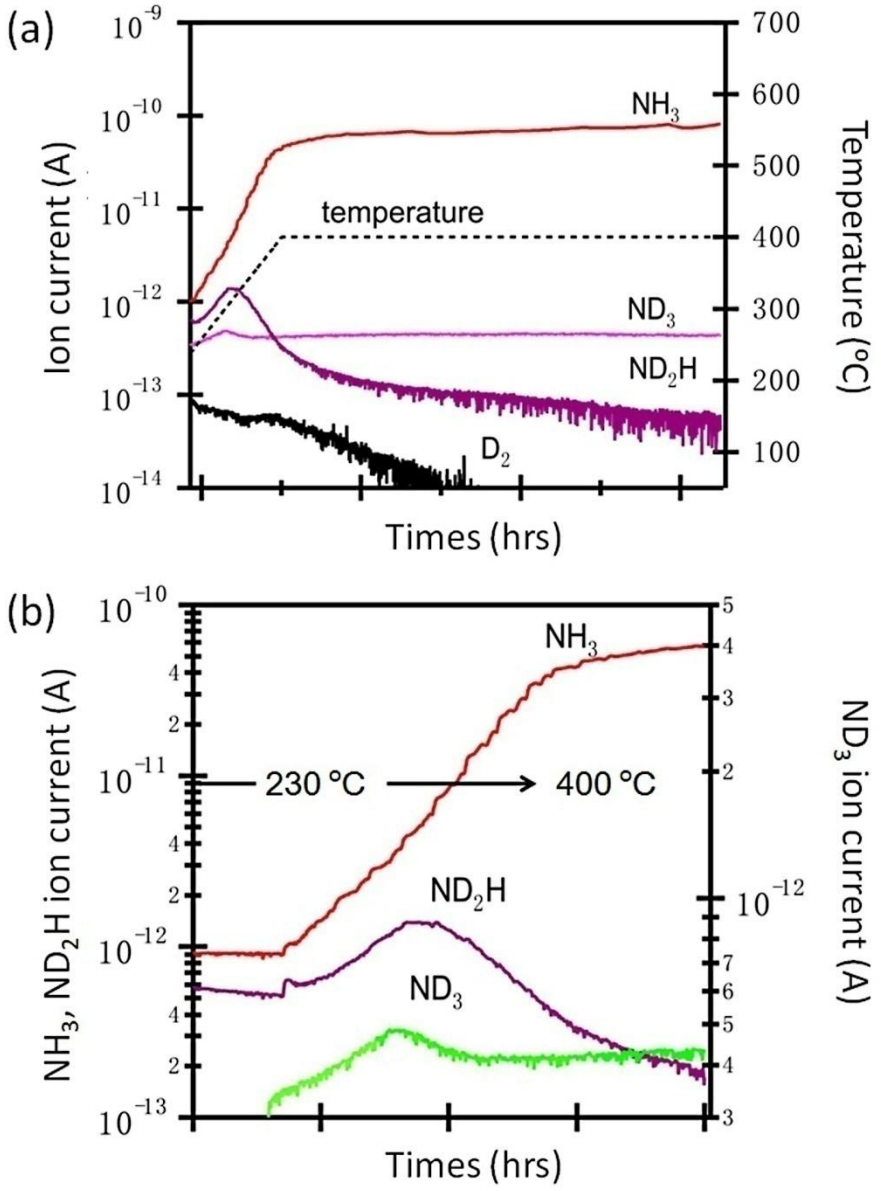

Figure 2.6. (a) Isotope products during ammonia synthesis. Various $N(H,D)_3$ products are monitored as the N_2/H_2 synthesis gas is flowed over a $Ru/BaTiO_{2.5}D_{0.5}$ catalyst. (b) is an enlargement of the first hour.

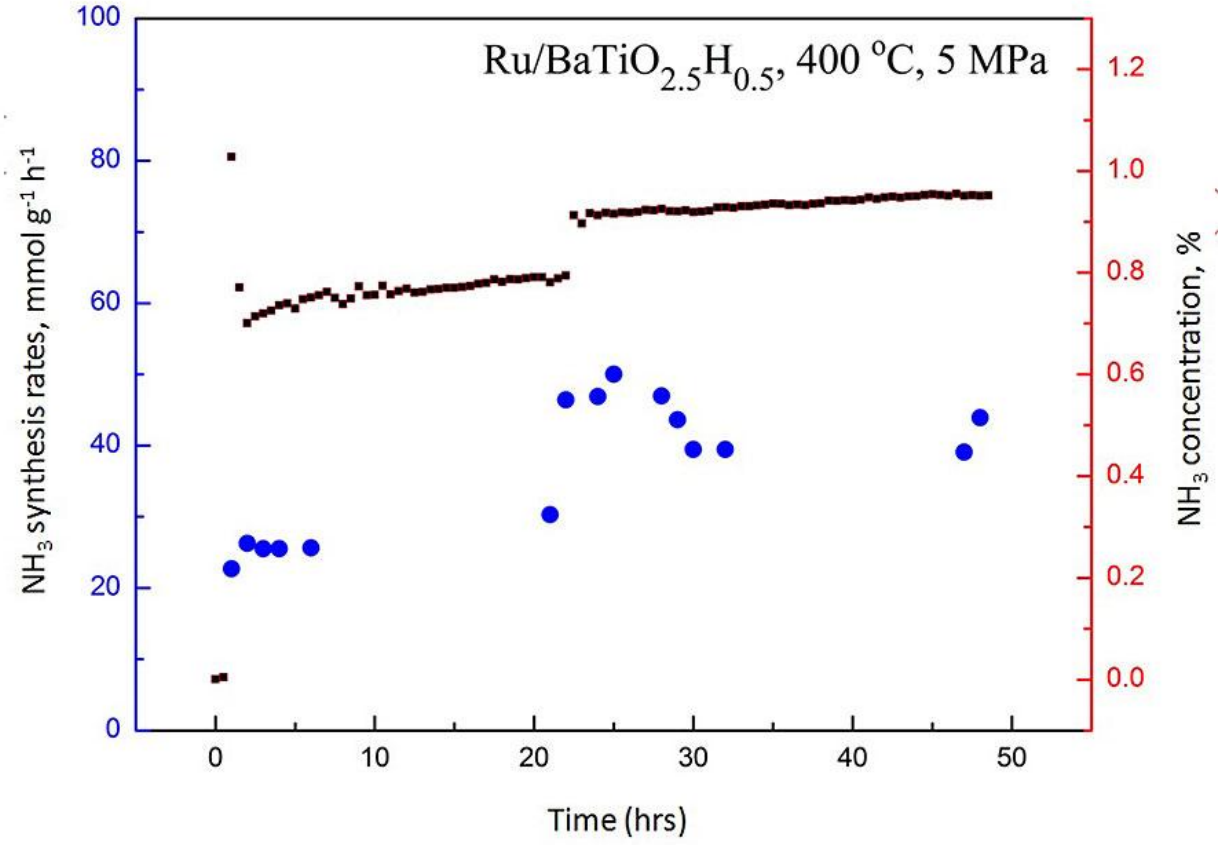

Figure 2.7. Stability of $Ru/BaTiO_{2.5}H_{0.5}$ for 48 hours reactions. Reaction conditions: 400 ˚C, 5 MPa. The blue dots show the results from an aqueous trap and NH_3-selective electrode, and the red dots show the NH_3 concentration during reactions from FT-IR measurements.

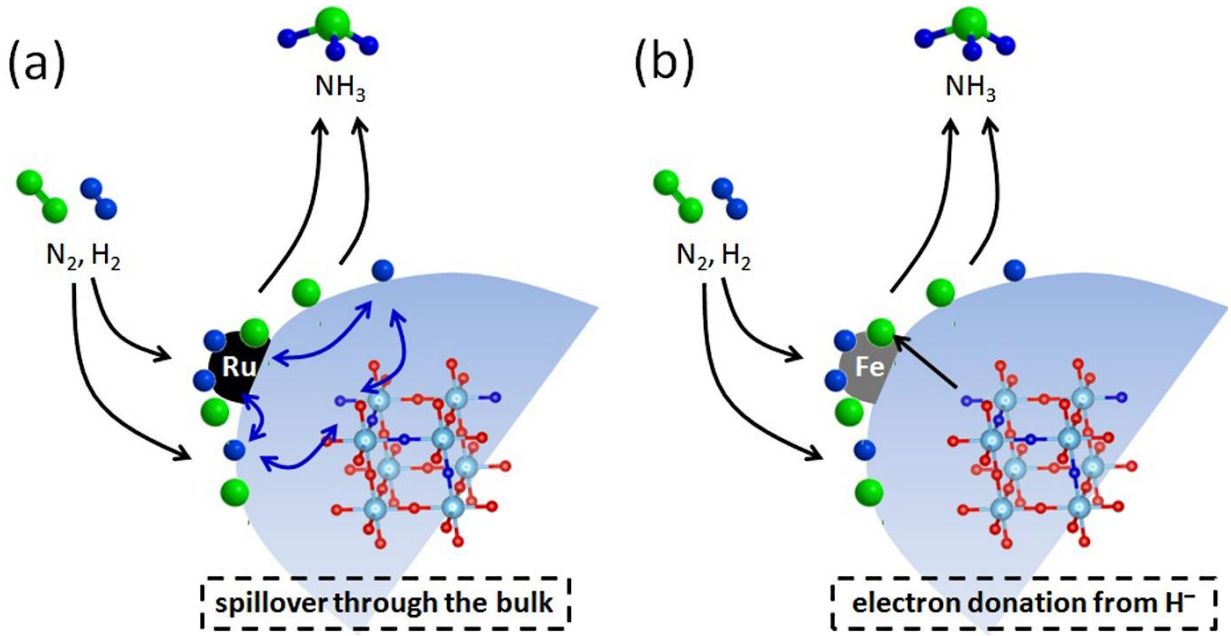

Figure 2.8. Possible metal-dependent mechanisms for the high activity. (a) Colossal spillover of H^- through the support, hindering H_2 poisoning on Ru. (b) Partial electron donation from H^- to the Fe (and possibly Co) particle, assisting in N_2 activation.

Chapter 3. Hydride-enhanced CO_2 methanation: water-stable $BaTiO_{2.4}H_{0.6}$ as a new support

3.1. Introduction

Heterogeneous metal catalysts are crucial to the modern chemical industry, involved in the synthesis and conversion of a broad range of chemicals such as ammonia, methane, and methanol.[1-3] Usually, in heterogeneous metal catalysts, support materials are extremely important and play a definitive role in the catalytic performance. In the past few years, a rising number of studies centered on searching for new types of catalytic supports with distinct electronic properties or surface/bulk anionic defects, such as electrides[4, 5] and metal hydrides.[6-8] A prime example is with ammonia synthesis, where inorganic electrides such as $12CaO{\cdot}7Al_2O_3{:}e^-$ (C12A7:e$^-$),[4, 9] $[Ca_2N]{:}e^-$,[10, 11] CaH_2,[8] Ca_2NH,[12] Y_5Si_3,[13] and LaScSi[14] exhibit excellent electron donation to adsorbed species,[4, 9, 15] enhancing activity. LiH[6] and BaH_2[7] have also been examined as catalytic supports for NH_3 synthesis, with lattice hydride (H^-) playing a decisive role in the hydrogenation of adsorbed nitrogen.[6, 16] The new recent activity concerning NH_3 synthesis, as opposed to other reactions, is doubtlessly related to the stability of the catalysts in these anhydrous and anaerobic environments. Other than Y_5Si_3, all of these materials are not water-stable.[17]

However, catalytic reactions involving water as a reactant or byproduct are quite numerous, such as the Fischer-Tropsch process,[18] steam reforming,[19] or the Sabatier reactions (CO_2 methanation)[20]. These reactions are challenging environments for any electride or hydride supports, as virtually all of these aforementioned electrides (except for Y_5Si_3, but only NH_3 synthesis was reported[13]) or hydrides are not stable in water. However, we note that the oxyhydride $BaTiO_{2.4}H_{0.6}$ is stable both in air and boiling water,[21] making it a good candidate for testing how hydride-based catalysts fare with these other types of reactions. We have previously confirmed that the lattice H^- in $BaTiO_{2.4}H_{0.6}$ can be exchanged with surrounding D_2 gas at 400 ˚C (based on neuron diffraction).[21] This H/D exchange involves D_2 bond dissociation and hints that various hydrogenation reactions may be possible. In a more recent study, we found a lattice hydride-involved (Mars–van Krevelen mechanism) formation of NH_3 on $BaTiO_{2.4}H_{0.6}$ under Haber-Bosch conditions,[22] indicating a great potential of oxyhydride for catalysis applications.

Hence, in this paper we examine the influence of hydride as it is introduced into a $BaTiO_3$ support when utilized as a catalyst for the Sabatier reaction ($CO_2 + 4H_2 \rightarrow CH_4 + 2H_2O$). The interesting feature of oxyhydride is the suspected electron donating power of H^-, which should be more than that from oxide anions (O^{2-}). Hence, the Lewis basicity (i.e.

the solid basicity) of oxyhydride may higher than the corresponding oxide. The importance of basicity for CO_2 methanation has already been previously discussed.[23-25] In this study, we have examined the activities of Ni/$BaTiO_{3-x}H_x$ and Ru/$BaTiO_{3-x}H_x$ catalysts finding that the activity is enhanced by 2–7 times, despite the water-rich environment. We also observe changes in reaction orders when compared to $BaTiO_3$-supported catalysts, indicating that activity change is due to the kinetics being influenced by hydride. This work demonstrates that the oxyhydride is an effective support material for CO_2 hydrogenation catalysis, and perhaps other water-involved catalytic processes.

3.2. Experimental Section

3.2.1. Catalyst preparation All of the reagents were of analytical grade and were used without any further purification. $BaTiO_3$ (100 nm particle size, provided by Sakai Chemical Industry Co., Ltd.) was preheated at 200 ˚C overnight to completely remove any adsorbed water. The $BaTiO_3$ powder was then ground with 3 molar equivalents of CaH_2, pelletized in a glovebox and then sealed in an evacuated Pyrex tube at pressures below 3×10^{-2} Pa.[21, 26] The tubes were then heated at 560 ˚C with different reaction durations to prepare $BaTiO_{3-x}H_x$ with different hydride contents.[27] The catalysts were prepared *via* the impregnation method. For 5 wt% Ni/$BaTiO_{3-x}H_x$, 0.703 g of $Ni(cod)_2$ (bis(1,5-cyclooctadiene)nickel), 99 %, Wako Co., Ltd.) powder were dissolved in 200 mL THF (tetrahydrofuran, 99.5 %, Wako Co., Ltd.) solution and 3 g of $BaTiO_{3-x}H_x$ powders were then added to the yellow solution, which was kept at room temperature for 4 hours under vigorous stirring. The THF slurry was then evaporated by rotary evaporation. The powder was sealed in an evacuated Pyrex tube and then heated at 120 ˚C for 6 hours and collected the sample in an N_2-filled glovebox. The same Ni impregnation method was conducted for ruthenium ($Ru_3(CO)_{12}$, trirutheniumdodecacarbonyl, 99 %, Wako Co., Ltd.) catalysts supported on oxides and oxyhydrides.

3.2.2. Catalytic activity measurements The catalysts were tested in a quartz reactor having a length of 300 mm and a diameter of approx. 10 mm, which was heated in a furnace. Typically, 100 mg catalysts were placed on quartz wool in the reactor and tested at temperatures ranging from 250 ˚C to 400 ˚C for 1 hour, respectively. The Ni-based catalysts were first reduced at 400 ˚C for 30 min (for Ru-based catalysts are 2 hours) under a pure H_2 flow at 90 mL min^{-1}. The gas flow was then switched to a reactant gas with a molar ratio of CO_2 : H_2 = 1 : 4 and the total flow rate was set to 90 mL min^{-1}. The outlet gas was analyzed online by gas chromatography (GC 490, Agilent Technologies) after cooling the effluent with a cold trap to remove excess H_2O.

3.2.3. Kinetic measurements The $BaTiO_3$ and $BaTiO_{2.4}H_{0.6}$-supported Ru catalysts (with 1 wt% metal deposition) were used in kinetic experiments. The hydride content of the oxyhydride support after Ru deposited was determined by Rietveld refinement of

Synchrotron data, see details in the part of charactering the anion content. The experiments were conducted in a fixed bed quartz reactor, the same with that in catalytic measurements. The kinetic experiment consists of two parts: the activation energy and the reaction order. We operated with low temperature (250–300 ˚C) to ensure low CO_2 conversation that the water level in the cold trap is low enough to minimize adsorption of gas species. The flow rates were controlled by mass flow controllers (MFC). The activation energy of the Ru-based catalysts were determined in the experiments that the temperature range from 250–300 ˚C and the flow rates were set at 100 mL min^{-1} with the mole ratio of CO_2 : H_2 : Ar = 15 : 60 : 25. Mixtures of CO_2, H_2 and Ar were used to determine the reaction order of H_2 and CO_2, which the experiment conditions are 275 ˚C with the flow rates are 100 mL min^{-1}.

3.2.4. Characterization X-ray diffraction (XRD) patterns were collected at room temperature by a Bruker D8 Advance diffractometer equipped with a Cu-Kα source (λ = 1.5406 Å). The synchrotron XRD experiments were performed at room temperature using a Debye−Scherrer camera installed at BL02B2 (λ = 0.42 Å) at SPring-8, JASRI. The synchrotron X-ray results were analyzed by the LeBail/Rietveld method with EXPGUI/GSAS.[28, 29] Thermal gravimetric analysis (TGA) was performed with a Rigaku Thermo Plus (TG 8120) using a Pt pan under flowing O_2 (300 mL min^{-1}). CO-pulse chemisorptions were conducted on a BELCAT instrument (BELCAT-II, BEL, Japan). The size and dispersion of the Ni and Ru particles were determined by CO-pulse adsorption at 50 ˚C using a He flow of 30 mL min^{-1} with intermittent pulses of 50 mL min^{-1} (9.97 % CO in He). Prior to the CO-pulse measurements, the catalyst was treated with flowing He (30 mL min^{-1}) at 50 ˚C for 10 minutes and then flowing H_2 (30 mL min^{-1}) at 400 ˚C for 120 minutes and cooling to 200 ˚C. Adsorbed hydrogen on the reduced catalysts was removed by purging with He (30 mL min^{-1}) at 50 ˚C for 15 minutes. A stoichiometry of Ni/CO = 1 and Ru/CO = 1 was assumed to calculate the metal dispersion. Ru and Ni contents were analyzed by Sumica Corp; samples were digested with by a sodium peroxide fusion, followed by acid extraction and ICP-AES analysis.

3.2.5. Characterizing the anion contents As we reported previously, the hydride contents in the $BaTiO_3$ lattice can be determined by various methods such as thermal gravimetric analysis (TGA, in air or oxygen), Rietveld refinement of X-ray diffraction data (synchrotron diffraction data or laboratory diffraction data), or neutron diffraction data.[21] Thermal gravimetric analysis of the $BaTiO_{3-x}H_x$ samples show a weight increase at the sample reverts to $BaTiO_3$.[27] Assuming that all anionic sites are occupied by either O^{2-} or H^- (our previous studies show that anion vacancies are negligible[21]), this weight increase is consistent with the formulae $BaTiO_{2.65}H_{0.35}$, $BaTiO_{2.56}H_{0.44}$, and $BaTiO_{2.38(1)}H_{0.62(1)}$, with the longer reaction times resulting in high hydride content. The increasing *a* lattice parameter is a good guide to the changes in hydride contents of the

cubic $BaTiO_{3-x}H_x$. The variation of the *a* lattice parameter of $BaTiO_{3-x}H_x$ is shown in our previously results.[27] It is evident that more hydride results in an increase of the lattice parameter of $BaTiO_{3-x}H_x$, from 4.02578(4) for x = 0.35 to 4.03300(3) for x = 0.62. Rietveld refinement of the synchrotron diffraction data (see details in the Figure 3.1a, c, and e) results in the formulae $BaTiO_{2.61(1)}H_{0.39(1)}$, $BaTiO_{2.55(1)}H_{0.45(1)}$ and $BaTiO_{2.44(1)}H_{0.56(1)}$, very close to that obtained from the thermal gravimetric analysis. More accurately, the lattice parameter of $BaTiO_{3-x}H_x$ extracted *via* a synchrotron refinement shows the very similar behavior with that from lab XRD results, with an increasing lattice parameter as the hydride contents increased (see details in Table 3.1). These consistent results led to the similar formulae $BaTiO_{2.65(4)}H_{0.35(4)}$, $BaTiO_{2.56(1)}H_{0.44(1)}$ and $BaTiO_{2.40(4)}H_{0.60(4)}$, which we take as our final composition for various $BaTiO_{3-x}H_x$ supports.

3.2.6. Method to calculate CH_4 conversion In this work, the CH_4 conversion was quantified by the following equation:

$$Y_{CH_4} = \frac{F_{CH_4,out}}{F_{CO_2,out} + F_{CH_4,out}}$$

where, $F_{CH4,\ out}$ is the flow rate of CH_4, and $F_{CO2,out}$ is the flow rate of CO_2 during the reaction. The produced CH_4 amounts during reaction were quantified by Micro GC (GC 490, Agilent Technologies) combined with a gas mixer.

3.3. Results and discussion

Three powder samples of $BaTiO_{3-x}H_x$ with x = 0.35, 0.44, and 0.60 were synthesized by reduction with CaH_2 (see the Supporting Information).[21] A symmetry change from the tetragonal *P4mm* space group to the cubic $Pm\bar{3}m$ space group is observed during conversion of the oxide to oxyhydride, which is due to the electron doping.[21, 26] We previously[21, 26] reported that the hydride content in the $BaTiO_3$ lattice can be determined by various methods, such as thermal gravimetric analysis (TGA[27]), Rietveld refinement of X-ray diffraction data (synchrotron or laboratory XRD, see Figure 3.1), or neutron diffraction data. These consistent results led to the similar formula of $BaTiO_{2.65}H_{0.35}$, $BaTiO_{2.56}H_{0.44}$, and $BaTiO_{2.4}H_{0.6}$ prepared with different reaction durations, which we take as our final compositions for various oxyhydride supports. More details for the anionic compositions are listed in Table 3.1.

3.3.1. Activity Figure 3.2 shows the CH_4 conversion of Ni and Ru catalysts supported on oxide ($BaTiO_3$) and oxyhydride ($BaTiO_{2.4}H_{0.6}$). For the Ni catalysts, the activities of both $Ni/BaTiO_3$ and $Ni/BaTiO_{2.4}H_{0.6}$ increased as the Ni loading amount increased from 1 wt% to 10 wt%. For the 5 wt% results (blue traces in Figure 3.2a), the CH_4 conversion of $Ni/BaTiO_{2.4}H_{0.6}$ (43%) at 350 ˚C is 5 times higher than that of $Ni/BaTiO_3$ (8%). At 10 wt%

(red traces in Figure 3.2a), we see a similar enhancement with the oxyhydride support. In general, the methanation activity of Ni/$BaTiO_{2.4}H_{0.6}$ is higher than Ni/$BaTiO_3$ between 250 ˚C to 400 ˚C, especially at the intermediate temperatures of 300 ˚C (insert of Figure 3.2a) and 350 ˚C. Other binary oxide supports have been examined extensively;[30] among these, the widely studied Ni/Al_2O_3 (16 wt%) was reported to have CH_4 conversion of 55% at 400 ˚C,[31] almost comparable with our 5 wt% Ni/$BaTiO_{2.4}H_{0.6}$ (ca. 53% conversion at 400 ˚C) despite the difference in metal loading. Furthermore, the CH_4 conversion of 5 wt% Ni/$BaTiO_{3-x}H_x$ with diverse hydride contents (x = 0.35–0.6) were also examined under the identical conditions. As shown in Figure 3.3, Ni/$BaTiO_{2.4}H_{0.6}$ yield highest methanation activity at 350 ˚C (see the Supporting Information), demonstrating that the hydride is the main enhancement factor.

For the Ru catalysts, depositing the Ru particles requires impregnating with $Ru_3(CO)_{12}$ and then treating under vacuum at 390 ˚C; this process results in some loss of hydride, as we have confirmed the composition Ru/$BaTiO_{2.67}H_{0.33}$ (Figure 3.1f). As shown in Figure 3.2b (red traces), the CH_4 conversion of Ru/$BaTiO_{2.67}H_{0.33}$ achieved its constant activity (probably limited by thermodynamics) at approximately 350 ˚C. The activity of Ru-based catalyst was enhanced nearly 2.5 times when the support was changed from oxide to oxyhydride (300–375 ˚C). Ru/$BaTiO_{2.67}H_{0.33}$ appears to be more active at 300 ˚C with approximately 50% CH_4 conversion. The results indicate that the oxyhydride support drastically enhances the catalytic activity. Note that while the highest activity is obtain with Ru/$BaTiO_{2.67}H_{0.33}$, our oxyhydride-supported Ni catalysts already surpass oxide-supported Ru catalysts at 350 ˚C, showing that the activity can be drastically enhanced without resorting to previous metals.

To ensure an accurate comparison between the various catalysts, the metal particle sizes and dispersion were examined by CO-pulse adsorption experiments, with the results were summarized in Table 3.2. For the 5 wt% and 10 wt% Ni catalysts, no significant differences in metal dispersion between $BaTiO_3$ and $BaTiO_{3-x}H_x$-supported catalysts are seen. Ru particle sizes were also examined, resulting in 3.1 nm for Ru/$BaTiO_3$ and 2.7 nm for Ru/$BaTiO_{2.67}H_{0.33}$ after reactions. The real deposited Ni, Ru amounts were examined by ICP-AES; as shown in Table 3.2, with the same nominally Ni amounts (1, 5, 10 wt%), the actual metal loading amounts are very similar both for oxide and oxyhydride supports. This indicates that the prepared metal catalysts show very similar metal size/dispersion effects for CO_2 methanation.

3.3.2. Stability In the Sabatier reaction, every mole of reacted CO_2 yields two moles of H_2O byproduct. We have previously confirmed the stability of $BaTiO_{2.5}H_{0.5}$ under boiling conditions with H_2O,[21] but not yet explicitly tested the upper limits in terms of temperature. Potentially, water may act as a weak oxidizing (or acidic) agent and reduce the hydride content in the oxyhydride support. Hence, we have monitored the activities

of $Ni/BaTiO_{2.4}H_{0.6}$ and $Ni/BaTiO_3$ over a period of 10 hours at 350 ˚C, as shown in Figure 3.4a, and then examined the catalyst after the reaction.

Throughout the 10 hours, the $Ni/BaTiO_3$ catalyst is approximately stable in terms of activity. The activity of the $Ni/BaTiO_{2.4}H_{0.6}$ catalyst somewhat decreases during the first 1~2 hours, but afterwards remains fairly constant and is still higher than the activity of $Ni/BaTiO_3$ (25% vs. 5% CH_4 conversion). During this test, some Ni sintering for both catalysts was observed, but occurred in almost identical amounts for both catalysts. For the $Ni/BaTiO_3$ catalyst, the particle size as observed from CO-pulse adsorption increased from 53 nm to 87 nm, and for the oxyhydride-supported catalyst, the analogous particle sizes were 45 nm and 87 nm.

The partial decrease in activity of $Ni/BaTiO_{2.4}H_{0.6}$ over time is probably due to partial loss of hydride, but also suggests that after the initial loss there is remaining hydride in the catalyst, preserving the overall enhanced activity. Figure 3.4b, c show Rietveld refinements of synchrotron XRD of the catalysts before and after the 10 hours reaction. According to these results, the formula of catalyst sample before reaction is $Ni/BaTiO_{2.48}H_{0.52}$, and this changes to $Ni/BaTiO_{2.72}H_{0.28}$ after the reaction. The changes in anion content also agree with the change in lattice parameters resulting from oxidation of Ti (see Table 3.1). Almost half of the hydride is lost, but as the activity is stable after the initial two hours, the partially oxidized catalyst is probably in a meta-stable state where the residual hydride, perhaps further away from the surface, remains and still has effects on the surface catalysis reactions.

3.3.3. Kinetics Different catalysts can be distinguished by their characteristic activation energies and reaction orders; hence, we have examined these parameters for our $Ru/BaTiO_3$ and $Ru/BaTiO_{2.67}H_{0.33}$ catalysts. The literature for Ru is more developed than for Ni, so we have not examined our Ni catalysts in this regard. Activation energies are more difficult to interpret, and numerous possible mechanisms have been proposed for CO_2 methanation[32-34] involving various intermediate species and hence different rate-determining step (RDS). As shown in Figure 3.5a, the activation energies were 95 kJ mol^{-1} for $Ru/BaTiO_{2.67}H_{0.33}$ and 97 kJ mol^{-1} for $Ru/BaTiO_3$. In comparison, the activation energy of Ru/Al_2O_3 is approximately 66 kJ mol^{-1}[35] and for Ru/TiO_2 is approximately 80 kJ mol^{-1}.[36, 37]

The reaction orders are shown in Figure 3.5b, c. The CO_2 reaction order for $Ru/BaTiO_3$ is 0.26 and for $Ru/BaTiO_{2.67}H_{0.33}$ is 0.27, which is quite close to that for Ru/Al_2O_3 (α = 0.34)[35] and Ru/TiO_2 (α = 0.22).[37] This suggests that there is no difference between the two supports for CO_2 side of the reaction. For the H_2 order there is a marked change, as $Ru/BaTiO_3$ has a negative reaction order (β = −0.53), whereas the reaction order for H_2 of $Ru/BaTiO_{2.67}H_{0.33}$ is positive (β = 0.79). This change itself is curious, but we also note that the negative reaction order observed with $Ru/BaTiO_3$ is the most

surprising, as other studies all report positive H_2 reaction orders (0.46~0.88 for Ru/Al_2O_3, 0.43~0.57 for Ru/TiO_2)[35, 36, 38, 39]. Whether the negative order is due to the presence of Ba is not clear, as Ba would first be expected to impart basicity,[40] but we do not see any changes in CO_2 reaction order, and hence the reaction is dominated by the hydrogen side of the reaction. There is no literature regarding reaction orders of explicitly basic supports such as Ba, or Mg-containing supports. In any event, phenomenally, $Ru/BaTiO_3$ seems to suffer from H_2 poisoning (similar to during NH_3 synthesis[4, 9]) and this is alleviated with the presence of hydride (perhaps hydrogen spillover). We note that all kinetic experiments have been conducted at low conversions (~5%–8%), far away from equilibrium.

Compared to other reactions such as NH_3 synthesis, the proposed reaction mechanisms of CO_2 methanation are numerous and more complex, possibly involving CO route or formate route.[33, 34, 41] In a CO-mediated mechanism, the CO dissociation into C and O atoms was found to be the RDS.[42] Alternatively, CH_4 formation occurs via the C–O bond cleavage was proposed in a formate route,[43, 44] in which, the reaction of *HCO dissociation to *CH + *O was predicted to be the RDS.[45] Turning to hydrogen side of the reaction, in general, CO_2 hydrogenation on the metal surface can occur through Eley–Rideal (ER) or Langmuir–Hinshelwood (LH) mechanisms, depending on how hydrogen reacts with the adsorbed CO_2.[46, 47] Duyar *et al.*[35] have recently reported that when the H_2 order is close to 1 (β = 0.88), the reaction is consistent with an Eley–Rideal (ER) mechanism, but with more lower activation energy (66 kJ mol^{-1}).

Despite these contradictory scenarios, however, CO_2 dissociation into CO is sometimes considered as a poisoning effect on hydrogen adsorption, both for Ru and Ni.[31, 48] In our own experiments, no CO was detected during catalytic measurements and kinetic measurements. Moreover, the methanation activity increased with the enhancement of the hydrogen adsorption on catalyst surface. It thus can simply to consider that the oxyhydride support increase the H_2 adsorption ability during CO_2 hydrogenation, and enhances activity.

3.4. Conclusions

In summary, the perovskite-type oxyhydride $BaTiO_{2.4}H_{0.6}$ was discovered to be an effective water-stable support material for CO_2 methanation. Kinetic analysis of the Ru-based catalysts shows how both oxyhydride and oxide supports have similar activation energies and CO_2 reaction orders but quite different H_2 reaction orders. Explaining the origins of these reaction orders requires more study. From a more general point of view, our study is the first demonstration of a hydride-based catalyst in a hostile environment and shows that we can still explore new catalysts in a variety of chemical

conversions. The hydride here seems to be adequately stabilized in the perovskite oxide lattice; perovskites are a large material family with many minor structural and compositional modifications possible. The number of perovskite-based transition metal oxyhydrides similar to our $BaTiO_{3-x}H_x$ system has increased substantially over the past few years,[49, 50] so further systematically investigating the oxyhydride support effect within this system should be fruitful in the future.

References

1. Deutschmann, O.; Knözinger, H.; Kochloefl, K.; Turek, T., In Ullmann's Encyclopedia of Industrial Chemistry; Wiley-VCH Verlag GmbH & Co. KGaA: **2000**.

2. Norskov, J. K.; Bligaard, T.; Rossmeisl, J.; Christensen, C. H., *Nat. Chem.* **2009**, *1*, 37.

3. Gao, F.; Goodman, D. W., *Annu. Rev. Phys. Chem.* **2012**, *63*, 265.

4. Kitano, M.; Inoue, Y.; Yamazaki, Y.; Hayashi, F.; Kanbara, S.; Matsuishi, S.; Yokoyama, T.; Kim, S. W.; Hara, M.; Hosono, H., *Nat. Chem.* **2012**, *4*, 934.

5. Hara, M.; Kitano, M.; Hosono, H., *ACS Catal.* **2017**, *7*, 2313.

6. Wang, P.; Chang, F.; Gao, W.; Guo, J.; Wu, G.; He, T.; Chen, P., *Nat. Chem.* **2017**, *9*, 64.

7. Gao, W.; Wang, P.; Guo, J.; Chang, F.; He, T.; Wang, Q.; Wu, G.; Chen, P., *ACS Catal.* **2017**, *7*, 3654.

8. Kitano, M.; Inoue, Y.; Ishikawa, H.; Yamagata, K.; Nakao, T.; Tada, T.; Matsuishi, S.; Yokoyama, T.; Hara, M.; Hosono, H., *Chem. Sci.* **2016**, *7*, 4036.

9. Kitano, M.; Kanbara, S.; Inoue, Y.; Kuganathan, N.; Sushko, P. V.; Yokoyama, T.; Hara, M.; Hosono, H., *Nat. Comm.* **2015**, *6*, 6731.

10. Kim, Y. J.; Kim, S. M.; Cho, E. J.; Hosono, H.; Yang, J. W.; Kim, S. W., *Chem. Sci.* **2015**, *6*, 3577.

11. Kim, Y. J.; Kim, S. M.; Hosono, H.; Yang, J. W.; Kim, S. W., *Chem. Comm.* **2014**, *5*0, 4791.

12. Abe, H.; Niwa, Y.; Kitano, M.; Inoue, Y.; Sasase, M.; Nakao, T.; Tada, T.; Yokoyama, T.; Hara, M.; Hosono, H., *J. Phys. Chem. C* **2017**, *121*, 20900.

13. Lu, Y.; Li, J.; Tada, T.; Toda, Y.; Ueda, S.; Yokoyama, T.; Kitano, M.; Hosono, H., *J. Am. Chem. Soc.* **2016**, *138*, 3970.

14. Wu, J.; Gong, Y.; Inoshita, T.; Fredrickson, D. C.; Wang, J.; Lu, Y.; Kitano, M.; Hosono, H., *Adv. Mater.* **2017**, 1700924.

15. Hayashi, F.; Toda, Y.; Kanie, Y.; Kitano, M.; Inoue, Y.; Yokoyama, T.; Hara, M.; Hosono, H., *Chem. Sci.* **2013**, *4*, 3124.

16. Vojvodic, A.; Medford, A. J.; Studt, F.; Abild-Pedersen, F.; Khan, T. S.; Bligaard, T.; Nørskov, J. K., *Chem. Phys. Lett.* **2014**, *598*, 108.

17. Buchammagari, H.; Toda, Y.; Hirano, M.; Hosono, H.; Takeuchi, D.; Osakada, K., *Org. Lett.* **2007**, *9*, 4287.

18. Dry, M. E., *Catal. Today* **2002**, *71*, 227.

19. Mei, D.; Lebarbier Dagle, V.; Xing, R.; Albrecht, K. O.; Dagle, R. A., *ACS Catal.* **2016**, *6*, 315.

20. Cokoja, M.; Bruckmeier, C.; Rieger, B.; Herrmann, W. A.; Kühn, F. E., *Angew. Chem. Int. Ed.* **2011**, *50*, 8510.

21. Kobayashi, Y.; Hernandez, O. J.; Sakaguchi, T.; Yajima, T.; Roisnel, T.; Tsujimoto, Y.; Morita, M.; Noda, Y.; Mogami, Y.; Kitada, A.; Ohkura, M.; Hosokawa, S.; Li, Z.; Hayashi, K.; Kusano, Y.; Kim, J.; Tsuji, N.; Fujiwara, A.; Matsushita, Y.; Yoshimura, K.; Takegoshi, K.;

Inoue, M.; Takano, M.; Kageyama, H., *Nat. Mater.* **2012**, *11*, 507.
22. Kobayashi, Y.; Tang, Y.; Kageyama, T.; Yamashita, H.; Masuda, N.; Hosokawa, S.; Kageyama, H., *J. Am. Chem. Soc.* **2017**, *139*, 18240.
23. Tomishige, K.; Chen, Y.-g.; Fujimoto, K., *J. Catal.* **1999**, *181*, 91.
24. Lemonidou, A. A.; Vasalos, I. A., *Appl. Catal. A: Gen.* **2002**, *228*, 227.
25. Seok, S.-H.; Choi, S. H.; Park, E. D.; Han, S. H.; Lee, J. S., *J. Catal.* **2002**, *209*, 6.
26. Sakaguchi, T.; Kobayashi, Y.; Yajima, T.; Ohkura, M.; Tassel, C.; Takeiri, F.; Mitsuoka, S.; Ohkubo, H.; Yamamoto, T.; Kim, J.; Tsuji, N.; Fujihara, A.; Matsushita, Y.; Hester, J.; Avdeev, M.; Ohoyama, K.; Kageyama, H., *Inorg. Chem.* **2012**, *51*, 11371.
27. Tang, Y.; Kobayashi, Y.; Shitara, K.; Konishi, A.; Kuwabara, A.; Nakashima, T.; Tassel, C.; Yamamoto, T.; Kageyama, H., *Chem. Mater.* **2017**, *29*, 8187.
28. a. C. Larson and R. B. Von Dreele, *Structure*, **2004**, *748*, 86-748.
29. a. C. Larson, R. B. Von Dreele and B. H. Toby, *J. Appl. Crystallogr.*, **2001**, *748*, 2001-2001.
30. Kattel, S.; Liu, P.; Chen, J. G., *J. Am. Chem. Soc.* **2017**, DOI: 10.1021/jacs.7b05362.
31. Garbarino, G.; Riani, P.; Magistri, L.; Busca, G., *Int. J. Hydrogen Energy* **2014**, *39*, 11557.
32. Ren, J.; Guo, H.; Yang, J.; Qin, Z.; Lin, J.; Li, Z., *Appl. Surf. Sci.* **2015**, *351*, 504.
33. Wang, W.; Wang, S.; Ma, X.; Gong, J., *Chem. Soc. Rev.* **2011**, *40*, 3703.
34. Cheng, D.; Negreiros, F. R.; Aprà, E.; Fortunelli, A., *ChemSusChem* **2013**, *6*, 944.
35. Duyar, M. S.; Ramachandran, A.; Wang, C.; Farrauto, R. J., *J. CO_2 Util.* **2015**, *12*, 27.
36. Prairie, M. R.; Renken, A.; Highfield, J. G.; Ravindranathan Thampi, K.; Grätzel, M., *J. Catal.* **1991**, *129*, 130.
37. Bell, A. T.; Marwood, M.; Doepper, R.; Prairie, M.; Renken, A., *Chem. Eng. Sci.* **1994**, *49*, 4801.
38. Kuśmierz, M., *Catal. Today* **2008**, *137*, 429.
39. Traa, Y.; Weitkamp, J., *Chem. Eng. Technol.* **1999**, *22*, 291.
40. Horiuchi, Y.; Kamei, G.; Saito, M.; Matsuoka, M., *Chem. Lett.* **2013**, *42*, 1282.
41. Wang, F.; He, S.; Chen, H.; Wang, B.; Zheng, L.; Wei, M.; Evans, D. G.; Duan, X., *J. Am. Chem. Soc.* **2016**, *138*, 6298.
42. Choe, S.-J.; Kang, H.-J.; Kim, S.-J.; Park, S.-B.; Park, D.-H.; Huh, D.-S., *Bull. Korean Chem. Soc.* **2005**, *26*, 1682.
43. Kattel, S.; Yan, B.; Chen, J. G.; Liu, P., *J. Catal.* **2016**, *343*, 115.
44. Kattel, S.; Yu, W.; Yang, X.; Yan, B.; Huang, Y.; Wan, W.; Liu, P.; Chen, J. G., *Angew. Chem. Int. Ed.* **2016**, *128*, 8100.
45. Avanesian, T.; Gusmão, G. S.; Christopher, P., *J. Catal.* **2016**, *343*, 86.
46. Lin, W.; Stocker, K. M.; Schatz, G. C., *J. Am. Chem. Soc.* **2017**, *139*, 4663.
47. Rettner, C. T.; Auerbach, D. J., *Science* **1994**, *263*, 365.
48. Borgschulte, A.; Gallandat, N.; Probst, B.; Suter, R.; Callini, E.; Ferri, D.; Arroyo, Y.; Erni,

R.; Geerlings, H.; Zuttel, A., *Phys. Chem. Chem. Phys.* **2013**, *15*, 9620.
49. Denis Romero, F.; Leach, A.; Möller, J. S.; Foronda, F.; Blundell, S. J.; Hayward, M. A., *Angew. Chem. Int. Ed.* **2014**, *126*, 7686.
50. Bang, J.; Matsuishi, S.; Hiraka, H.; Fujisaki, F.; Otomo, T.; Maki, S.; Yamaura, J.-i.; Kumai, R.; Murakami, Y.; Hosono, H., *J. Am. Chem. Soc.* **2014**, *136*, 7221.

Table 3.1. Details of hydride contents and lattice parameters of oxyhydride supports.

Samples	TG results (in O_2 flow)	Lattice parameter (lab Cu-Kα XRD, determined by TOPAS software)	Rietveld analysis of Synchrotron XRD
$BaTiO_{3-x}H_x$ (4 days)	0.35	4.02578(4)	$BaTiO_{2.61(1)}H_{\mathbf{0.39(1)}}$ 4.02866(3)
5 wt% Ni/ $BaTiO_{3-x}H_x$ (4,*b*)	–	4.02584(5)	$BaTiO_{2.61(1)}H_{\mathbf{0.39(1)}}$ 4.02808(3)
$BaTiO_{3-x}H_x$ (6 days)	0.44	4.03045(4)	$BaTiO_{2.55(1)}H_{\mathbf{0.45(1)}}$ 4.030265(8)
5 wt% Ni/ $BaTiO_{3-x}H_x$ (6,*b*)	–	4.03064(5)	$BaTiO_{2.55(1)}H_{\mathbf{0.45(1)}}$ 4.03068(2)
$BaTiO_{3-x}H_x$ (7 days)	0.62	4.03300(3)	$BaTiO_{2.44(1)}H_{\mathbf{0.56(1)}}$ 4.03208(1)
5 wt% Ni/ $BaTiO_{3-x}H_x$ (7,*b*)	–	4.03271(4)	$BaTiO_{2.48(1)}H_{\mathbf{0.52(1)}}$ 4.03196(3)
5 wt% Ni/ $BaTiO_{3-x}H_x$ (7,*a*) after 350 ˚C, 10 hrs	–	4.02755(7)	$BaTiO_{2.72(1)}H_{\mathbf{0.28(1)}}$ 4.02681(4)

[a] denotes after reaction; [b] denotes before reaction.

Table 3.2. Catalytic performances of Ni and Ru-based catalysts.

Catalysts	Ni or Ru (wt%)		Conversion (%)[b]	Metal size (nm)[c]
	Nominal	Actual[a]		
$Ni/BaTiO_3$	1	0.89	3	26
	5	3.3	8	53
	10	6.6	11.7	96
$Ni/BaTiO_{2.4}H_{0.6}$	1	0.92	7.8	15
	5	3.9	43	44
	10	6.9	46.6	98
$Ni/BaTiO_{2.65}H_{0.35}$	5	–	15.8	51
$Ni/BaTiO_{2.56}H_{0.44}$	5	–	18	47
$Ru/BaTiO_3$	1	0.77	33	–
$Ru/BaTiO_{2.67}H_{0.33}$	1	0.78	82	–

[a] Ni/Ru contents were determined by ICP-AES; [b] at 350 ˚C, CH_4 conversion was calculated by the method which details in the Supporting Information; [c] after H_2 reduction (conditions: 400 ˚C for 30 mins), based on CO-pulse results.

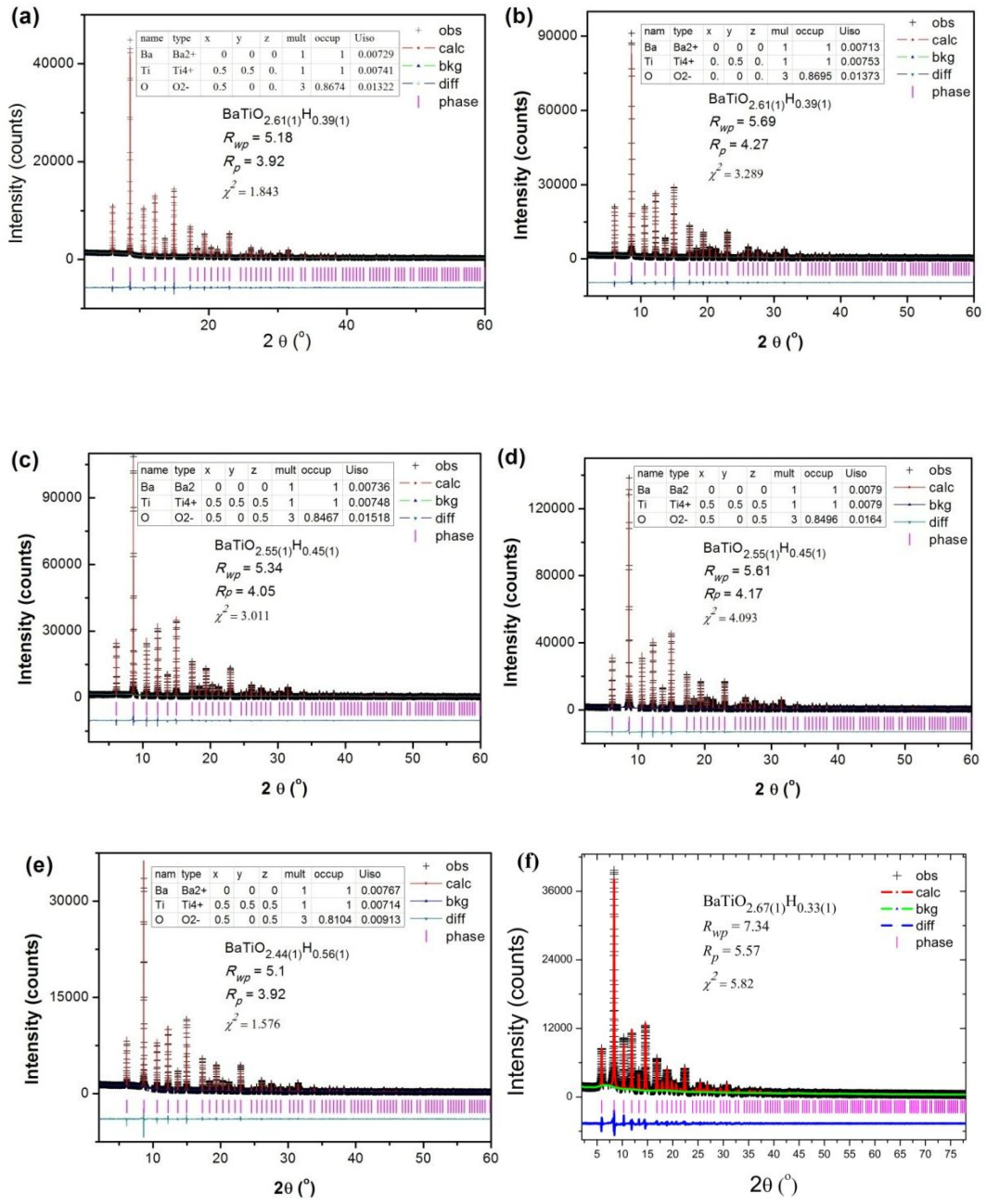

Figure 3.1. Rietveld refinement of synchrotron data. (a) $BaTiO_{3-x}H_x$ (four days); (b) 5 *wt*% $Ni/BaTiO_{3-x}H_x$ (four days); (c) $BaTiO_{3-x}H_x$ (six days); (d) 5 *wt*% $Ni/BaTiO_{3-x}H_x$ (six days); (e) $BaTiO_{3-x}H_x$ (seven days); (f) 1 wt% $Ru/BaTiO_{3-x}H_x$.

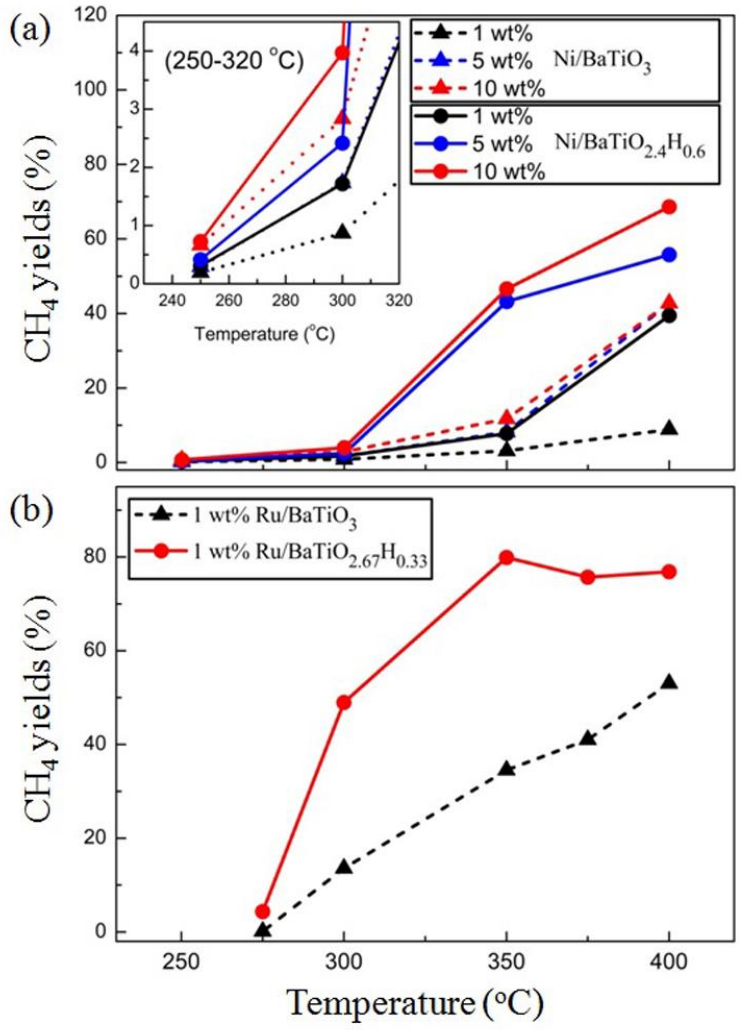

Figure 3.2. CH_4 conversion rates of (a) Ni and (b) Ru catalysts supported on oxide and oxyhydride (100 mg catalysts, CO_2:H_2 = 1:4, flow rate = 90 mL min^{-1}, 1 atm).

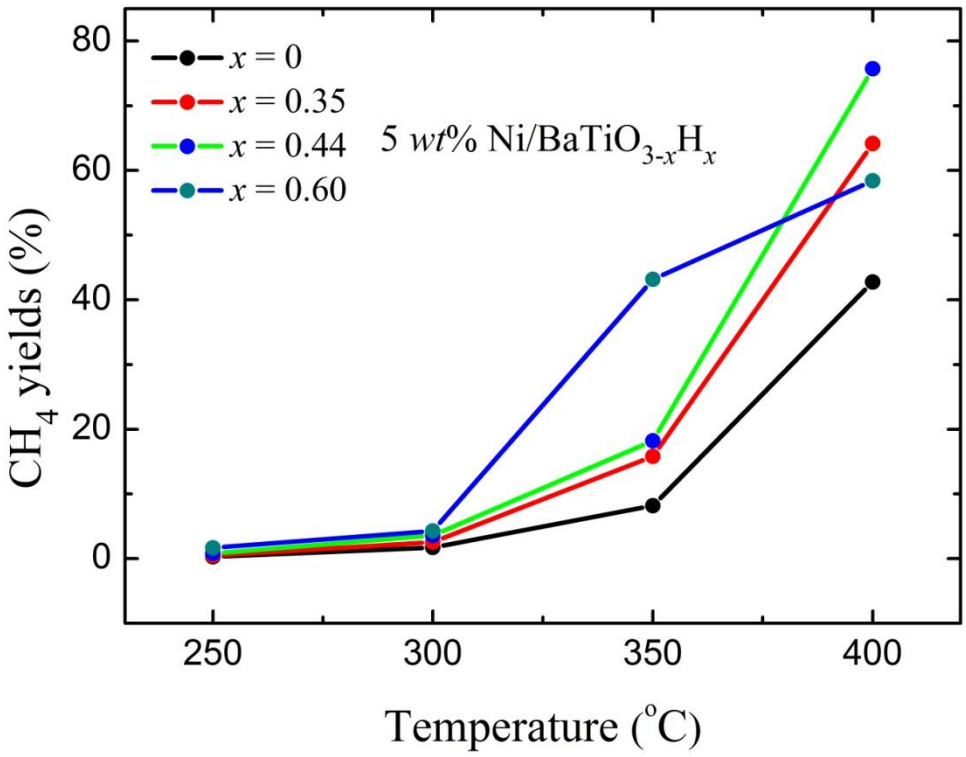

Figure 3.3. CH_4 conversion of Ni catalysts as a function of hydride contents in various oxyhydride supports (100 mg catalysts, CO_2:H_2 = 1:4, flow rate = 90 mL min^{-1}, 1 atm).

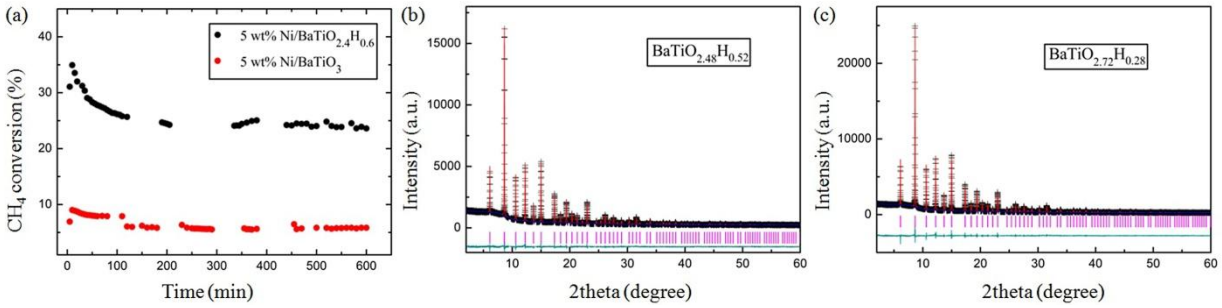

Figure 3.4. (a) 10 hours stability test of 5 wt% Ni/$BaTiO_{2.4}H_{0.6}$ and 5 wt% Ni/$BaTiO_3$ (100 mg catalysts, CO_2:H_2 = 1:4, flow rate = 90 mL min^{-1}, 1 atm, 350 ˚C). Rietveld refinements of synchrotron data for 5 wt% Ni/$BaTiO_{2.4}H_{0.6}$ (b) before (R_{wp} = 6.90%, R_p = 4.67%, χ^2 = 1.45) and (c) after (R_{wp} = 5.30%, R_p = 4.07%, χ^2 = 1.65) 350 ˚C, 10 hours of reaction.

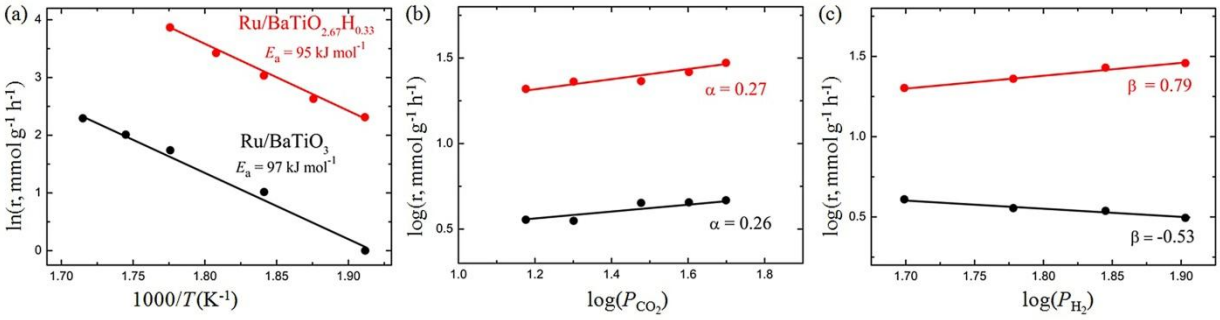

Figure 3.5. Kinetic analyses of Ru-based catalysts. (a) Arrhenius plots of activity for $Ru/BaTiO_3$ and $Ru/BaTiO_{2.67}H_{0.33}$ for CO_2 methanation over 250–300 ˚C. (b) and (c) are CO_2 and H_2 reaction order plots of $Ru/BaTiO_3$ (black line) and $Ru/BaTiO_{2.67}H_{0.33}$ (red line), respectively.

Chapter 4. On hydride diffusion in transition metal perovskite oxyhydrides investigated via deuterium exchange

4.1. Introduction

Perovskite oxyhydrides with a sizable amount of hydride anions (H^-) in the lattice possess potential for a wide range of applications.[1-4] One of these potentials is where the hydride lability is exploited for various synthetic uses.[5-7] For example, $BaTiO_{3-x}H_x$ ($x \leq 0.60$) has been shown to be a useful precursor for topotactic conversion to oxynitrides *via* H/N exchange under moderate conditions.[7] Other mixed anion phases impossible to access otherwise, such as $BaTi(O,H,F)_3$ and $BaTi(O,H,OH)_3$ have also been reported using the anion exchange reactions starting from titanium oxyhydrides.[5-7]

A growing number of oxyhydrides have been reported in recent years include $SrCrO_2H$,[3] $Sr_{n+1}V_nO_{2n+1}H_n$ (n = 1, 2, ∞),[4, 8] $LaSrMnO_{3.3}H_{0.70}$,[9] and $BaScO_2H$.[10] Given the lighter mass, smaller charge, larger polarizability, and larger redox potential of H^- compared to that of oxide anion, hydride conductivity in oxyhydrides is an interesting subject to pursue, but experimental studies on this topic are still quite limited. Bridges *et al.* examined H^- diffusion in the anion-ordered oxyhydride $LaSrCoO_3H_{0.70}$ with the Ruddlesden-Popper type perovskite structure by means of quasi-elastic neutron scattering (QENS). It was shown that H^- hopping along the one-dimensional (1D) H^- array *via* 30% vacancies along the *a* axis is extremely fast, with an activation energy of ca. 20 kJ mol^{-1}.[11] Very recently, Kanno and co-workers demonstrated pure H^- conduction in $La_{2-x-y}Sr_{x+y}LiH_{1-x+y}O_{3-y}$ using impedance measurements, revealing that two-dimensional (2D) H^- conduction in the layered lithium perovskite is facilitated by introducing H^- vacancies (y),[12] though the activation energy of 68.4 kJ mol^{-1} for $La_{0.6}Sr_{1.4}LiH_{1.6}O_2$ (x = 0.40 and y = 1.0) is somewhat larger than that in $LaSrCoO_3H_{0.70}$.

Unlike $LaSrCoO_3H_{0.70}$ and $La_{2-x-y}Sr_{x+y}LiH_{1-x+y}O_{3-y}$, we did not detect any anion vacancies in $BaTiO_{3-x}H_x$ at ambient temperature by means of structural refinement of X-ray/neutron diffraction data.[1] However, a small amount of H^- may leave as hydrogen gas at elevated temperatures (300–450 °C), providing the necessary anion vacancy for three-dimensional (3D) bulk oxide/hydride diffusion. A non-trivial hopping mechanism involving electron transfer from H to Ti followed by diffusion and recombination has been theoretically proposed by Iwazaki *et al*.[13] Recent calculations by Liu *et al*. have also examined the activation energy of hydride diffusion in the $BaTiO_3$ lattice.[14] Unfortunately, the high electronic conductivity of $ATiO_{3-x}H_x$ (A = Ca, Sr, Ba, and Eu)[1, 15-17] does not permit the direct

measurement of H^- conductivity by an impedance measurement. The H^- diffusion in $A\mathrm{TiO}_{3-x}\mathrm{H}_x$ has been indirectly observed *via* the bulk nature of hydride exchange reactions with D,[1] N,[5, 7] or F.[5] Although there are some arguments linked to the H^- diffusion (or lability) in $A\mathrm{TiO}_{3-x}\mathrm{H}_x$,[1, 2, 6, 16] none of them provided any quantitative estimates of activation energy and its relation with the lattice hydride concentration. To understand the H^- diffusion (or H^- exchange) mechanism in $A\mathrm{TiO}_{3-x}\mathrm{H}_x$ and other oxyhydrides in general, a universal method that enables quantitative arguments on hydride diffusion, even in the presence of electronic conductivity, would be helpful as such oxyhydrides may find various ionic-based applications.

In this work, the kinetics of H/D exchange and H_2 release in $\mathrm{BaTiO}_{3-x}\mathrm{H}_x$ (x = 0.35–0.60) and $\mathrm{LaSrCoO_3H_{0.70}}$ are probed using thermally evolved gas analysis (by quadrupole mass spectrometry, QMS), where the activation energies for these two processes were obtained by the Kissinger method. The Kissinger method, as originally proposed,[18] relies on some characteristic temperature determined from the experiments (e.g., thermogravimetry (TG) and QMS) carried at different linear heating rate β. The Kissinger method has been used quite often to determine the activation energy of H_2 release from metal hydrides (e.g., TiH_2 and MgH_2)[19] and other hydrogen storage materials (e.g., $Mg(NH_2)_2$ and $LiNH_2$).[20-22] In terms of H/D exchange, a study on NaH has only been reported.[23] In this study, it was found that bulk diffusion, rather than any surface reactions, was to be rate-limiting; hence this technique using gas-phase analysis can be used to probe bulk hydride diffusion. A systematic study of $\mathrm{BaTiO}_{3-x}\mathrm{H}_x$ and comparison with $\mathrm{LaSrCoO_3H_{0.70}}$ by using Kissinger analysis enables one to argue probable hydride hopping process of the whole system, providing a general guide to design and improve H^- conductivity in oxyhydrides.

4.2. Experimental Section

4.2.1. Preparation of oxyhydrides Four powder samples of $\mathrm{BaTiO}_{3-x}\mathrm{H}_x$ with x = 0.35, 0.39, 0.44, and 0.60 were synthesized by low temperature topochemical reactions with CaH_2.[1] $BaTiO_3$ (0.23 g, 100 nm particle size, provided by Sakai Chemical Industry Co., Ltd.), preheated at 200 ˚C overnight to completely remove any adsorbed water, was ground with 3 molar equivalents of CaH_2 (0.12 g, 99.9%, Aldrich), pelletized in a glove box and then sealed in an evacuated Pyrex tube at pressures below 3×10^{-2} Pa. Heating the tubes at 560 ˚C for 4, 5, 6 and 7 days resulted in the formation of phase-pure $\mathrm{BaTiO}_{3-x}\mathrm{H}_x$ with x = 0.35, 0.39, 0.44, and 0.60. The XRD patterns of these compounds are shown in Figure 4.1. $\mathrm{BaTiO}_{3-x}\mathrm{D}_x$ (x

= 0.47) was prepared in the same manner using a 3 molar excess of CaD_2, where CaD_2 was synthesized by reacting calcium metal (99.9%, Wako) under D_2 gas (99.8%, Taiyo Nippon Sanso) at 600 ˚C. After the reaction completion, the CaO reaction product and the excess CaH_2/CaD_2 were washed out of the reaction product using a 0.1 M NH_4Cl solution in methanol.

We followed the synthetic procedure of $LaSrCoO_3H_{0.70}$ as described in the original report.[24, 25] The starting material $LaSrCoO_4$ (3.0 g) was prepared by the citric acid method, where powder specimens of La_2O_3 (1.40 g, 99.9%, Wako), $SrCO_3$ (1.27 g, 99.9%, Wako), and elemental cobalt (0.51 g, 99.9%, Wako) were weighed out in stoichiometric quantities and dissolved in dilute nitric acid with citric acid. To synthesize $LaSrCoO_3H_{0.70}$ (0.28 g), $LaSrCoO_4$ (0.30 g) mixed with CaH_2 (0.07 g) (1:2 molar ratio) was reacted at 450 ˚C for 2 days in a sealed evacuated Pyrex tube, followed by washing with 0.1 M NH_4Cl solution in methanol for purification. The cell parameters are in agreement with those of reported (Table 4.1).[24, 25]

4.2.2. Characterizing the hydride content As previously reported,[1] the hydride content in $BaTiO_{3-x}H_x$ can be determined by combined methods including TG (under air or O_2 flow), Rietveld refinement of X-ray and neutron diffraction patterns, and thermal desorption spectroscopy (TDS). Here, we mainly used TG and synchrotron Rietveld refinement. The TG experiments were performed using a Rigaku Thermo Plus (TG 8120) under flowing pure O_2 at 300 mL min^{-1}. A Pt pan was used as a sample holder. TG data showed a weight increase as the oxyhydride sample reverts to $BaTiO_3$ (Figure 4.2). Assuming that all the anionic sites are fully occupied by either O^{2-} or H^-, as demonstrated previously,[1] we estimated the hydride content from the weight change. This gave $BaTiO_{2.65}H_{0.35}$, $BaTiO_{2.61}H_{0.39}$, $BaTiO_{2.56}H_{0.44}$, and $BaTiO_{2.40}H_{0.60}$ for the samples prepared with CaH_2 for a period of 4, 5, 6 and 7 days, respectively. All these compounds adopt cubic perovskite structure, with the cell parameter increasing in proportion with x (from 4.02578(4) Å for x = 0.35 to 4.03208(1) Å for x = 0.60, see Table 4.2), in accordance with the previous study. Rietveld refinement of synchrotron X-ray diffraction data for the specimen hydride-reduced for 5 days yielded the oxygen content of 2.61(1), in excellent agreement with the aforementioned TG result. Synchrotron Rietveld refinement for other two compositions also yielded consistent results, as summarized in Table 4.2.

4.2.3. H/D exchange and H_2 release experiments Thermal analysis measurements were conducted using a Rigaku Thermo Plus thermal balance linked to QMS (Pfeiffer Omni Star). H/D exchange and H_2 release experiments were performed at different linear heating rates of 1, 5, 10, 20 and 30 ˚C min^{-1} (2, 15, 20, 30, 40 ˚C min^{-1} for $LaSrCoO_3H_{0.70}$) over the temperature range of 30 ˚C to 700 ˚C

under flowing 5% D_2/Ar or pure Ar. The oxyhydride samples (typically ~17 mg) of $BaTiO_{3-x}H_x$ and $LaSrCoO_3H_{0.70}$ were placed in a Pt crucible for the experiment. A linear heating rate was then applied in QMS measurements, resulting in a HD or H_2 release peak, which is depending on the gas choice. This is recorded as a function of time, and then analyzed using a Kissinger formula. Prior to the thermal measurement, the samples were treated with flowing pure Ar (200 mL min^{-1}) at 120 ˚C for 2 hours to remove adsorbed water on the surface of the particles. Subsequently, the H/D exchange measurements were performed with 5% D_2 in Ar (100 mL min^{-1}). The same Ar pretreatment was also conducted before the H_2 release measurements.

4.2.4. DFT calculations First-principles calculations for $BaTiO_{3-x}H_x$ and $LaSrCoO_3H$ were performed using the projector augmented wave (PAW) method as implemented in the VASP code.[26-29] Configurations of valence electrons of PAW potentials are $5s^2$ $5p^6$ $6s^2$ for Ba, $3p^6$ $3d^2$ $4s^2$ for Ti, $2s^2$ $2p^4$ for O, $1s^1$ for H, $5s^2$ $5p^6$ $6s^2$ $5d^1$ $4f^0$ for La, $4s^2$ $4p^6$ $5s^2$ for Sr, and $3p^6$ $3d^7$ $4s^2$ for Co. The exchange-correlation term was treated with the local density approximation (LDA).[30] The plane-wave cutoff energies were set to be 550 eV. Strong correlation effects of 3d orbitals are taken into account within a frame work of GGA+U method.[31] The parameters of effective U potential are 4.49eV[14, 32] and 4.0 eV[33] for Ti 3d and Co 3d, respectively. The size of $\boldsymbol{k}$-point sampling meshes are 6 × 6 × 6 and 6 × 6 × 2 for the unit cell of $BaTiO_3$ and $LaSrCoO_3H$. The calculated lattice parameters of a tetragonal $BaTiO_3$ unit cell were $a = b$ = 3.983 Å, c = 3.996 Å, and c/a = 1.003. These values are in agreement with experimental values.[34, 35] A tetragonal $BaTiO_3$ supercell containing 40 atoms was constructed by 2 × 2 × 2 expansion of an optimized unit cell. Integration in reciprocal space was performed with 3 × 3 × 3 meshes. $LaSrCoO_3H_{0.70}$ is reported to have a defective K_2NiF_4-type structure with a space group of *Immm*.[24] La^{3+} and Sr^{2+} ions randomly occupy the same 4*i* site and H^- ions are situated at the 2*d* sites with 70% occupancy. We constructed ordered $LaSrCoO_3H$ structure with a space group of *Imm*2 similar to that in Ref. [25]. Optimized lattice parameters of $LaSrCoO_3H$ are a = 3.824 Å, b = 3.513 Å, and c = 12.647 Å. Although the amounts of hydrogen are different, the optimized lattice constants of $LaSrCoO_3H$ are comparable values with those of $LaSrCoO_3H_{0.70}$. A $LaSrCoO_3H$ supercell containing 56 atoms was constructed by 2 × 2 × 1 expansion of an optimized unit cell. Integration in reciprocal space was performed with 4 × 4 × 2 meshes.

The nudged elastic band (NEB) method[36, 37] was applied to calculate the energy barrier of the hydride hopping in $BaTiO_3$ lattice. We have selected the hydride jump pathway along nearest-neighbour (NN) and second

nearest-neighbour (2NN) sites. For NEB calculations, an H atom and a vacancy with the NN or 2NN configuration were placed at O sites in the $BaTiO_3$ supercell. In the case of $LaSrCoO_3H$, an hydride ion vacancy are created in the $LaSrCoO_3H$ supercell. Charge states of the defective supercells were set to be neutral. Effective charges of vacancies were compensated by reduction of Ti valence states. Spinpolarization was taken into account for all calculations.

4.3. Results

4.3.1. H/D exchange on $BaTiO_{3-x}H_x$ Figure 4.3a presents how HD evolves from $BaTiO_{3-x}H_x$ (x = 0.35) when it is heated under flowing 5% D_2/Ar at different heating rates (β = 1, 5, 10, 20, 30 ˚C min^{-1}). Increasing β led to a systematic increase of the peak temperature T_m, while the curve shape remains roughly the same. T_m increases from 390 ˚C at β = 1 ˚C min^{-1} to 422 ˚C at β = 30 ˚C min^{-1}. A similar trend has been observed for other compositions (x = 0.39, 0.44, and 0.60), as shown in Figure 4.3b, c, and d. In Figure 4.4a, we plotted T_m values in these samples as a function of β.

When heated under pure Ar flow at β = 30 ˚C min^{-1}, $BaTiO_{2.4}H_{0.6}$ releases H_2 gas at around 400 ˚C (Figure 4.5). Interestingly, heating under D_2 flow at the same heating rate of β = 30 ˚C min^{-1} results in the hydride exchange taking place at a very similar temperature of 400 ˚C.[1, 7] In order to further understand the effect of H_2 release behavior as a function of x and β, we heated the samples of x = 0.35, 0.39, 0.44, and 0.60 under pure Ar at various β, the result of which is shown in the rest of Figure 4.5. At a constant β, T_m values for H/D exchange and H_2 release are quite similar. For x = 0.60, for example, T_m at β = 30 ˚C min^{-1} is 429.5 ˚C and 433 ˚C for H/D exchange and H_2 release, respectively (Figure 4.6a). The same behaviour is also observed in the other compositions. This suggests that D_2 cleavage on the surface is not the rate-determining step (RDS) for H/D exchange, and as we later discuss, we assume the kinetics of H_2 release and H/D exchange processes to reflect kinetics of hydride diffusion within the bulk. A similar assumption has been found to be solid by Borgschulte *et al*,[23] that is, the bulk deuterium exchange (or bulk hydride diffusion) in NaH is RDS. We also note that the sample mass used does not influence the H_2 release temperature (Figure 4.7).

For the curves in Figure 4.3, some minor shoulders near the peaks can be seen. In Figure 4.3, as a trend, the higher temperature subpeak seems to increase in size as the hydride concentration is increased. The presence of multiple peaks or shoulders may result from slight inhomogeneities in anionic composition[2] and/or multiple diffusion steps.[38-40] However, exploration of these complex factors was

beyond the scope of this study as the peaks are not separated enough to be deconvoluted. We note that time total amount of H_2 or HD recorded as obtained by integrating *vs.* time is approximately equivalent for all runs (Table 4.3).

4.3.2. Kissinger analysis The Kissinger equation[18] is given by

$$\ln\frac{\beta}{T_m^2} = -\frac{E_a}{R}\frac{1}{T_m} + \ln A$$

where R is the universal gas constant, E_a is the apparent activation energy for the process during H/D exchange or H_2 release. This equation has a linear relationship between $\ln(\beta/T_m^2)$ and $1/T_m$. Using the obtained values of β and T_m, a $\ln(\beta/T_m^2)$ *vs.* $1/T_m$ plot was fitted to the linear equation to obtain the E_a values for H/D exchange (Figure 4.4b) and H_2 release. The activation energies are plotted in Figure 4.6b; it is clearly seen that for both processes, E_a depends considerably on the H^- content. We also conducted D/H exchange on $BaTiO_{2.53}D_{0.47}$ (under flowing 5% H_2/Ar), and found an E_a value of approximately 200 kJ mol^{-1} (Figure 4.8b), which is similar with that of H/D exchange on $BaTiO_{2.56}H_{0.44}$ (237 ± 7 kJ mol^{-1}). All the E_a values were summarized in Table 4.4.

Figure 4.6b compares the E_a values of H/D exchange and H_2 release on $BaTiO_{3-x}H_x$ with different H^- contents, from which three conclusions can be drawn. First, the activation energies of both processes for the same sample are similar to each other, though a certain deviation is seen at x = 0.39. Second, the E_a drastically reduces with increasing hydride content until it reaches around x_{th} ~0.4 (a threshold hydride concentration). Third, at higher hydride concentrations beyond x_{th} ~0.4, the E_a values hardly change (200–220 kJ mol^{-1}). Here, as we previously mentioned, the H_2 release process presumably involves various reaction steps including bulk diffusion in the perovskite anion lattice, surface H–H recombination, and desorption, whereas initial D–D bond cleavage is additionally necessary for the H/D exchange reaction. However, the RDS for both H_2 release and H/D exchange processes in $BaTiO_{3-x}H_x$ most likely corresponds to a bulk H^- diffusion in the anion lattice since other steps typically have much smaller energy barriers. For example, E_a for surface H/D exchange on $BaCe_{0.90}Y_{0.10}O_{2.95}$ surface has been reported to be 30 kJ mol^{-1}.[41]

4.3.3. H/D exchange on $LaSrCoO_3H_{0.70}$ Prior to this study, Bridges *et al.* analysed H^- transport in $LaSrCoO_3H_{0.70}$ using QENS.[11] On the basis of a 1D hydride hopping model through 2NN sites, they obtained an activation energy of 19.5–22.1 kJ mol^{-1}. This value is, however, remarkably lower than those of $BaTiO_{3-x}H_x$ (E_a > 200 kJ mol^{-1}) and even prototypical proton conductors such as $BaZrO_3$, $CaZrO_3$ (70–90 kJ mol^{-1}),[42, 43] $Sr_2(Sc_{1+x}Nb_{1-x})O_{6-x/2}$ (52–60 kJ mol^{-1}),[44] and Y-doped $BaZrO_3$ (43 kJ mol^{-1}).[45] Here, we investigated H/D exchange and H_2 release behaviours for

$LaSrCoO_3H_{0.70}$ under a continuous flow of D_2/Ar and pure Ar, respectively. As shown in Figure 4.9a, we found two peaks of HD appearing during heating under D_2/Ar flow. The first peak appears at around 300–400 ˚C, which is hereafter denoted as peak 1, and the other at around 600–650 ˚C (denoted as peak 2).

Analysis of an XRD pattern of the sample quenched from 410 ˚C during the D_2 treatment showed that the original orthorhombic structure (*Immm*) was preserved with negligible changes to the lattice parameters (Figure 4.10a, b and Table 4.1). Thus, peak 1 can be ascribed to a reversible H/D exchange, as found in $BaTiO_{3-x}H_x$. At temperatures beyond peak 1, the HD release increases continuously with increasing temperature until it forms a second peak at 600–650 ˚C. The crystal structure of the sample after the 700 ˚C treatment (both for D_2/Ar and Ar) turned out to be of tetragonal symmetry (*I4/mmm*) with lattice parameters being close to reported $LaSrCoO_{3.57(1)}$.[25] Thus, above peak 1 (~430˚C), the hydride anion in $LaSrCoO_3H_{0.70}$ is slowly and topochemically removed, and almost completely converts back to the pristine oxide at ~700 ˚C. Moreover, the asymmetric peak shape for peak 2 is also reminiscent of a decomposition reaction.[18, 46, 47]

The H_2 release experiment on $LaSrCoO_3H_{0.70}$ displays a similar tendency to the H/D exchange, with T_m increasing with β (see the inset of Figure 4.9a). Applying the Kissinger method to $LaSrCoO_3H_{0.70}$, one finds roughly the same E_a values for both processes (Figure 4.9b): 193 ± 8 kJ mol^{-1} for H/D exchange and 170 ± 16 kJ mol^{-1} for H_2 release. Obviously, these values are much larger than what has been obtained by QENS,[11] but are quite interestingly close to those obtained for $BaTiO_{3-x}H_x$ with $x_{th} > 0.4$.

4.4. Discussion

We have already demonstrated in Figure 4.6b that the apparent activation energy E_a for H/D exchange and H_2 release in $BaTiO_{3-x}H_x$ shows a characteristic x dependence, where E_a decreases substantially with x in the low concentration region up to x_{th} ~0.4, and beyond 0.4 it becomes nearly constant. This observation is of great interest as it can give a hint on the hydride migration pathway in the perovskite lattice. We previously speculated on two possible diffusion mechanisms at low and high H^- concentrations without any experimental verification.[1] The initial vacancy necessary for oxide/hydride diffusion may be supplied by a small amount of hydride desorbing at elevated temperatures; then, at low H^- concentrations, the migration of oxide anion (O^{2-}) would be necessary together with hydride diffusion. The inclusion of O^{2-} diffusion should result in a high activation energy. At high hydride concentrations, as H^- (and in-situ formed

vacancy) paths connect, diffusion is not dependent on O^{2-}, and a lower activation energy results. The present study (Figure 4.6b) not only provides a qualitative support for this view, but also allows for more detailed discussions on the diffusion mechanism with some quantitative insight.

At low H^- concentration (below x_{th} ~0.4), O^{2-} hopping is necessary, as shown in Figure 4.11a. Consistent with this assumption, a relatively high activation energy of ~370 kJ mol^{-1} at x = 0.35 was observed in this study. In an oxygen isotope tracer ($^{16}O_2/^{18}O_2$) experiment on CaO,[48] E_a for bulk oxide diffusion has been estimated to be in the range of 183–326 kJ mol^{-1}, reasonably agreeing with our study. Oxygen diffusion in $BaTiO_3$ has been widely studied by various methods, and the E_a values for bulk oxygen diffusion in $BaTiO_3$ range from 190 to 270 kJ mol^{-1}.[49-54] Impedance measurements on oxide ion conductors, such as $LaGaO_3$, $Ba_2In_2O_5$, and $MgSiO_3$, have also yielded similarly high E_a values of 120–300 kJ mol^{-1},[55, 56] and even 370 kJ mol^{-1}.[57] Based on the high E_a values (~360 kJ mol^{-1}) observed in $BaTiO_{3-x}H_x$ with x = 0.35, we presume that our results also reflect bulk oxygen diffusion in the anion lattice. When the hydride concentration is higher than the threshold value ($0.4 < x$), the activation energy is smaller (200–220 kJ mol^{-1}) and is nearly independent of x, suggesting that only hydride anions participate in the diffusion process.

Usually, oxide hopping in perovskite oxide conductors is dominated by NN jumps.[58] Through extensive studies on the O^{2-} transport in layered perovskite-based oxides such as $Sr_3Fe_2O_{7-x}$,[58] NN hopping is energetically more favourable compared with 2NN hopping. In $BaTiO_{3-x}H_x$, hydride diffusion *via* NN sites appears to be the relevant process in high H^- concentration, as shown in Figure 4.11c. However, recalling that each anion in $BaTiO_{3-x}H_x$ has eight NN anion sites (i.e., four NN anion sites per octahedron), anion sites must be at least 25% occupied (randomly) by hydride to achieve a 3D percolation pathway of hydride. This requirement gives rise to a hydride content of $x \geq 0.75$, which is well beyond the hydride content of currently available $x \leq 0.60$.[1] Therefore, the hydride transport for $x_{th} < x < 0.75$ probably includes both NN and 2NN hopping processes, as illustrated in Figure 4.11b. One can then naturally expect that the RDS for $x_{th} < x < 0.75$ is the 2NN hopping of hydride, rather than the NN hopping.

The activation energy of hydride migration along NN and 2NN jumps in $BaTiO_{3-x}H_x$ and $LaSrCoO_3H_{0.70}$ were calculated theoretically by the NEB method. Figure 4.11e illustrates the calculated energy profiles of the hydride migration pathways. For 2NN jumps, the calculated values for $BaTiO_{3-x}H_x$ and $LaSrCoO_3H_{0.70}$ are quite close, being 313 kJ mol^{-1} and 325 kJ mol^{-1}, respectively. The calculated E_a of hydride migration along the NN sites in $BaTiO_{3-x}H_x$ is obviously lower, at 96 kJ mol^{-1}. Experimentally, the observed E_a for $BaTiO_{3-x}H_x$ at $0.40 < x < 0.60$ is 200~220

kJ mol^{-1}, making the distinction between NN *vs.* 2NN jumps based on absolute E_a values ambiguous. However, we note that experimentally, the E_a for H/D exchange for $BaTiO_{3-x}H_x$ and $LaSrCoO_3H_{0.70}$ are equal, as they were theoretically. Structurally, only 2NN jumps are permitted for $LaSrCoO_3H_{0.70}$ (Figure 4.11d). Hence, while there is systematic error between theory and calculation, the calculations serve as strong evidence for 2NN hopping in series with NN hopping in $BaTiO_{3-x}H_x$ at $0.40 < x < 0.60$. Hypothetically, at $x > 0.75$, the last remnants of 2NN hopping would disappear, with NN hopping taking over completely.

In a computational study, Iwazaki *et al.*[13] looked at the energetics of various scenarios during hydride diffusion through a $BaTiO_3$ lattice. Although their calculations assume a very low concentration of hydride and no polarons, one of their findings was that energetically, it is favourable for hydride to dissociate into a proton and two electrons, followed by separate diffusion and recombination at an oxygen vacancy. This mechanism is intriguing as it does not require oxide ions to diffuse during the apparent hydride diffusion. We have looked at differential charge density maps and Bader charge analysis to look for any protonic character of hydrogen during H^- diffusion (Figure 4.12). For both NN and 2NN jumps, we see that hydride keeps essentially all of its anionic character during diffusion, so we do not see any evidence of this mechanism within our calculations. Recently, Liu *et al.*,[14] reported a calculated E_a value of hydride hopping between the NN sites at 27 kJ mol^{-1}. We are not sure about the reasons for the large discrepancy with our results (96 kJ mol^{-1}), but the charge state of the supercell during the transition state of the diffusion process in their study is not clear.

It is rather surprising that the activation energy for hydride diffusion in $LaSrCoO_3H_{0.70}$ obtained in this study is nearly ten times as large as that obtained by QENS, where hydride dynamics were seen above 412 °C.[11] It is worth noting again that, unlike $BaTiO_{3-x}H_x$, for the cobalt case, beyond peak 1 the HD (and H_2) gas evolution continuously increases as temperature is increased until it reaches peak 2, and that the XRD pattern of the sample quenched at 410 °C under pure Ar flow shows an impurity phase (Figure 4.10). These facts indicate a gradual net loss of hydride from $LaSrCoO_3H_{0.70}$ above the peak 1. In fact, the authors of Ref. 11 addressed an anomalous lattice expansion at 412 °C and time-dependent changes in lattice parameters (contraction of the *a* and *b* axes, and expansion of the *c* axis). The similar behaviour in lattice parameters was also observed in our experiments. This temperature- and time-dependence indicates that the observed hydrogen dynamics may be due to irreversible H_2 release (i.e. decomposition) rather than a stable solid/gas equilibrium necessary for observing bulk diffusion. We also note that the data were collected for 9–16 hours at each temperature,[11] further

increasing the potential effects of hydride loss and decomposition. The measurement time of our H/D exchange experiments is in the range of 0.5–3 hours, depending on the heating rate β, much shorter than the QENS measurement.

Another crucial factor to be addressed is the observation time scale inherent in QENS measurements. If the hopping time scale is much larger than the QENS time window (typically, 10^{-12} to 10^{-9} sec),[59, 60] hydride jumps within this long time are invisible.[61] When the temperature is higher than 412 ˚C, the hydride dynamics, regardless of whether or not it is intrinsic (i.e, dynamics in bulk $LaSrCoO_3H_{0.70}$), may be of an observable time scale, but below 400 ˚C, the slower bulk hydride diffusion may not be of the right time scale. Unlike spectroscopic techniques, however, the bulk H/D exchange experiments as we conducted here can probe hydrogen dynamics of any time scale. Therefore, it is quite possible that the previous QENS study focus on hydride mobility during decomposition, while our study is probing diffusion during reversible H/D exchange (i.e., bulk hydride diffusion in $LaSrCoO_3H_{0.70}$).

4.5. Conclusions

In conclusion, among the oxyhydrides examined in this work, H/D exchange and H_2 release reactions can be analysed sufficiently with the Kissinger method to compare activation energies for hydride transport. The dependence of activation energy on hydride content in $BaTiO_{3-x}H_x$ is most interesting, as it points to a cooperative nature of neighbouring H^- in the exchange (or moreover, diffusion) process. We propose here, on the basis of activation energy values derived from Kissinger analysis and DFT calculations, that the hydride transport in $BaTiO_{3-x}H_x$ ($0.4 < x$) and $LaSrCoO_3H_{0.70}$ rely considerably on 2NN jumps.

Explaining the differences between the gas exchange experiments and other QENS or impedance studies requires further work. Fabricating concentration gradients and observing them with SIMS (SIMS-IEDP techniques) would shed further light on these differences. However, in terms of relevance for potential hydrogenation catalysis or anion exchange for topochemical solid state chemistry, Kissinger analysis of H/D exchange reaction (or H_2 release reaction which is facile and cost-effective) is the most relevant as it directly probes the overall exchange process. Moreover, the Kissinger method may be applied to materials not compatible for NMR or impedance measurements, such as magnetic or electronically conducting samples, or samples which cannot be readily sintered into pellets. This makes it a robust method to characterize various oxyhydrides for such applications.

References

1. Kobayashi, Y.; Hernandez, O. J.; Sakaguchi, T.; Yajima, T.; Roisnel, T.; Tsujimoto, Y.; Morita, M.; Noda, Y.; Mogami, Y.; Kitada, A.; Ohkura, M.; Hosokawa, S.; Li, Z.; Hayashi, K.; Kusano, Y.; Kim, J.; Tsuji, N.; Fujiwara, A.; Matsushita, Y.; Yoshimura, K.; Takegoshi, K.; Inoue, M.; Takano, M.; Kageyama, H., *Nat. Mater.* **2012,** *11*, 507–511.

2. Sakaguchi, T.; Kobayashi, Y.; Yajima, T.; Ohkura, M.; Tassel, C.; Takeiri, F.; Mitsuoka, S.; Ohkubo, H.; Yamamoto, T.; Kim, J.; Tsuji, N.; Fujihara, A.; Matsushita, Y.; Hester, J.; Avdeev, M.; Ohoyama, K.; Kageyama, H., *Inorg. Chem.* **2012,** *51*, 11371–11376.

3. Tassel, C.; Goto, Y.; Kuno, Y.; Hester, J.; Green, M.; Kobayashi, Y.; Kageyama, H., *Angew. Chem. Int. Ed.* **2014,** *53*, 10377–10380.

4. Bang, J.; Matsuishi, S.; Hiraka, H.; Fujisaki, F.; Otomo, T.; Maki, S.; Yamaura, J.; Kumai, R.; Murakami, Y.; Hosono, H., *J. Am. Chem. Soc.* **2014,** *136*, 7221–7224.

5. Masuda, N.; Kobayashi, Y.; Hernandez, O.; Bataille, T.; Paofai, S.; Suzuki, H.; Ritter, C.; Ichijo, N.; Noda, Y.; Takegoshi, K.; Tassel, C.; Yamamoto, T.; Kageyama, H., *J. Am. Chem. Soc.* **2015,** *137*, 15315–15321.

6. Mikita, R.; Aharen, T.; Yamamoto, T.; Takeiri, F.; Ya, T.; Yoshimune, W.; Fujita, K.; Yoshida, S.; Tanaka, K.; Batuk, D.; Abakumov, A. M.; Brown, C. M.; Kobayashi, Y.; Kageyama, H., *J. Am. Chem. Soc.* **2016,** *138*, 3211–3217.

7. Yajima, T.; Takeiri, F.; Aidzu, K.; Akamatsu, H.; Fujita, K.; Yoshimune, W.; Ohkura, M.; Lei, S.; Gopalan, V.; Tanaka, K.; Brown, C. M.; Green, M. A.; Yamamoto, T.; Kobayashi, Y.; Kageyama, H., *Nat. Chem.* **2015,** *7*, 1017–1023.

8. Denis Romero, F.; Leach, A.; Möller, J. S.; Foronda, F.; Blundell, S. J.; Hayward, M. A., *Angew. Chem. Int. Ed.* **2014**, *126*, 7556–7559.

9. Tassel, C.; Goto, Y.; Watabe, D.; Tang, Y.; Lu, H.; Kuno, Y.; Takeiri, F.; Yamamoto, T.; Brown, C. M.; Hester, J., *Angew. Chem. Int. Ed.* **2016**, *128*, 9819–9822.

10. Goto, Y.; Tassel, C.; Noda, Y.; Hernandez, O.; Pickard, C. J.; Green, M. A.; Sakaebe, H.; Taguchi, N.; Uchimoto, Y.; Kobayashi, Y.; Kageyama, H., *Inorg. Chem.* **2017,** DOI: 10.1021/acs.inorgchem.6b02834.

11. Bridges, C. A.; Fernandez-Alonso, F.; Goff, J. P.; Rosseinsky, M. J., *Adv. Mater.* **2006,** *18*, 3304–3308.

12. Kobayashi, G.; Hinuma, Y.; Matsuoka, S.; Watanabe, A.; Iqbal, M.; Hirayama, M.; Yonemura, M.; Kamiyama, T.; Tanaka, I.; Kanno, R., *Science* **2016,** *351*, 1314–1317.

13. Iwazaki, Y.; Suzuki, T.; Tsuneyuki, S., *J. Appl. Phys.* **2010**, *108*, 083705.

14. Liu, X.; Bjorheim, T. S.; Haugsrud, R., *J. Mater. Chem. A* **2017**, *5*, 1050–1056.

15. Bouilly, G.; Yajima, T.; Terashima, T.; Yoshimune, W.; Nakano, K.; Tassel, C.; Kususe, Y.; Fujita, K.; Tanaka, K.; Yamamoto, T.; Kobayashi, Y.; Kageyama, H., *Chem. Mater.* **2015**, *27*, 6354–6359.

16. Yajima, T.; Kitada, A.; Kobayashi, Y.; Sakaguchi, T.; Bouilly, G.; Kasahara, S.; Terashima, T.; Takano, M.; Kageyama, H., *J. Am. Chem. Soc.* **2012**, *134*, 8782–8785.
17. Yamamoto, T.; Yoshii, R.; Bouilly, G.; Kobayashi, Y.; Fujita, K.; Kususe, Y.; Matsushita, Y.; Tanaka, K.; Kageyama, H., *Inorg. Ch*em. **2015**, *54*, 1501–1507.
18. Kissinger, H. E., *Anal. Chem.* **1957**, *29*, 1702–1706.
19. Lu, J.; Choi, Y. J.; Fang, Z. Z.; Sohn, H. Y.; Rönnebro, E., *J. Am. Chem. Soc.* **2010**, *132*, 6616–6617.
20. Liu, Y.; Zhong, K.; Luo, K.; Gao, M.; Pan, H.; Wang, Q., *J. Am. Chem. Soc.* **2009**, *131*, 1862–1870.
21. Sudik, A.; Yang, J.; Halliday, D.; Wolverton, C., *J. Phys. Chem. C* **2007**, *111*, 6568–6573.
22. Xiong, Z.; Hu, J.; Wu, G.; Chen, P.; Luo, W.; Gross, K.; Wang, J., *J. Alloy. Compd.* **2005**, *398*, 235–239.
23. Borgschulte, A.; Pendolino, F.; Gremaud, R.; Züttel, *Appl. Phys. Lett.* **2009,** *94*, 111907.
24. Hayward, M. A.; Cussen, E. J.; Claridge, J. B.; Bieringer, M.; Rosseinsky, M. J.; Kiely, C. J.; Blundell, S. J.; Marshall, I. M.; Pratt, F. L., *Science* **2002**, *295*, 1882–1884.
25. Bridges, C. A.; Darling, G. R.; Hayward, M. A.; Rosseinsky, M. J., *J. Am. Chem. Soc.* **2005**, *127*, 5996–6011.
26. Blöchl, P. E., *Phys. Rev. B* **1994**, *50*, 17953–17979.
27. Kresse, G.; Joubert, D., *Phys. Rev. B* **1999**, *59*, 1758–1775.
28. Kresse, G.; Hafner, J., *Phys. Rev. B* **1993**, *47*, 558–561.
29. Kresse, G.; Furthmüller, J., *Comput. Mater. Sci.* **1996**, *6*, 15–50.
30. Ceperley, D. M.; Alder, B. J., *Phys. Rev. Lett.* **1980**, *45*, 566–569.
31. Dudarev, S.; Botton, G.; Savrasov, S.; Humphreys, C.; Sutton, A., *Phys. Rev. B* **1998**, *57*, 1505–1509.
32. Zhang, J.; Gou, G.; Pan, B., *J. Phys. Chem. C* **2014**, *118*, 17254–17259.
33. Buckeridge, J.; Taylor, F.; Catlow, C., *Phys. Rev. B* **2016**, *93*, 155123.
34. Shirane, G.; Danner, H.; Pepinsky, R., *Phys. Rev.* **1957**, *105*, 856–860.
35. Bilc, D. I.; Orlando, R.; Shaltaf, R.; Rignanese, G. M.; Íñiguez, J.; Ghosez, P., *Phys. Rev. B* **2008**, *77*, 165107.
36. Henkelman, G.; Jónsson, H., *J. Chem. Phys.* **2000**, *113*, 9978–9985.
37. Henkelman, G.; Uberuaga, B. P.; Jónsson, H., *J. Chem. Phys.* **2000**, *113*, 9901–9904.
38. Tang, T. B.; Chaudhri, M., *J. Therm. Anal. Calorim.* **1980,** 18, (2), 247-261.
39. Ozawa, T., *J. Therm. Anal. Calorim.* **1976,** 9, (2), 217–227.
40. Gong, H., *J. Therm. Anal. Calorim.* **2005,** 79, (3), 677–683.
41. Hancke, R.; Li, Z.; Haugsrud, R., *J. Electrochem. Soc.* **2013**, *160*, 757–763.
42. Islam, M. S.; Davies, R. A.; Gale, J. D., *Chem. Mater.* **2001**, *13*, 2049–2055.
43. Ryu, K. H.; Haile, S. M., *Solid State Ionics* **1999**, *125*, 355–367.
44. Liang, K.; Du, Y.; Nowick, A., *Solid State Ionics* **1994**, *69*, 117–120.

45. Bohn, H. G.; Schober, T., *J. Am. Ceram. Soc.* **2000**, *83*, 768–772.
46. Maehlen, J. P.; Yartys, V. A.; Denys, R. V.; Fichtner, M.; Frommen, C.; Bulychev, B. M.; Pattison, P.; Emerich, H.; Filinchuk, Y. E.; Chernyshov, D., *J. Alloy. Comp.* **2007**, *280*, 446–447.
47. Ferrizz, R. M. *Sandia report* **2006**, *sand2006–7014*.
48. Acke, F.; Panas, I., *J. Phys. Chem. B* **1998**, *102*, 5158–5164.
49. Preis, W.; Sitte, W., *Solid State Ionics* **2006**, *177*, 3093–3098.
50. Nowotny, J.; Rekas, M., *Ceram. Int.* **1994**, *20*, 265–275.
51. Preis, W., *Solid State Ionics* **2017**, *299*, 82–88.
52. Wemicke, R., *Philips Res. Rept.* **1976**, *31*, 526–543.
53. Maier, J.; Schwitzgebel, G.; Hagemann, H. J. *J. Solid State Chem.* **1985**, *58*, 1–13.
54. Kolodiazhnyi, T.; Petric, A., *J. Am. Ceram. Soc.* **2003**, *86*, 1554–1559.
55. Kharton, V.; Yaremchenko, A.; Viskup, A.; Mather, G.; Naumovich, E.; Marques, F., *J. Electroceram.* **2001,** 7, (1), 57-66.
56. Didier, C.; Claridge, J.; Rosseinsky, M., *J. Solid State Chem.* **2014,** *218*, 38-43.
57. Dobson, D. P.; Dohmen, R.; Wiedenbeck, M., *Earth Planet. Sci. Lett.* **2008,** *270*, (1), 125-129.
58. Markov, A. A.; Patrakeev, M. V.; Kharton, V. V.; Pivak, Y. V.; Leonidov, I. A.; Kozhevnikov, V. L., *Chem. Mater.* **2007**, *19*, 3980–3987.
59. Mehrer, H., Diffusion in Solids: Fundamentals, Methods, Materials, Diffusion-Controlled Process. *Springer Series in Solid State Science 155* **2007**.
60. al-Wahish, A.; Jalarvo, N.; Bi, Z.; Herwig, K. W.; Bridges, C.; Paranthaman, M. P.; Mandrus, D., *J. Phys. Chem. C* **2014**, *118*, 20112–20121.
61. Österberg, C.; Fahlquist, H.; Häussermann, U.; Brown, C. M.; Udovic, T. J.; Karlsson, M., *J. Phys. Chem. C* **2016**, *120*, 6369–6376.

Table 4.1. Lattice parameters of $LaSrCoO_3H_{0.70}$ after D_2/Ar or Ar treatment.

Samples	*a*	*b*	*c*	Space group
$LaSrCoO_4$	3.80689(8)	_	12.5042(3)	Tetragonal, *I4/mmm*
$LaSrCoO_3H_{0.70}$	3.88151(8)	3.60506(7)	12.9863(3)	Orthorhombic, *Immm*
$LaSrCoO_3H_{0.70}$ after 410 °C D_2	3.87212(2)	3.6105(2)	13.0120(6)	Orthorhombic, *Immm*
$LaSrCoO_3H_{0.70}$ after 410 °CAr	3.8718(2)	3.6103(2)	13.0226(7)	Orthorhombic, *Immm*
$LaSrCoO_3H_{0.70}$ after 450 °C D_2	3.8762(2)	3.6143(1)	13.0216(5)	Orthorhombic, *Immm*
$LaSrCoO_3H_{0.70}$ after 500 °C D_2	3.8629(4)	3.6100(4)	13.046(1)	Orthorhombic, *Immm*
$LaSrCoO_3H_{0.70}$ after 550 °C D_2	3.8204(7)	3.5897(6)	13.176(3)	Orthorhombic, *Immm*
$LaSrCoO_3H_{0.70}$ after 700 °C D_2	3.7440(2)	_	13.3248(8)	Tetragonal, *I4/mmm*
$LaSrCoO_3H_{0.70}$ after 700 °CAr	3.7497(2)	_	13.2820(7)	Tetragonal, *I4/mmm*

Table 4.2. Details of the oxyhydride compositions.

Samples $BaTiO_{3-x}H_x$	Synchrotron XRD data		Lab X-Ray data		*x*, TG data	Particle size nm
	Lattice parameters	*x*, Rietveld refinement	Lattice parameters	*x*, Rietveld refinement		
$BaTiO_{3-x}H_x$-4 days	_	_	4.02578(4)	0.36(1)	0.35	100
$BaTiO_{3-x}H_x$-5 days	4.02866(3)	0.39(1)	4.02832(6)	0.39(1)	0.39	100
$BaTiO_{3-x}H_x$-6 days	4.030265(8)	0.45(1)	4.03045(4)	0.45(2)	0.44	100
$BaTiO_{3-x}H_x$-7 days	4.03208(1)	0.56(1)	4.03300(3)	0.56(1)	0.60	100
$BaTiO_{3-x}D_x$	4.0297(1)	0.47	4.0291(1)	0.49(2)	_	100

Table 4.3. The hydride exchange amounts from various oxyhydrides ($BaTiO_{3-x}H_x$) at different heating rates. The amounts were obtained by integrating the MS curves. The sample weights are approx. 17 mg.

Hydride content, *x*	Scaling factor (a.u.)	1 ˚C/min	5 ˚C/min	10 ˚C/min	20 ˚C/min	30 ˚C/min
0.35	10^{-10}	1.61	0.80	0.70	0.60	0.70
0.39	10^{-8}		0.66	0.71	0.69	0.40
0.44	10^{-7}		1.03	0.80	0.82	0.62
0.60	10^{-7}	0.50	0.69	0.82	0.73	1.27

Table 4.4. Activation energies E_a of H/D exchange and H_2 release from $BaTiO_{3-x}H_x$ (x = 0.35, 0.39, 0.44, and 0.60), $BaTiO_{2.53}D_{0.47}$, and $LaSrCoO_3H_{0.70}$.

Samples	Activation energy (kJ mol^{-1})	
	H/D exchange	H_2 release
$BaTiO_{2.65}H_{0.35}$	370	371
$BaTiO_{2.61}H_{0.39}$	253	311
$BaTiO_{2.56}H_{0.44}$	238	234
$BaTiO_{2.40}H_{0.60}$	226	221
$BaTiO_{2.53}D_{0.47}$	200	–
$LaSrCoO_3H_{0.70}$	193	170

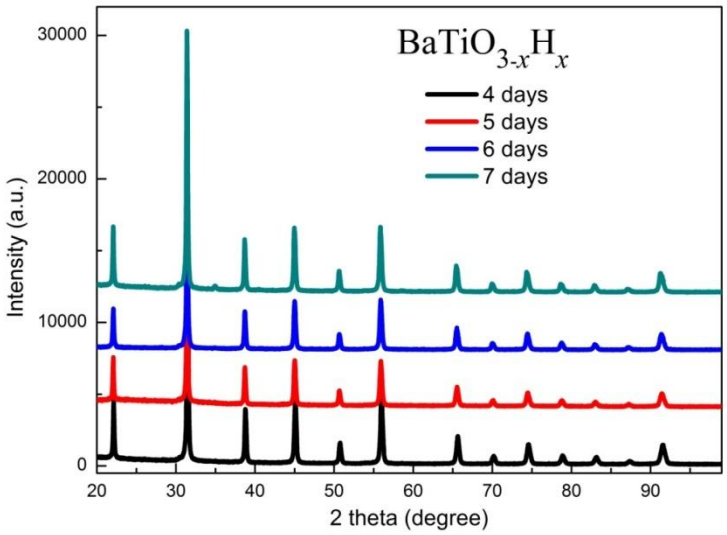

Figure 4.1. XRD patterns of $BaTiO_{3-x}H_x$ with different reaction time of 4, 5, 6, and 7 days at 560 ˚C. The lattice parameters were summarized in Table 4.2.

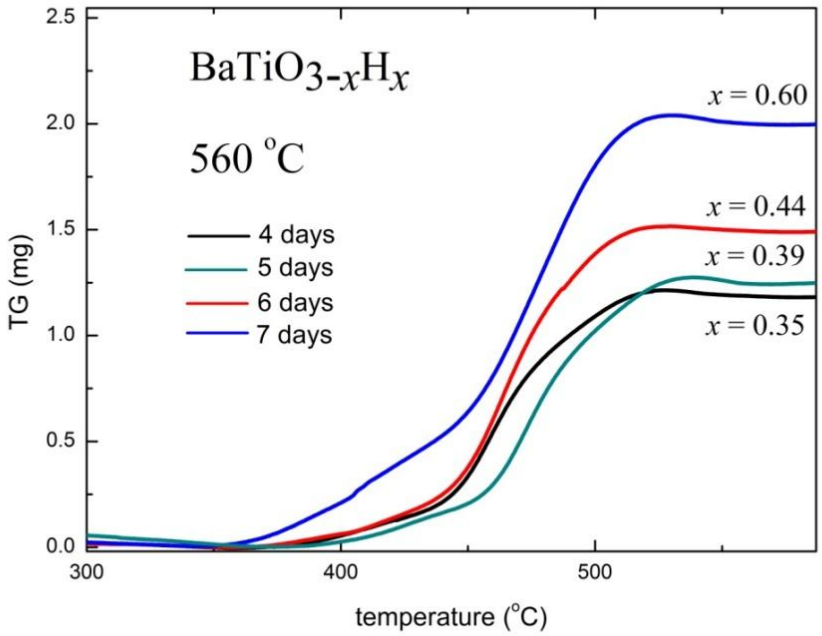

Figure 4.2. Thermalgravimetric analysis of powder $BaTiO_{3-x}H_x$ samples under flowing oxygen. Prior to each TG experiment, the powder oxyhydride samples were heated at 120 ˚C for 2 hours to remove adsorbed water, which is the same with H/D exchange and H_2 release experiments. The weight increase is 1.12 mg for 46.8 mg 4 days sample, 1.24 mg for 46.6 mg 5 days sample, 1.49 mg for 50.0 mg 6 days sample, and 2.01 mg for 49.8 mg 7 days sample. Such weight increase is consistent with formula of $BaTiO_{2.65}H_{0.35}$, $BaTiO_{2.61}H_{0.39}$, $BaTiO_{2.56}H_{0.44}$, and $BaTiO_{2.40}H_{0.60}$ for 4, 5, 6, and 7 days powder samples, respectively.

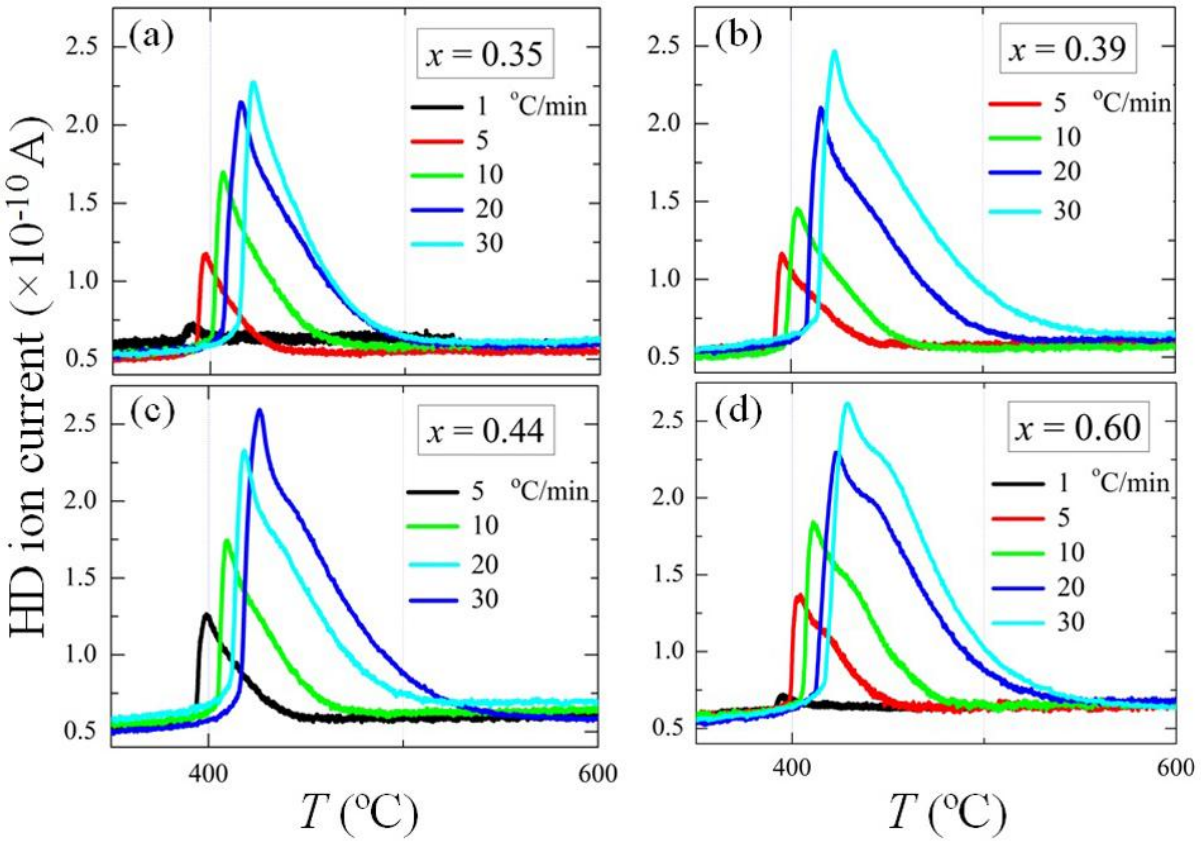

Figure 4.3. HD evolution as a function of heating rate β for $BaTiO_{3-x}H_x$ with (a) x = 0.35, (b) x = 0.39, (c) x = 0.44, and (d) x = 0.60.

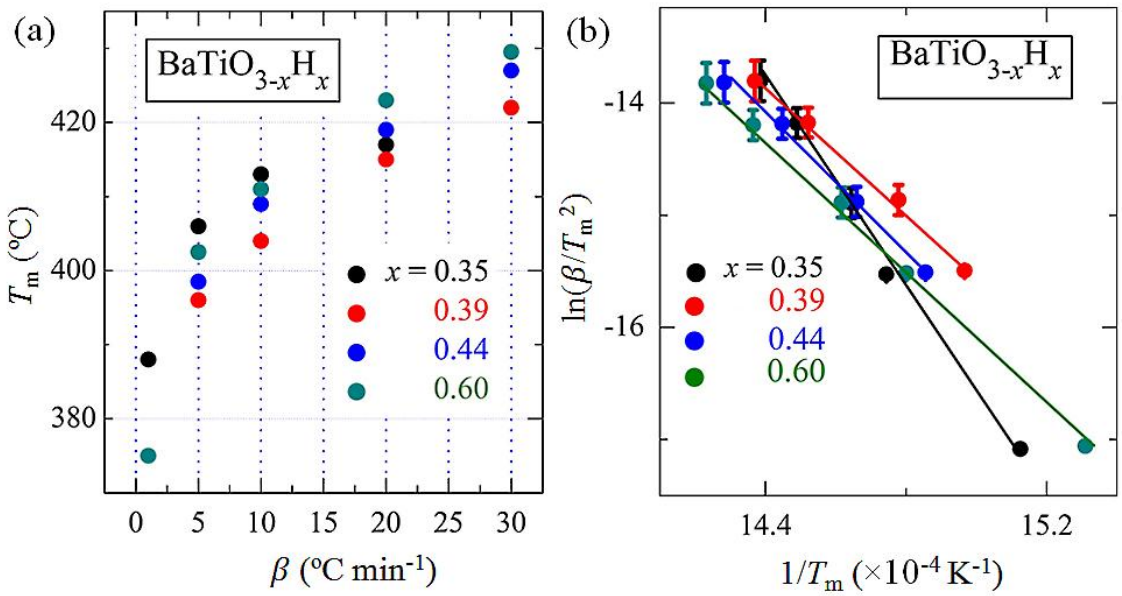

Figure 4.4. (a) HD evolution temperatures T_m for $BaTiO_{3-x}H_x$ as a function of β. (b) Kissinger plots ($\ln(\beta/T_m^2)$ *vs.* $1/T_m$) to evaluate E_a of H/D exchange process.

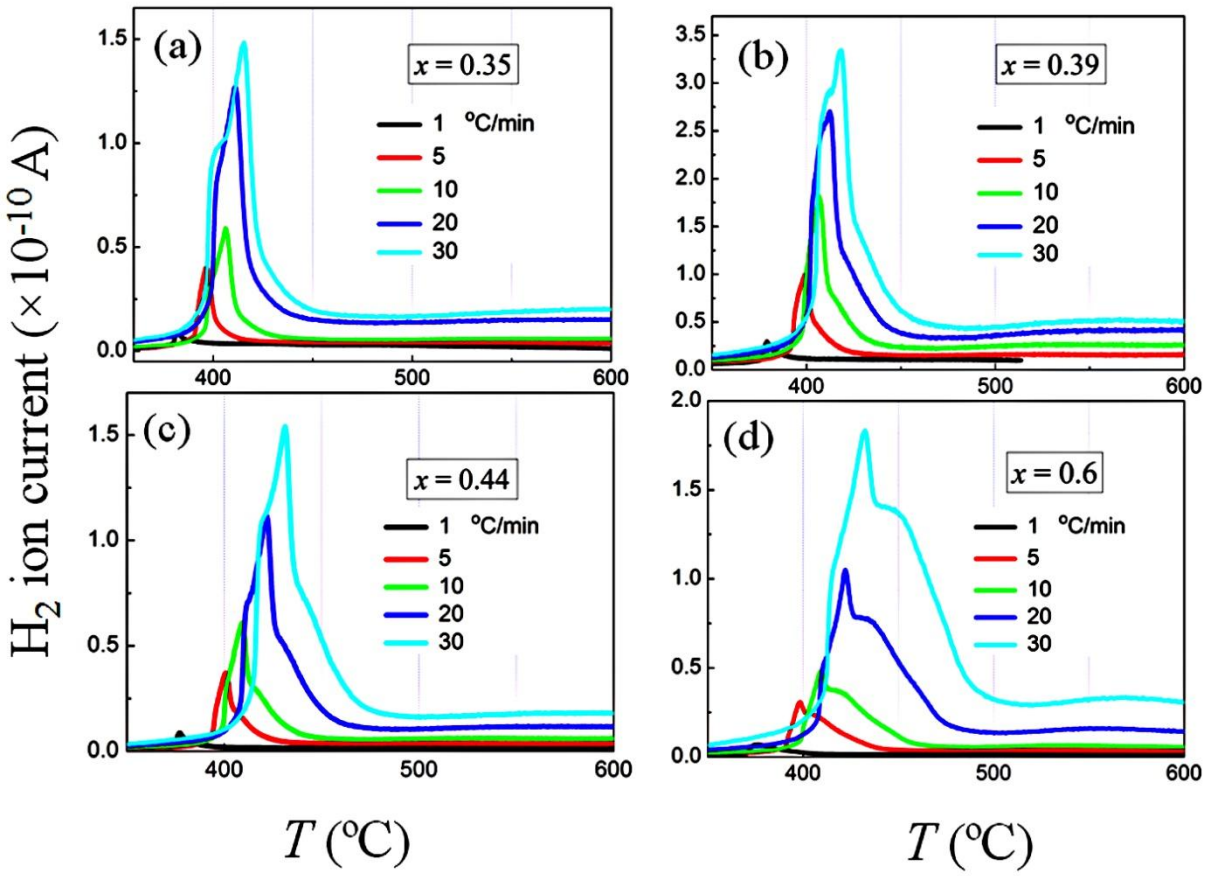

Figure 4.5. H_2 release from $BaTiO_{3-x}H_x$ with (a) x = 0.35, (b) x = 0.39, (c) x = 0.44, and (d) x = 0.6 under different heating rates of β = 1, 5, 10, 20 and 30 ˚C min^{-1}.

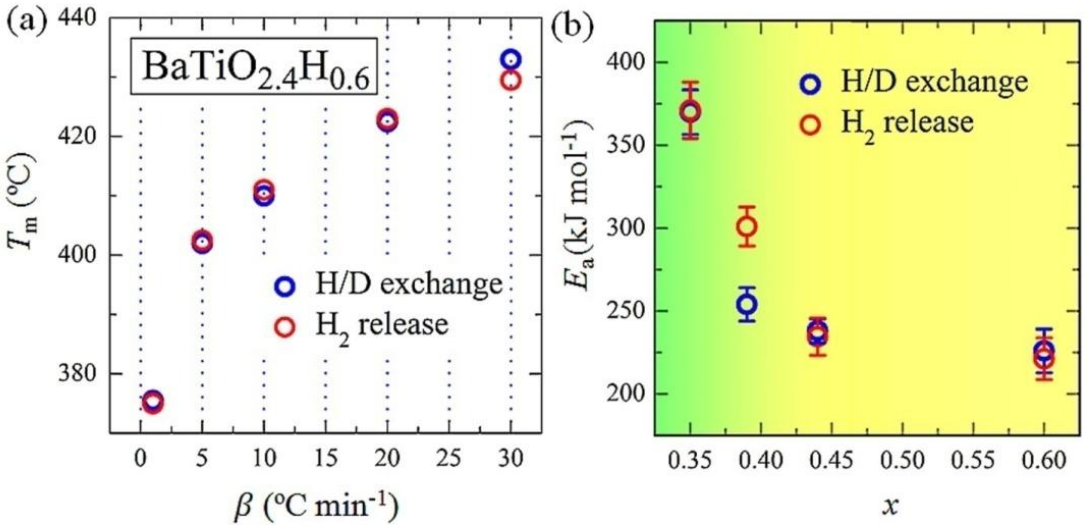

Figure 4.6. (a) The peak temperature T_m for H/D exchange (blue) and H_2 release (red) as a function of β in $BaTiO_{2.40}H_{0.60}$. (b) The activation energy E_a for H/D exchange (blue) and H_2 release (red) in $BaTiO_{3-x}H_x$ as a function of hydride content x.

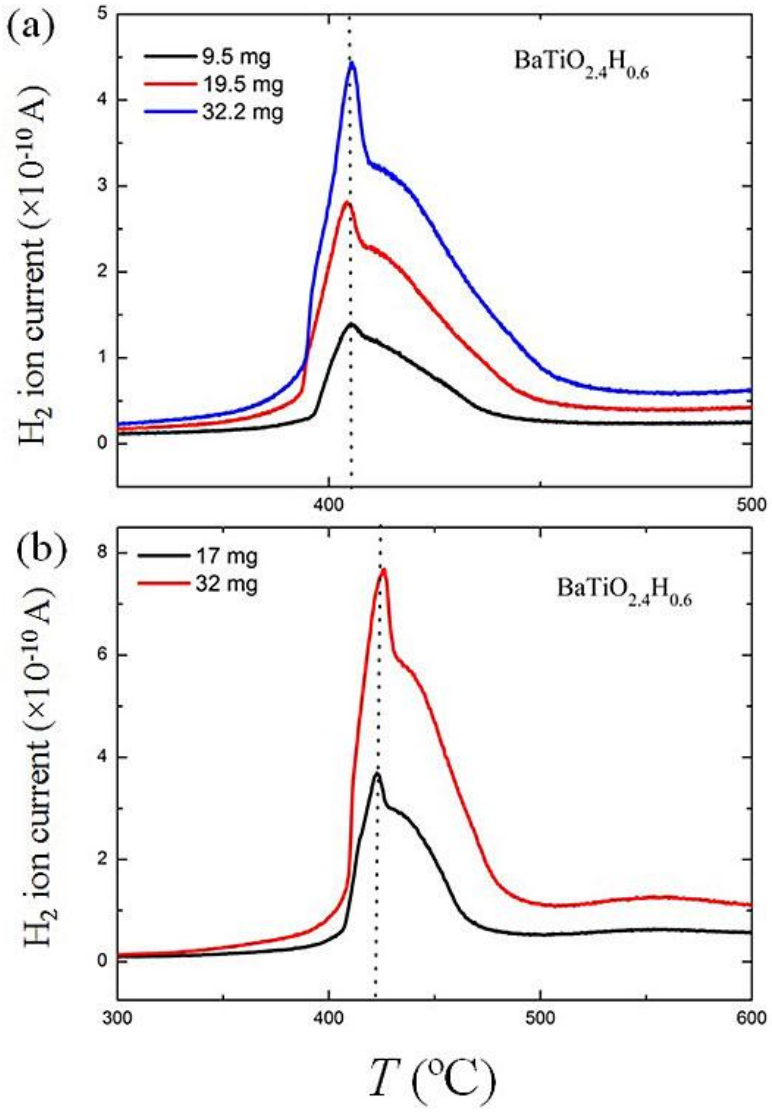

Figure 4.7. Peak temperature T_m as function of sample weights, (a) at β = 10 ˚C min^{-1}; (b) at β = 30 ˚C min^{-1}.

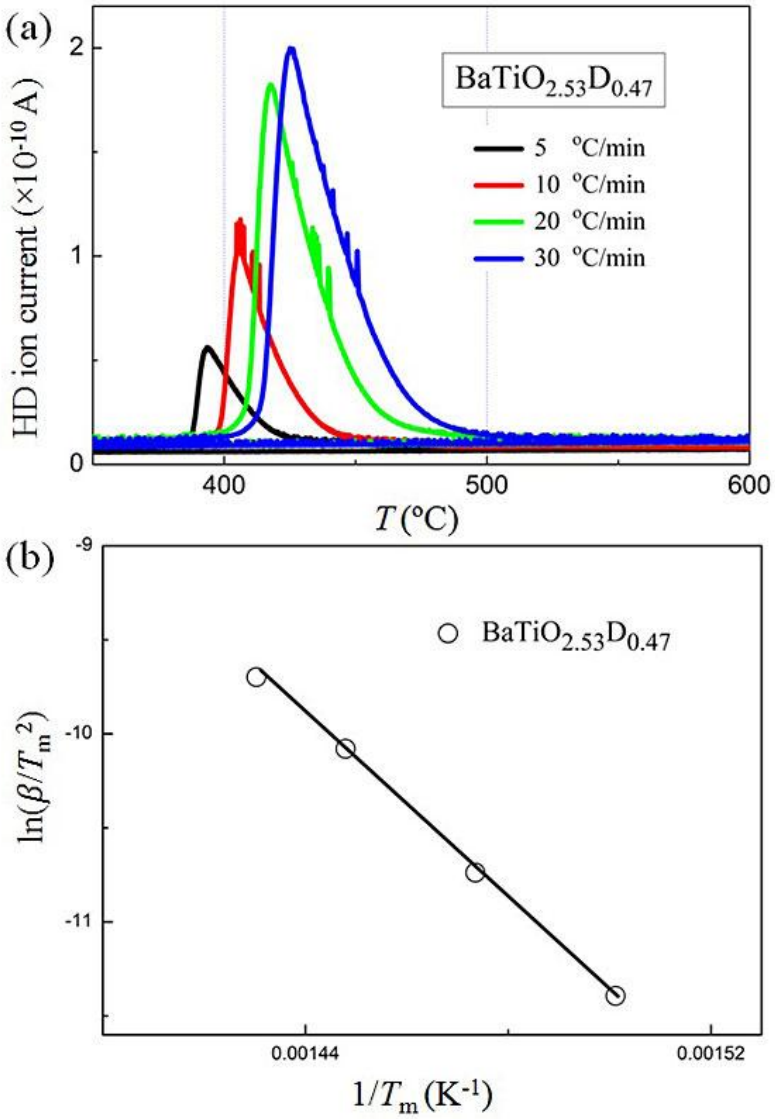

Figure 4.8. (a) HD evolution as a function of β for $BaTiO_{2.53}D_{0.47}$. (b) Kissinger plot ($\ln(\beta/T_m^2)$ *vs.* $1/T_m$) to evaluate E_a of H/D exchange process in $BaTiO_{2.53}D_{0.47}$.

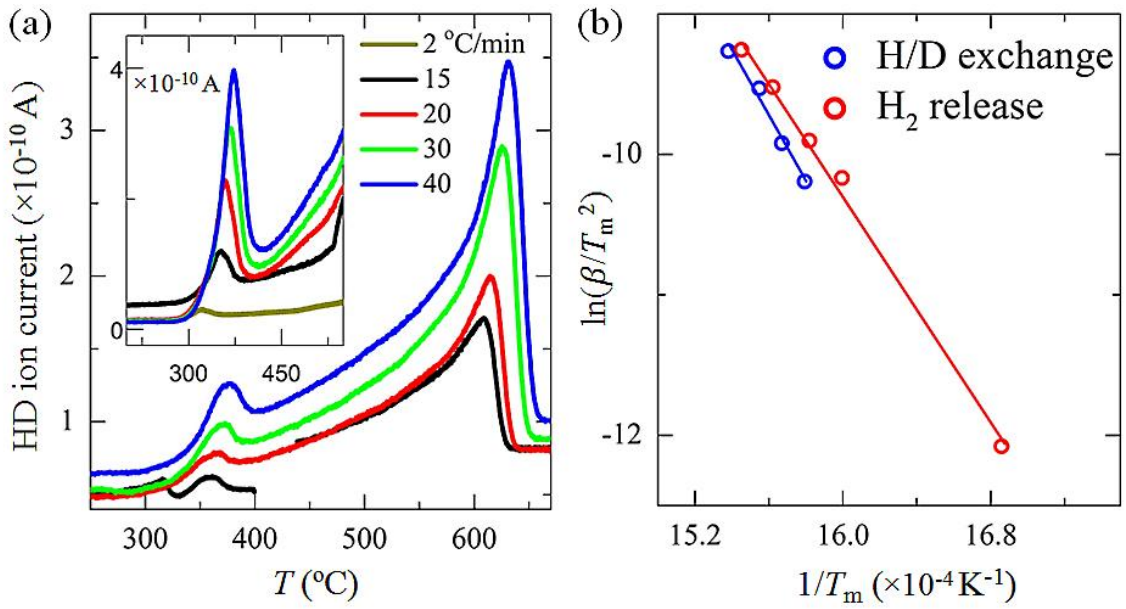

Figure 4.9. (a) HD evolution as a function of β for $LaSrCoO_3H_{0.70}$ showing two peaks. The lower temperature peak corresponds to the H/D exchange (T_m). The H_2 release result is shown in the inset. (b) Kissinger plots ($\ln(\beta/T_m^2)$ *vs.* $1/T_m$) to evaluate E_a for H/D exchange (blue) and H_2 release (red) processes in $LaSrCoO_3H_{0.70}$.

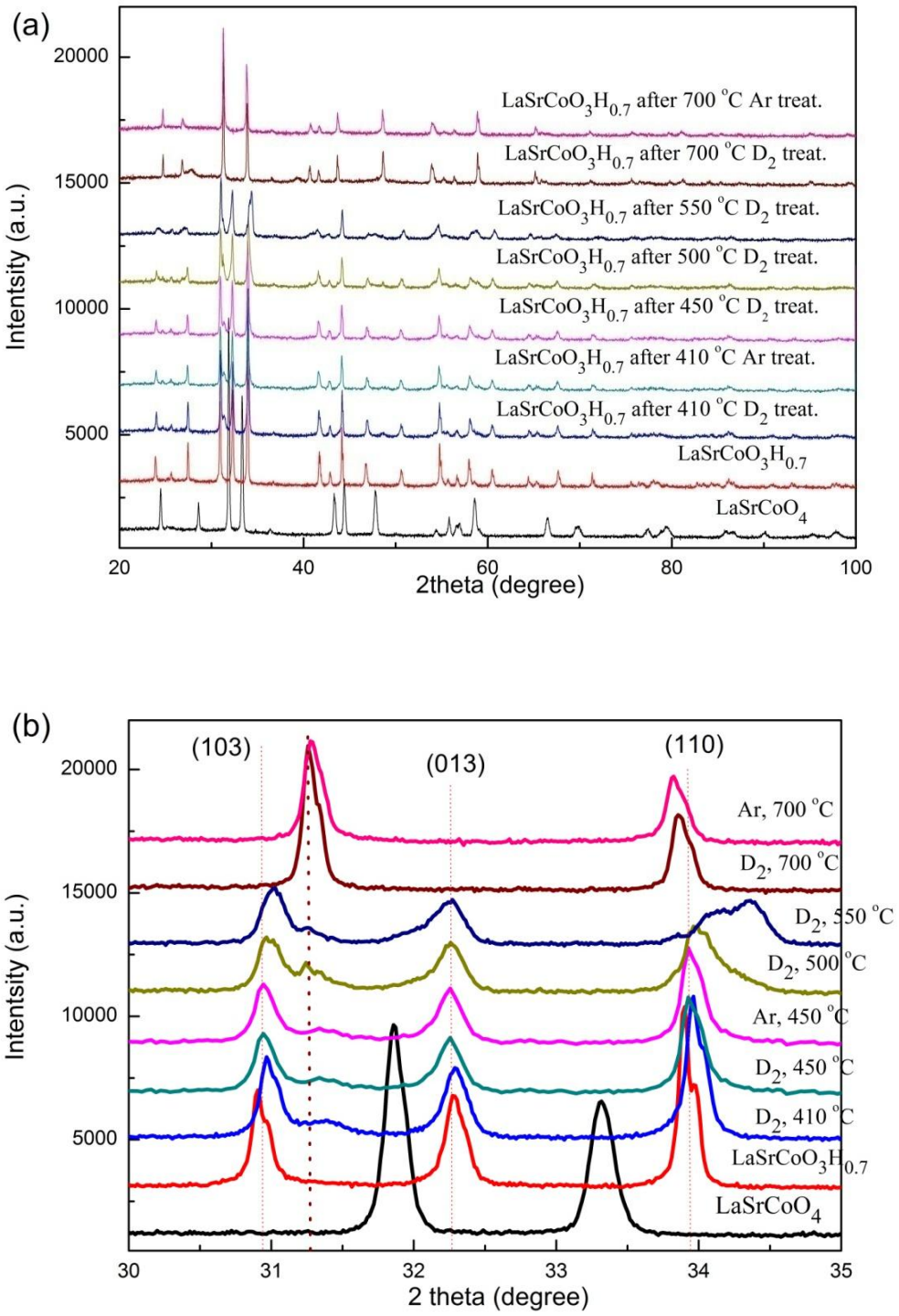

Figure 4.10. (a) XRD patterns of $LaSrCoO_3H_{0.70}$ at various states. The lattice parameters were summarized in Table 4.1. (b) is the enlarged figure of (a) from $2\theta = 30–35^{o}$.

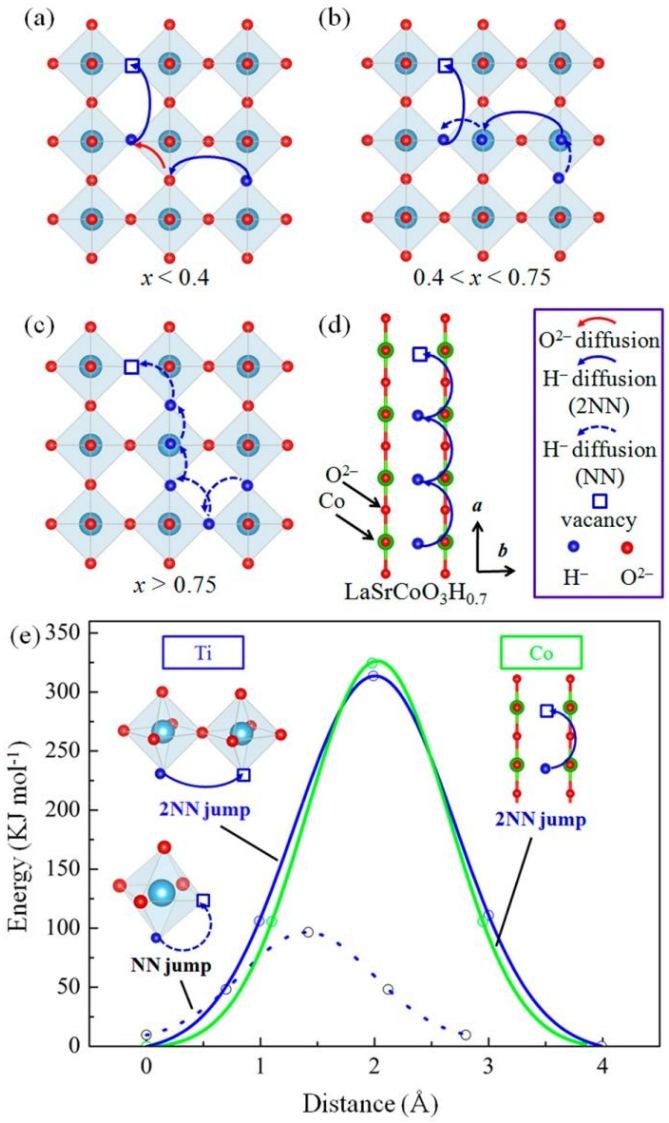

Figure 4.11. The possible hydride diffusion pathway in $BaTiO_{3-x}H_x$ with hydride contents are $x < 0.4$ (a), $0.4 < x < 0.75$ (b), $0.75 < x$ (c). (d) 2NN hydride hopping in $LaSrCoO_3H_{0.70}$. (e) The calculated energy profiles for hydride migration along NN (blue, dot line), 2NN (blue, solid line) jumps in $BaTiO_{3-x}H_x$, and 2NN (green) jumps in $LaSrCoO_3H_{0.70}$.

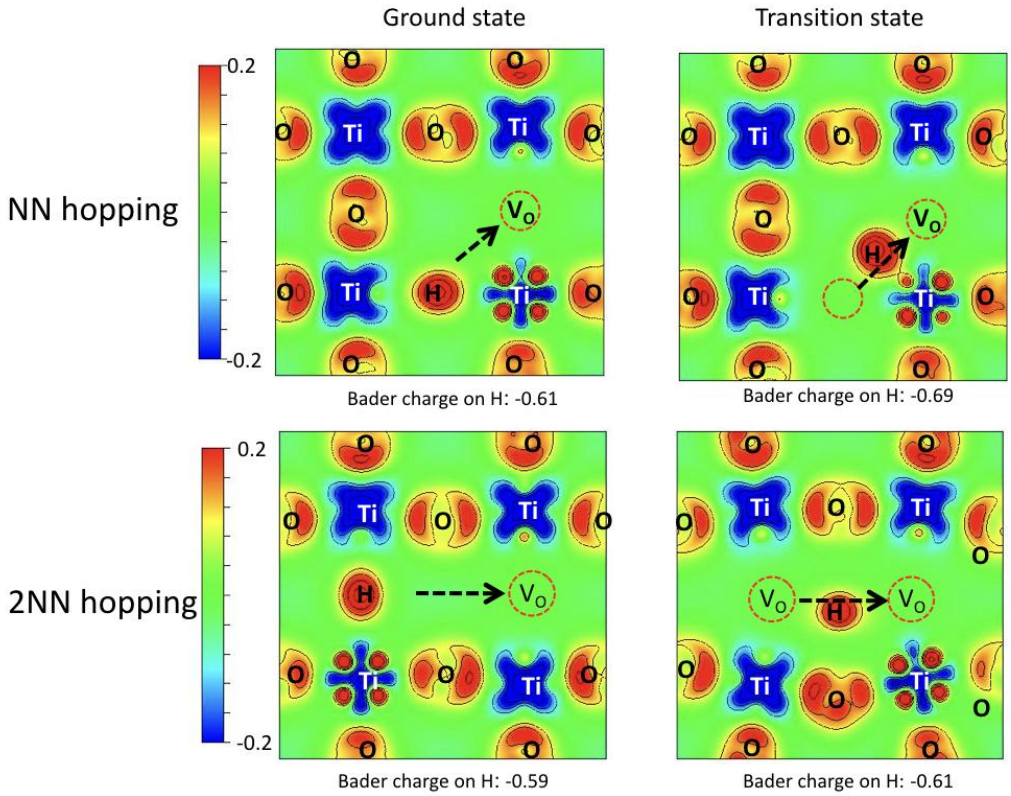

Figure 4.12. Differential charge density maps of a $BaTiO_{3-x}H_x$ system during NN and 2NN hopping. Red indicates anionic character, while blue indicates cationic character (scale bar units in $Å^{-3}$). Bader charge states of H are also indicated.

General Conclusion

This thesis reported the catalytic reactions on the metal-free $BaTiO_{2.5}H_{0.5}$ (and TiH_2), and $BaTiO_{2.5}H_{0.5}$-supported Ru, Fe, Co, Ni metal catalysts, especially focused on NH_3 synthesis and CO_2 methanation. In addition, by using H/D exchange, we investigated the hydride diffusion in the perovskite oxyhydrides. Combined isotopic exchange and Kissinger analysis, this enables us to argue probable hydride hopping process of the whole system, providing a general guide to design and improve H^- conductivity in oxyhydrides. Morover, on the basis of catalytic results, two main features of oxyhydride in the applications of catalysis were observed: (i) the catalytic activity have a hydride content-dependent effect; i.e. more hydride amounts, more high activity. (ii) hydride anion in the oxyhydride lattice is quite mobile, which provides a hydrogen spillover pathway during the reaction. Hence, the works in this thesis point the way to the future use of oxyhydride for catalysis applications; that is, the oxyhydride with high concentration of hydride have a large potential in catalysis applications. This potential could be further verified by H/D exchange experiments, where the activation energy of hydride diffusion can be calculated by Kissinger model.

In *Chapter 1*, the author demonstrated that the solid-state hydride-containing Ti compounds (TiH_2 and $BaTiO_{2.5}H_{0.5}$) exhibit continuously NH_3 synthesis activity under a Haber-Bosch condition (400 ˚C, 5 MPa), with activity almost comparable to conventional supported Ru catalysts such as Cs-Ru/MgO or $Ru/BaTiO_3$. Titanium, being an early transition metal, was traditionally viewed as an inactive metal for catalytic NH_3 synthesis, but a continuous NH_3 formation on $BaTiO_{2.5}H_{0.5}$ and TiH_2 were observed even in the absence of the typically necessary Ru, Fe, or Co particles. From the perspective of NH_3 synthesis, finding new catalysts to break the scale limitation have garnered much attention recently. While the activity is modest, when compared to industrial catalysts (KM1 or Ba-Ru/C), the Ti-H solid system is one example of a new composition that may be a starting point for breaking scaling rules, and ultimately lead to cheaper catalysts working at lower temperatures and pressures.

In *Chapter 2*, the author demonstrated that the introduction of hydride into the oxide $ATiO_3$ (A = Ca, Sr, Ba) support results in enhanced activities and altered kinetic parameters, with the details depending on the choice of supported metals (Ru, Fe, Co). Overall, the high activity is due to a hydrogen-based Mars–van Krevelen mechanism decreasing the hydrogen poisoning, and also as hydride functioning either as a strong electron donor. Which of these effects visibly dominates depends on the metal supported. Comparison with other hydride-based catalysts reveals that hydride can have a variety of roles, depending on the support matrix. In terms of optimization, the titanium

oxyhydrides are based on well-known oxide perovskites, and have a potential to have their composition tuned in *A*-site or *B*-site substitution to search a further active ammonia synthesis catalyst. As the number of oxyhydrides increases, this study shows that the interesting effects of hydrogen can be investigated in a wider range of materials than previously thought.

In *Chapter 3*, the perovskite oxyhydride $BaTiO_{2.4}H_{0.6}$ was discovered to be an effective water-stable support material for CO_2 methanation. Kinetic analysis of the Ru-based catalysts shows how both oxyhydride and oxide supports have similar activation energies and CO_2 reaction orders but quite different H_2 reaction orders. Explaining the origins of these reaction orders requires more study. From a more general point of view, this study is the first demonstration of a hydride-based catalyst in a hostile environment. The hydride here seems to be adequately stabilized in the perovskite oxide lattice; perovskites are a large material family with many minor structural and compositional modifications possible. With these potential applications in catalysis, it is evident that the transition metal oxyhydrides will continue to gain prominence in the future catalysis research.

In *Chapter 4*, the author demonstrated that the H/D exchange and H_2 release reactions can be analysed sufficiently with the Kissinger method to compare activation energies for hydride transport in perovskite oxyhydrides. The dependence of activation energy on hydride content in $BaTiO_{3-x}H_x$ is most interesting, as it points to a cooperative nature of neighbouring H^- in the exchange (or diffusion) process. On the basis of activation energy values derived from Kissinger analysis and DFT calculations, the hydride transport in $BaTiO_{3-x}H_x$ ($0.4 < x$) and $LaSrCoO_3H_{0.70}$ rely considerably on 2NN jumps. In terms of relevance for potential hydrogenation catalysis or anion exchange for topochemical solid state chemistry, Kissinger analysis of H/D exchange reaction is the most relevant as it directly probes the overall exchange process.

List of Publications

Chapter 1

Titanium-based hydrides as heterogeneous catalysts for ammonia synthesis

Yoji Kobayashi, Ya Tang, Toki Kageyama, Hiroki Yamashita, Naoya Masuda, Saburo Hosokawa, Hiroshi Kageyama.

Journal of the American Chemical Society 139 (2017), 18240–18246

Chapter 2

Metal-dependent support effects of oxyhydride-supported Ru, Fe, Co catalysts for ammonia synthesis

Ya Tang, Yoji Kobayashi, Naoya Masuda, Yoshinori Uchida, Hiroki Okamoto, Toki Kageyama, Saburo Hosokawa, François Loyer, Kei Mitsuhara, Keisuke Yamanaka, Yusuke Tamenori, Cédric Tassel, Takafumi Yamamoto, Tsunehiro Tanaka, Hiroshi Kageyama.

Chemical Science, submitted.

Chapter 3

Hydride–enhanced CO_2 methanation: water-stable $BaTiO_{2.4}H_{0.6}$ as a new support

Ya Tang, Yoji Kobayashi, Cédric Tassel, Takafumi Yamamoto, Hiroshi Kageyama.

Advanced Energy Materials, submitted.

Chapter 4

On hydride diffusion in transition metal perovskite oxyhydrides investigated via deuterium exchange

Ya Tang, Yoji Kobayashi, Kazuki Shitara, Ayako Konishi, Akihide Kuwabara, Takahide Nakashima, Cédric Tassel, Takafumi Yamamoto, Hiroshi Kageyama.

Chemistry of Materials, **2017**, *29* (19), 8187–8194

The following papers are not included in this thesis

High-Pressure Synthesis of Manganese Oxyhydride with Partial Anion Order

Cédric Tassel, Yoshinori Goto, Daichi Watabe, Ya Tang, Honcheng Lu, Yoshinori Kuno, Fumitaka Takeiri, Takafumi Yamamoto, Craig M Brown, James Hester, Yoji Kobayashi, Hiroshi Kageyama.

Angewandte Chemie International edition 128 (2016), 9819–9822

Topochemical Nitridation with Anion Vacancy-Assisted N^{3-}/O^{2-} Exchange

Riho Mikita, Tomoko Aharen, Takafumi Yamamoto, Fumitaka Takeiri, Ya Tang, Wataru Yoshimune, Koji Fujita, Suguru Yoshida, Katsuhisa Tanaka, Dmitry Batuk, Artem M Abakumov, Craig M Brown, Yoji Kobayashi, Hiroshi Kageyama.

Journal of the American Chemical Society 138 (2016), 3211–3217

Acknowledgment

This thesis summarizes the author's studies at Kageyama Laboratory during Apr. 2014 – Apr. 2018, Department of Energy and Hydrocarbon Chemistry, Graduate School of Engineering, Kyoto University.

The author is greatly appreciates for Professor Hiroshi Kageyama to give me the opportunity to study in his lab, especially for his continuous encouragement, constructive criticism and fruitful suggestion. The author also wishes to express his gratitude to Lecturer Yoji Kobayashi, his support was invaluable. The author is also grateful to Associate Professor Cédric Tassel, Takafumi Yamamoto, and Hiroshi Takatsu, for their kind guidance and constructive suggestion.

The author would like to express his gratitude to the following people: Dr. Fumitaka Takeiri, Yuki Matsumoto, Taito Murakami, Hiroki Okamoto, Naoya Masuda, Ryo Horikoshi, Toki Kageyama, Hiroyuki Okajima, Daichi Kato, Kazunari Arai, Takahide Nakashima, for their friendship, experiments and continuous encouragement. The author is also grateful to Professor Akihide Kuwabara (JFCC), for his fruitful discussion on diffusion DFT calculations. The author has worked with many wonderful students/researchers during my doctor course, who have contributed in various ways to making my work possible. The author would like to thank the past, present post-doctoral fellows, secretaries and visitors of the Kageyama Laboratory for their hearty encouragement and friendship during his time in the laboratory. The author wishes to thank all my Chinese friends in Katsura campus of Kyoto University for their kindly encouragement and warm support.

The author would like to thank for the financial support of Japanese Government (Monbukagakusho, MEXT) Scholarship. Finally, I would like to offer special thanks to my mother, Daorong Lin and my girlfriend, Wenqian Chen.

Ya Tang

2018